Calculation of Virial Coefficients and Their Uses

A Dissertation Presented

by

Nicholas Jerome Getter

to

The Graduate School

in Partial Fulfillment of the

Requirements

for the Degree of

Doctor of Philosophy

in

Chemistry

Stony Brook University

December 2010

Stony Brook University

The Graduate School

Nicholas Jerome Getter

We, the dissertation committee for the above candidate for

the Doctor of Philosophy degree, hereby recommend

acceptance of this dissertation.

George Stell – Dissertation Advisor
Distinguished Professor Emeritus, Department of Chemistry

Ben Chu – Chairperson of Defense
Distinguished Professor, Department of Chemistry

Roy Lacey
Professor, Department of Chemistry

Barry McCoy
Distinguished Professor, Department of Physics

This dissertation is accepted by the Graduate School

Lawrence Martin
Dean of the Graduate
School

Abstract of Dissertation

Calculation of Virial Coefficients and Their Uses

by

Nicholas Jerome Getter

Doctor of Philosophy

In

Chemistry

Stony Brook University

2010

This work is centers on the classical statistical derivation of thermodynamic properties of a system from its pair potential through the calculation of virial coefficients and also develops a useful method for modeling systems with the square-well potential. It is organized into 5 chapters.

Chapter 1 lays the statistical mechanics background for the use of virial coefficients and the square-well model. It is intended for the reader unfamiliar with these concepts and with the exception of a derivation of C(T) for the square-well potential using overlapping spheres, does not contain any novel discoveries.

Chapter 2 introduces a Monte Carlo hit-and-miss technique for calculating virial coefficients for the square-well named ratio integration. Unlike traditional Monte Carlo hit-and-miss integration, only the percentage of hits are measured

and not the volume of the integration. The integration is then scaled by the literature values for virial coefficients of the hard sphere model. This has a significant increase in computation speed.

In chapter 3 the virial coefficients calculated in chapter 2 are used to produce phase diagrams using the Maxwell construction. A technique is developed to fit the square-well parameters to second virial coefficient data. The method is examined for argon and then generalized for mixtures.

Mayer sampling is a technique for calculating virial coefficients at specific temperatures for any pair potential. In chapter 4 it is used to examine two models for the C_{60} fullerene, the widespread Girifalco potential and its suggested replacement, the Smith-Thakkar potential. These are both also modeled by the square-well potential using the techniques developed in chapters 2 and 3.

Chapter 5 presents possible future extensions and improvements of this work.

Dedication Page

To my daughter and wife, my inspiration and strength, my heart and soul.

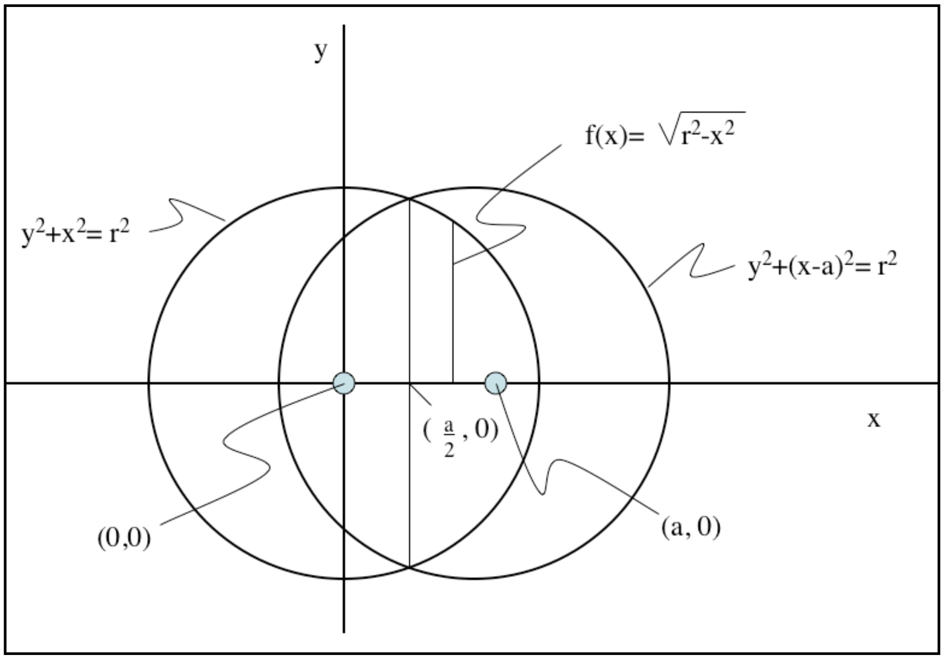

"*If you dream it, you can do it*"

-Saving Silverman

Table of Contents

List of Figure

List of Tables

Acknowledgements

Thanks to everyone who made this possible. To my family, their support and confidence in me was unbreakable. To the Stony Brook Chemistry Department, whose staff and faculty selflessly worked hard to ensure the success of their students. And to my Committee, who patiently adjusted their schedules to meet for my defense.

A special thanks to my advisor, Dr. Stell, without whom none of this would be possible. Thank you for your constant support.

And finally thank you to my wife. She has stood by me and sacrificed much for this work, it is as much hers as mine.

Chapter 1
Statistical-Mechanical Basis

1.1 INTRODUCTION

The study of thermodynamics has a deep and long history. Scientists in the 17th century began to explore the relationships energy and heat had with pressure, temperature, and volume. During the 18th century the concept of entropy was developed. Even before the concept of the atom was accepted or well understood scientists had a rich understanding of the macroscopic effects work and heat had on a system. Amazingly, early thermodynamic scientists only developed these relationships through experimental observations, even though they could never explain the phenomena they observed.

Naturally, with the development of an atomic theory came the desire to describe observable, macroscopic properties through the behavior of atoms. A statistical treatment of these behaviors in order to explain the thermodynamic phenomena is the goal of statistical thermodynamics.

Boltzmann is often credited as the father of statistical mechanics because of his work in the late 19th century. The Boltzmann distribution law describes the probability of a state occurring as a function of the energy of that state. This allowed Gibbs to develop the statistical ensemble.

Because of the relatively recent development of statistical mechanics, major advances continued well into the 20th century in a way that could not have been possible in areas of thermodynamics and classical macroscopic mechanics.

1.2 ENSEMBLES

The Boltzmann distribution law describes the probability of finding a system in a state as proportional to a function of absolute temperature (T) and the energy of the state (ε):

$$e^{-\varepsilon/kT} \tag{1.2.1}$$

where k is the Boltzmann constant.

The normalized probability of finding the system in some state is given by the value of expression (1.2.1) for that state divided by the sum of the values of expression (1.2.1) for all possible states the system can be in. With the probabilities of each state known, the thermodynamics are calculable, as we discuss in subsequent sections.

The challenge then is to find the sum of (1.2.1) for all states. This is the concept behind the statistical ensemble. The ensemble can be visualized as an average over either an infinite number of systems or one system over an infinite length of time.

One can imagine a system with a definite volume, and then imagines that the system is in contact with a thermal reservoir capable of exchanging heat to ensure a constant temperature. The system is also connected to a reservoir containing particles at the same chemical potential as those in the system, which can be exchanged freely with the system. Now one mentally allows the system to grow to infinite volume. Then the system is partitioned into individual microsystems, all with the same volume. Each microsystem has the same volume and temperature, and is composed of particles with the same chemical potential. Each microsystem also has some pressure and number density that describe the microstate of the microsystem.

This imaginary system is a grand canonical ensemble. The probability of finding another system with the same volume, temperature and chemical potential as our microsystems in one of the microstates is equal to the number of microsystems with that microstate divided by the total number of microsystems.

An equally valid method for calculating the probability of finding a system in a state is to again imagine a system of definite volume free to exchange particles and heat with the surroundings in order to ensure a constant temperature and chemical potential. If the system is allowed to exist on an infinite timescale, it will sample all possible states and the probability of finding the system in any state is the length of time is spends in that state divided by the total time the system exists. This time average is assumed to be equal to the ensemble average, although rigorous proof of this is still lacking.

Just as the grand canonical ensemble is described by its volume, temperature and chemical potential, a canonical ensemble is described by its volume, number of particles and temperature and the isothermal-isobaric ensemble is described by its pressure, number of particles and temperature, while the microcanonical ensemble is described by its volume, number of particles and internal energy. A given thermodynamic system is typically characterized most conveniently by one or another of these ensembles.

1.3 THE PARTITION FUNCTION

The probability of finding the system in any state is proportional to (1.2.1). In order to calculate that probability, we need to normalize (1.2.1) by dividing by the sum of the values of (1.2.1) for all possible states. The sum of expression (1.2.1) for all the microstates available to the system is known as the partition function:

$$\Xi = \sum_i e^{-\varepsilon_i/kT} \tag{1.3.1}$$

The evaluation of equation (1.3.1) begins with the Hamiltonian of the system:

$$H(\mathbf{r}^N, \mathbf{p}^N) = K_N(\mathbf{p}^N) + V_N(\mathbf{r}^N) + \phi_N(\mathbf{r}^N) \tag{1.3.2}$$

The Hamiltonian (H) describes the total energy of the system and is a sum of the kinetic (K), interparticle (V) and external (ϕ) energies. The energy of the system depends on the number of particles (N), their positions (**r**), and their momentums (**p**), where bold variables represent vectors. The value for energy (ε) in (1.2.1) and (1.3.1) is the Hamiltonian (1.3.2) with the contribution from the chemical potential subtracted. This term must be subtracted because as particles are added to the system they are taken from the surroundings, not created. If the chemical potential term were left in a state with an infinite number of particles, it would be found with a probability of 1.

With this expression for energy the probability of finding the system in each state becomes:

$$f_0(\mathbf{r}^N, \mathbf{p}^N; N) = \frac{e^{-\beta(H-N\mu)}}{\Xi} \tag{1.3.3}$$

Where f_0 is the ensemble probability density, $\beta = 1/kT$, and Ξ is now:

$$\Xi = \sum_{N=0}^{\infty} \frac{1}{h^{3N} N!} \int \int e^{-\beta(H-N\mu)} d\mathbf{r}^N d\mathbf{p}^N \tag{1.3.4}$$

The h^{3N} ensures that the partition function is dimensionless (where h is Planck's constant), and the N! corrects for overcounting. The contribution from the chemical potential does not depend on the momentums or positions, and can be pulled out of the integrals:

$$\Xi = \sum_{N=0}^{\infty} \frac{e^{N\beta\mu}}{h^{3N} N!} \int \int e^{-\beta H} d\mathbf{r}^N d\mathbf{p}^N \tag{1.3.5}$$

The kinetic portion of the Hamiltonian can be expressed as a function of temperature (rather than particles' momenta). Introducing the activity:

$$z = \frac{e^{\beta\mu}}{\Lambda^3} \tag{1.3.6}$$

where:

$$\Lambda = \sqrt{\frac{\beta h^2}{2\pi m}} \tag{1.3.7}$$

is the thermal de Broglie wavelength, and m is the mass of a particle; the partition function can then be simplified to:

$$\Xi = \sum_{N=0}^{\infty} \frac{z^N}{N!} \int e^{-\beta V_N} d\mathbf{r}^N \tag{1.3.8}$$

where V_N is the potential energy of the system due to interparticle interactions from (1.3.2) and no external forces are assumed ($\phi(\mathbf{r}^N) = 0$).

Knowing the probability of each of the states allows us to calculate expected values of observable quantities. If we are interested in a quantity, B, then the expected value would be an average over the ensemble, weighted by each states probability:

$$<B>=\sum_{N=0}^{\infty}\int\int\frac{Be^{-\beta(H-N\mu))}}{\Xi}d\mathbf{r}^N d\mathbf{p}^N \tag{1.3.9}$$

where the angled brackets indicate an ensemble average.

1.4 THE VIRIAL EXPANSION

The virial expansion is a direct outgrowth of the partition function. Here we shall make the simplifying assumption that the energy due to interparticle interactions is simply the sum of each pair of particles interactions with each other (this is an almost, but not quite, exact characteristic of many liquids and gases of interest):

$$V_N=\sum_{i=0}^{N-1}\sum_{j=i+1}^{N}u_{i,j}(\mathbf{r}) \tag{1.4.1}$$

Where $u_{i,j}(\mathbf{r})$ is the pair potential between particles i and j, and **r** is the vector between them. Then (1.3.8) becomes:

$$\Xi=\sum_{N=0}^{\infty}\frac{z^N}{N!}\int\prod_{i=0}^{N-1}\prod_{j=i+1}^{N}e^{-\beta u_{i,j}(\mathbf{r})} \tag{1.4.2}$$

For simplification we introduce the e-bond:

$$e_{i,j}=e^{-\beta u_{i,j}(\mathbf{r})} \tag{1.4.3}$$

and (1.4.2) becomes:

$$\Xi=1+z+\frac{z^2}{2}\int\int e_{1,2}d\mathbf{r_1}d\mathbf{r_2}+\frac{z^3}{6}\int\int\int e_{1,2}e_{2,3}e_{1,3}d\mathbf{r_1}d\mathbf{r_2}d\mathbf{r_3}+\ldots \tag{1.4.4}$$

Because the grand canonical partition function is the sum of many multidimensional integrals, many other quantities that are derived from the partition function also contain these integrals. As a result, it becomes convenient to express these integrals through diagrammatic representations. For example, the last term on the right hand side of (1.4.4) can be represented as:

(1.4.5)

In this representation each black circle represents a particle's position to be integrated over and the value of z for that particle. Each line represents an e-bond between the particles it connects. Implicit within the definition of the diagram is the factor (1/3!). The value of the diagram is the value of the integral, over all possible positions of the black circles, of the product of each of the lines and circles, divided by the number of ways to label the molecules (without changing the connectivity). Equation (1.4.4) can then be represented as:

(1.4.6)

A typical pair potential tends to zero as distance is increased, and as a result the e-bond tends to 1:

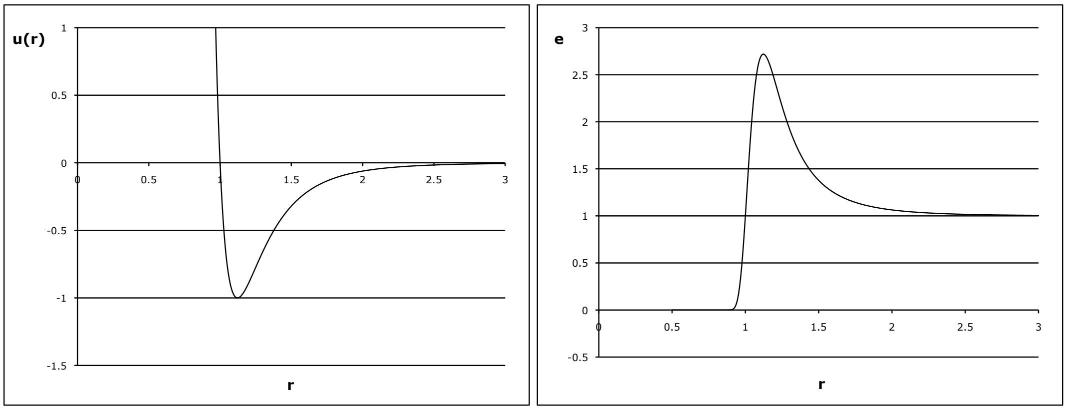

Figure 1.1 – The pair potential (u) and the corresponding e-bond of the Lennard-Jones potential graphed against interparticle distance (r).

This implies that the contribution from the Nth integral would be on the order of V^N, but it would be convenient if the integrands tended to zero as the distance was increased. We therefore introduce the f-bond:

$$f_{i,j} = e^{-\beta u_{i,j}(\mathbf{r})} - 1 \tag{1.4.7}$$

The f-bond tends to zero as distance is increased. Now we need to express (1.4.4) with f-bonds. This can be done by replacing each integral of N fully connected e-bonds with each unique diagram of N f-bonds. For example:

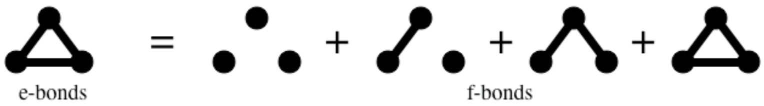

(1.4.8)

Note that the term on the left hand side (LHS) and the first and last terms on the right hand side (RHS) can each be labeled 3! ways, but the other 2 terms on the RHS can only be labeled 2 ways (without changing the connectivity). So the RHS is:

$$\frac{z^3}{3!}\int\int \mathbf{r_1} d\mathbf{r_2} d\mathbf{r_3} + \frac{z^3}{2}\int\int\int f_{1,2} d\mathbf{r_1} d\mathbf{r_2} d\mathbf{r_3} + \frac{z^3}{2}\int\int\int f_{1,2} f_{1,3} d\mathbf{r_1} d\mathbf{r_2} d\mathbf{r_3} + \frac{z^3}{3!}\int\int\int f_{1,2} f_{2,3} f_{1,3} d\mathbf{r_1} d\mathbf{r_2} d\mathbf{r_3} \tag{1.4.9}$$

or:

$$\frac{z^3}{3!}\int\int\int [1 + 3f_{1,2} + 3f_{1,2}f_{1,3} + f_{1,2}f_{2,3}f_{1,3}] \mathbf{r_1} d\mathbf{r_2} d\mathbf{r_3} \tag{1.4.10}$$

Looking at only the integrands:

$$1 + 3f_{1,2} + 3f_{1,2}f_{1,3} + f_{1,2}f_{2,3}f_{1,3} \tag{1.4.11}$$

$$= 1 + 3(e_{1,2} - 1) + 3(e_{1,2} - 1)(e_{1,3} - 1) + (e_{1,2} - 1)(e_{2,3} - 1)(e_{1,3} - 1) \tag{1.4.12}$$

$$\begin{aligned} &= 1 + 3e_{1,2} - 3 \\ &\quad +3e_{1,2}e_{1,3} - 3e_{1,2} - 3e_{1,3} + 3 \\ &\quad +e_{1,2}e_{2,3}e_{1,3} - e_{1,2}e_{2,3} - e_{1,2}e_{1,3} - e_{2,3}e_{1,3} + e_{1,2} + e_{2,3} + e_{1,3} - 1 \end{aligned} \tag{1.4.13}$$

Because the labels are arbitrary, so that all points are treated as identical, the integral over $e_{1,2} = e_{2,3} = e_{1,3}$ and likewise $e_{1,2}e_{1,3} = e_{1,2}e_{2,3} = e_{2,3}e_{1,3}$. So (1.4.13) simplifies to:

$$e_{1,2}e_{2,3}e_{1,3} \tag{1.4.14}$$

matching the integrand of LHS in (1.18).

With the e-bonds replaced by f-bonds the expression for the grand canonical partition function is now:

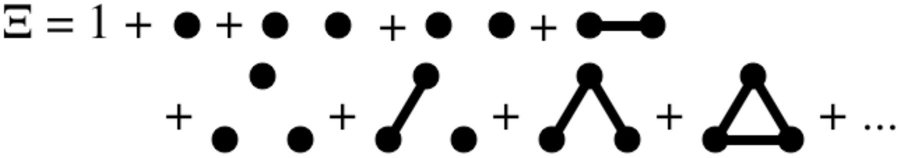

(1.4.15)

with the value of each black circle z, and the value of each black line the f-bond between the particles it connects. From this expression for the grand canonical partition function it is possible to derive expressions for many important thermodynamic quantities in the form of similar integrals; such as the excess chemical potential. The excess chemical potential (μ^{ex}) is the value the chemical potential (μ) is in excess over the chemical potential of an ideal gas (μ^{id}):

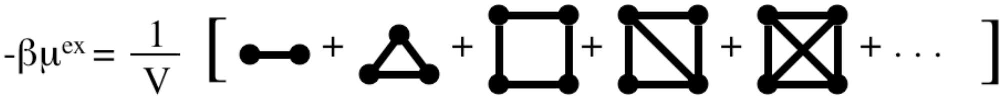

(1.4.16)

here the lines are still f-bonds, but the circles represent the density (ρ). The inverse volume term at the beginning of the RHS can be excluded by holding the position of the first particle fixed and integrating over all possible positions of the other particles.

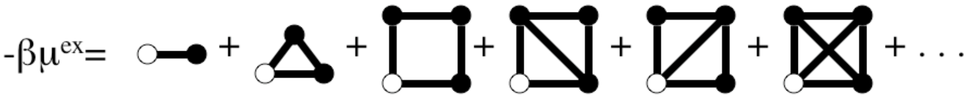

(1.4.17)

The white circles represent a particle with fixed position and still have the value of the number density (ρ). Note that there are 2 choices for the particle to be fixed in the fourth integral in (1.4.16) (a particle with 2 bonds or a particle with 3 bonds), so the integral must be performed twice, but the fourth and fifth integral in (1.4.17) will have the same value so the integral can be performed once and doubled. Expressed in the conventional format:

$$\beta\mu^{ex} = -\sum_{i=1}^{\infty} \beta_i \rho^i \tag{1.4.18}$$

The coefficients β_i represent the sum of all integrals in (1.4.17) with i+1 particles. The virial expansion can be derived from (1.4.18). First we need expressions for the chemical potential and pressure of the ideal gas:

$$\beta\mu^{id} = \ln[\Lambda^3 \rho] \tag{1.4.19}$$

$$\beta P^{id} = \rho \tag{1.4.20}$$

The path from chemical potential to pressure follows from:

$$\left(\frac{\partial P}{\partial \rho}\right)_T = \rho \left(\frac{\partial \mu}{\partial \rho}\right)_T \tag{1.4.21}$$

From (1.4.19) and (1.4.18):

$$\beta\mu = \ln[\Lambda^3 \rho] - \sum_{i=1}^{\infty} \beta_i \rho^i \tag{1.4.22}$$

making β times the RHS of (1.4.21) :

$$\rho \left[\frac{1}{\rho} - \beta_1 - 2\beta_2\rho - 3\beta_3\rho^2 - ...\right] = 1 - \beta_1\rho - 2\beta_2\rho^2 - 3\beta_3\rho^3 - ... \tag{1.4.23}$$

Integrating with respect to density, we obtain an expression for βP:

$$\beta P = \rho - \frac{1}{2}\beta_1\rho^2 - \frac{2}{3}\beta_2\rho^3 - \frac{3}{4}\beta_3\rho^4 - ... \tag{1.4.24}$$

or:

$$\beta P = \rho - \sum_{i=1}^{\infty} \frac{i}{i+1} \beta_i \rho^{i+1} \tag{1.4.25}$$

Perhaps the most important aspect of (1.4.25) is that the only assumption made in its derivation is that the pair potential is pairwise additive (1.4.1), which, as noted earlier, is typically a very good approximation, thus it is nearly ubiquitous in integral-equation theory.

Even the most successful predictions of real systems usually have many assumptions or approximations in their derivation. For this reason, equation (1.4.25) has been a mainstay of statistical thermodynamics. It is always possible to increase the accuracy of a theory by calculating more coefficients (although this comes with increasing difficulty). It has been extensively studied, and it can be used as a measuring stick for other approximations. For example, other other approximations often give quantitatively correct phase diagram information, but fail to accurately calculate virial coefficients.

1.5 PAIR POTENTIAL

The primary difference between real systems and ideal gases is the interactions between the molecules. The interaction between two individual molecules can be described as a function of the distance between them and their orientation by a pair potential. Real particles have a strong repulsive interaction at short distances, a weaker attractive interaction at intermediate distances, and virtually no interaction at great distances. True pair potentials can be described by complex formulas, which may not be appropriate when performing statistical calculations for systems with a large number of particles.

1.6 HARD SPHERE AND SQUARE-WELL MODELS

It is often useful to make an approximation to the pair potential when studying the thermodynamics of a large system. Arguably the simplest and most studied model for a pair potential is the hard sphere (HS) model. In a HS model $u(\mathbf{r})$ is independent of orientation ($u(\mathbf{r})=u(r)$). Inside the hard sphere diameter (σ) $u(r)$ is infinitely repulsive and outside it is zero.

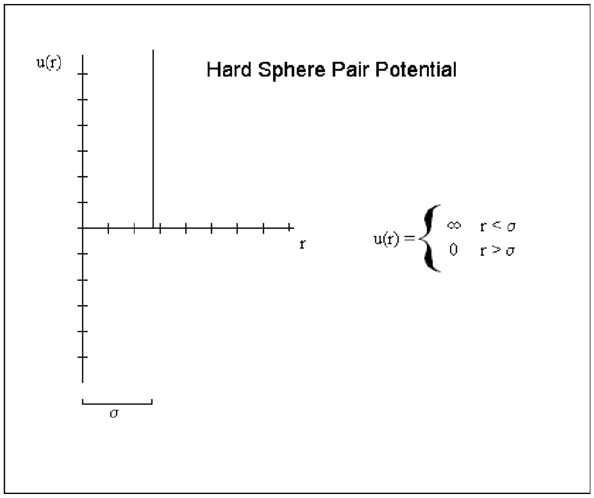

Figure 1.2 – The hard sphere pair potential graphed against interparticle distance.

The simple form of the hard sphere model makes it the most studied and well-understood pair potential in statistical thermodynamics. However, the most notable feature missing from this model is the attractive portion of the pair potential of a real molecule. The hard sphere model is a fair approximation to the gas phase and has been found to undergo an entropy-driven fluid-solid transition. The hard sphere model does not, however, predict a liquid phase. The gaseous phase is dominated by intraparticle potentials. The solid phase is dominated by repulsive interactions, and liquid phase is dominated by attractive interactions. The liquid phase has been the hardest for scientist to completely understand. In order to study the liquid phase a more complicated model is needed.

The simplest pair potential model with an attractive portion is the square-well potential. The square-well model incorporates the repulsive and attractive parts of the pair potential while maintaining mathematical simplicity. It is a step-wise function with a hard-core, and an attractive well. Figure 1.3 shows a generalized square-well potential.

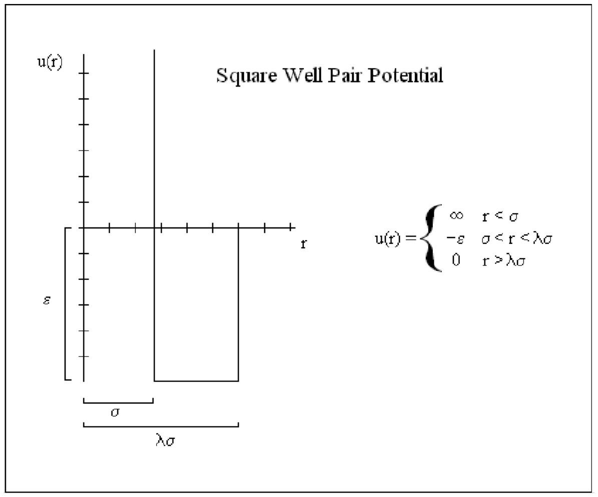

Figure 1.3 – The square-well potential graphed against interparticle distance.

The parameters that describe the square-well potential are the well depth (ε), the hard-core diameter (σ), and the well width (described relative to the hard-core diameter by λ). Because the thermodynamics of this model depend on the dimensions of the square-well only in a relative way, σ may be taken to be unity (or more precisely, we can use units of σ to describe length).

1.7 SECOND VIRIAL COEFFICIENT

The virial expansion (1.4.25) can also be expressed in terms of virial coefficients:

$$\frac{P}{kT} = \rho + B(T)\rho^2 + C(T)\rho^3 + D(T)\rho^4 + ... \tag{1.7.1}$$

where B(T) is the second virial coefficient, C(T) is the third, and so on. And from (1.4.24) and (1.4.25):

$$B(T) = -\frac{1}{2}\beta_1 \tag{1.7.2}$$

$$C(T) = -\frac{2}{3}\beta_2 \tag{1.7.3}$$

From (1.4.17) and (1.7.2):

$$B(T) = -\frac{1}{2}\beta_1 = -\frac{1}{2} \; \bullet\!\!-\!\!\bullet \; = -\frac{1}{2}\int f_{1,2}\; d\mathbf{r_2} \tag{1.7.4}$$

In the case of a spherically symmetric potential (1.7.4) becomes:

$$B(T) = -2\pi \int_0^\infty f_{1,2}\; dr \tag{1.7.5}$$

where r is the distance between particles 1 and 2.

For the hard sphere model:

$$u(r) = \begin{cases} \infty & r < \sigma \\ 0 & r > \sigma \end{cases} \tag{1.7.6}$$

making the f-bond from (1.4.7):

$$f(r) = \begin{cases} -1 & r < \sigma \\ 0 & r > \sigma \end{cases} \tag{1.7.7}$$

From (1.7.7) and (1.7.5):

$$B_{HS}(T) = \frac{2\pi\sigma^3}{3} \tag{1.7.8}$$

The value of (1.7.8) is used frequently as a reference to describe other virial coefficients, and is represented as b_0.

For the square-well, recall that the potential is defined as:

$$u(r) = \begin{cases} \infty & r < \sigma \\ -\varepsilon & \sigma < r < \lambda\sigma \\ 0 & r > \lambda\sigma \end{cases} \tag{1.7.9}$$

making the f-bond for a square-well:

$$f(r) = \begin{cases} -1 & r < \sigma \\ h & \sigma < r < \lambda\sigma \\ 0 & r > \lambda\sigma \end{cases} \tag{1.7.10}$$

where:

$$h = e^{\varepsilon/kT} - 1 \tag{1.7.11}$$

With (1.7.10) substituted into (1.7.5):

$$B_{SW}(T) = -2\pi\left[-\int_0^{\sigma} r^2 dr + h\int_{\sigma}^{\lambda\sigma} r^2 dr\right] \tag{1.7.12}$$

which is:

$$B_{SW}(T) = -2\pi\left[\frac{-\sigma^3}{3} + \frac{h}{3}(\lambda^3\sigma^3 - \sigma^3)\right] \tag{1.7.13}$$

or:

$$B_{SW}(T) = \frac{2\pi}{3}\left[\sigma^3 - h(\lambda^3\sigma^3 - \sigma^3)\right] \tag{1.7.14}$$

In terms of (1.7.8), (1.7.14) becomes:

$$\frac{B_{SW}(T)}{b_0} = 1 - h(\lambda^3 - 1) \tag{1.7.15}$$

1.8 THIRD VIRIAL COEFFICIENT FROM FOURIER TRANSFORM

The third virial coefficient for a hard sphere potential was solved by Boltzmann in 1909[1]:

$$\frac{C_{HS}(T)}{b_0^2} = \frac{5}{8} \tag{1.8.1}$$

Hauge[2] solved the third virial coefficient for a square-well utilizing a Fourier transform. If we recall from (1.4.18):

$$\beta_2 = \frac{1}{2}\int\int f(r_{12})f(r_{13})f(r_{23})d\vec{r}_{12}d\vec{r}_{13} \tag{1.8.2}$$

With a Fourier transform $\tilde{f}(k)$ is defined as:

$$\tilde{f}(k) = \int \mathrm{d}\vec{r}\; e^{i\vec{k}\vec{r}} f(r) \tag{1.8.3}$$

The tilde (~) over the f(k) here shows that f(k) is not the same function as f(r) but is related through the Fourier transform. The reverse Fourier transform is

$$f(r) = \int \frac{\mathrm{d}\vec{k}}{(2\pi)^3}\; e^{-i\vec{k}\vec{r}}\tilde{f}(k) \tag{1.8.4}$$

So:

$$f(r_{12}) = \int \frac{\mathrm{d}\vec{k}}{(2\pi)^3}\; e^{-i\vec{k}\vec{r}_{12}}\tilde{f}(k) \tag{1.8.5}$$

$$f(r_{13}) = \int \frac{\mathrm{d}k'}{(2\pi)^3}\; e^{-i\vec{k}'\vec{r}_{13}}\tilde{f}(k') \tag{1.8.6}$$

$$f(r_{23}) = \int \frac{\mathrm{d}k''}{(2\pi)^3}\; e^{-i\vec{k}''\vec{r}_{23}}\tilde{f}(k'') \tag{1.8.7}$$

Substituting (1.8.5)-(1.8.7) into (1.8.2):

$$\beta_2 = \frac{1}{2}\int \frac{\mathrm{d}\vec{k}}{(2\pi)^3}\int \frac{\mathrm{d}\vec{k}'}{(2\pi)^3}\int \frac{\mathrm{d}\vec{k}''}{(2\pi)^3}\;\tilde{f}(k)\tilde{f}(k')\tilde{f}(k'')\int \mathrm{d}\vec{r}_{12}\int \mathrm{d}\vec{r}_{13}\, e^{-i\vec{k}\vec{r}_{12}}e^{-i\vec{k}'\vec{r}_{13}}e^{-i\vec{k}''\vec{r}_{23}} \tag{1.8.8}$$

The primes (‘,’’) following the k ’s show that as one type is varied in its integral, the others are not. Understanding that:

$$\vec{r}_{23} = \vec{r}_2 - \vec{r}_3 = \vec{r}_2 - \vec{r}_1 + \vec{r}_1 - \vec{r}_3 = -\vec{r}_{12} + \vec{r}_{13} \tag{1.8.9}$$

(1.8.8) may be changed to:

$$\beta_2 = \frac{1}{2}\int \frac{\mathrm{d}\vec{k}}{(2\pi)^3}\int \frac{\mathrm{d}\vec{k}'}{(2\pi)^3}\int \frac{\mathrm{d}\vec{k}''}{(2\pi)^3}\;\tilde{f}(k)\tilde{f}(k')\tilde{f}(k'')\int \mathrm{d}\vec{r}_{12}\int \mathrm{d}\vec{r}_{13}\, e^{-i\vec{k}\vec{r}_{12}}e^{-i\vec{k}'\vec{r}_{13}}e^{i\vec{k}''\vec{r}_{12}}e^{-i\vec{k}''\vec{r}_{13}} \tag{1.8.10}$$

Taking the last part of (1.8.10) and defining it as X, we have:

$$X = \int \mathrm{d}\vec{r}_{12}\int \mathrm{d}\vec{r}_{13}\; e^{-i\vec{k}\vec{r}_{12}}e^{-i\vec{k}'\vec{r}_{13}}e^{i\vec{k}''\vec{r}_{12}}e^{-i\vec{k}''\vec{r}_{13}} \tag{1.8.11}$$

or:

$$X = \left(\int \mathrm{d}\vec{r}_{12}\; e^{-i(\vec{k}-\vec{k}'')\vec{r}_{12}}\right)\left(\int \mathrm{d}\vec{r}_{13}\; e^{-i(\vec{k}'+\vec{k}'')\vec{r}_{13}}\right) \tag{1.8.12}$$

The Dirac delta function is defined as:

$$\delta(x) = \int_{-\infty}^{\infty} \frac{\mathrm{d}s}{2\pi} e^{-isx} \tag{1.8.13}$$

or in three dimensions:

$$\delta(\vec{x}) = \int \frac{\mathrm{d}\vec{s}}{(2\pi)^3} e^{-i\vec{s}\vec{x}} \tag{1.8.14}$$

A comparison of (1.8.12) and (1.8.14) reveals:

$$X = (2\pi)^6 \delta(\vec{k} - \vec{k}'')\delta(\vec{k}' + \vec{k}'') \tag{1.8.15}$$

Substituting back into (1.8.10) we have:

$$\beta_2 = \frac{1}{2} \int \mathrm{d}\vec{k} \int \mathrm{d}\vec{k}' \int \frac{\mathrm{d}\vec{k}''}{(2\pi)^3}\ \tilde{f}(k)\tilde{f}(k')\tilde{f}(k'')\delta(\vec{k} - \vec{k}'')\delta(\vec{k}' + \vec{k}'') \tag{1.8.16}$$

The terms not involving k’’ can be pulled out of the integral, and $\delta(\vec{k} - \vec{k}'')$ becomes $\delta(\vec{k} + \vec{k}')$ because of the nature of the delta function. An integral over a Dirac delta function, δ(x), that starts at x<0 and goes to x>0 will return a value of 1. So (1.8.16) becomes:

$$\beta_2 = \frac{1}{2}\frac{1}{(2\pi)^3} \int \mathrm{d}\vec{k} \int \mathrm{d}\vec{k}'\ \tilde{f}(k)\tilde{f}(k')\delta(\vec{k} + \vec{k}') \int \mathrm{d}\vec{k}''\ \tilde{f}(k'')\delta(\vec{k}' + \vec{k}'') \tag{1.8.17}$$

And because of the definition of the delta function:

$$\int \mathrm{d}\vec{k}''\ \tilde{f}(k'')\delta(\vec{k}' + \vec{k}'') = \tilde{f}(-k') \tag{1.8.18}$$

making (1.8.17):

$$\beta_2 = \frac{1}{2}\frac{1}{(2\pi)^3} \int \mathrm{d}\vec{k}\ \tilde{f}(k) \int \mathrm{d}\vec{k}'\ \tilde{f}(k')\tilde{f}(-k')\delta(k + k') \tag{1.8.19}$$

but:

$$\int \mathrm{d}\vec{k}'\ \tilde{f}(k')\tilde{f}(-k')\delta(\vec{k} + \vec{k}') = \tilde{f}(-k)\tilde{f}(k) \tag{1.8.20}$$

so (1.8.19) is:

$$\beta_2 = \frac{1}{2}\frac{1}{(2\pi)^3}\int d\vec{k}\ \tilde{f}(k)\tilde{f}(-k)\tilde{f}(k) \tag{1.8.21}$$

Recall that:

$$\tilde{f}(k) = \int \mathrm{d}\vec{r}\ e^{i\vec{k}\vec{r}} f(r) \tag{1.8.22}$$

So the complex conjugate would be:

$$\tilde{f}(k)^* = \int \mathrm{d}\vec{r}\ \left(e^{i\vec{k}\vec{r}}\right)^* f(r) = \int \mathrm{d}\vec{r}\ e^{-i\vec{k}\vec{r}} f(r) = \tilde{f}(-k) \tag{1.8.23}$$

making (1.8.21):

$$\beta_2 = \frac{1}{2}\frac{1}{(2\pi)^3}\int \mathrm{d}\vec{k}\ \tilde{f}(k)^2\tilde{f}(k)^* = \frac{1}{2}\frac{4\pi}{(2\pi)^3}\int \mathrm{d}k\ k^2\tilde{f}(k)^2\tilde{f}(k)^* = \frac{1}{4\pi^2}\int \mathrm{d}k\ k^2\tilde{f}(k)^2\tilde{f}(k)^* \tag{1.8.24}$$

And from the Jacobian:

$$\begin{aligned}\tilde{f}(k) = \int \mathrm{d}\vec{r}\ e^{i\vec{k}\vec{r}} f(r) &= \int_0^\infty dr\ r^2 \int_0^\pi \mathrm{d}\theta\ sin\theta \int_0^{2\pi} \mathrm{d}\phi\ e^{ikrcos\theta} f(r) \\ &= 2\pi \int_0^\infty \mathrm{d}r\ r^2 f(r) \int_0^\pi \mathrm{d}\theta\ sin\theta e^{ikrcos\theta}\end{aligned} \tag{1.8.25}$$

Letting t be defined as:

$$t = cos\theta \qquad\qquad \mathrm{d}t = -sin\theta\mathrm{d}\theta \tag{1.8.26}$$

(1.8.25) becomes

$$\begin{aligned}\tilde{f}(k) &= 2\pi\int_0^\infty \mathrm{d}r\ r^2 f(r)\left[-\int_1^{-1}\mathrm{d}t\ e^{ikrt}\right] = 2\pi\int_0^\infty \mathrm{d}r\ r^2 f(r)\left[\int_{-1}^{1}\mathrm{d}t\ e^{ikrt}\right] \\ &= 2\pi\int_0^\infty \mathrm{d}r\ r^2 f(r)\left[\frac{1}{ikr}\left(e^{ikr}-e^{-ikr}\right)\right] = \frac{4\pi}{k}\int_0^\infty \mathrm{d}r\ rf(r)sin(kr)\end{aligned} \tag{1.8.27}$$

The last step is a result of Euler's formula. Because k is real in the final f form of (1.8.27) it is shown that

$$\tilde{f}(k) = \tilde{f}(k)^* \tag{1.8.28}$$

Simplifying (1.8.24) to:

$$\beta_2 = \frac{1}{4\pi^2}\int \mathrm{d}k\ k^2 \tilde{f}(k)^3 \tag{1.8.29}$$

Substituting (1.7.10) into (1.8.27) one finds for a square-well:

$$\tilde{f}(k) = \frac{-4\pi}{k}\int_0^{\sigma} \mathrm{d}r\ rsin(kr) + \frac{4\pi}{k}h\int_{\sigma}^{\lambda\sigma} \mathrm{d}r\ rsin(kr) \tag{1.8.30}$$

Using the mathematics program Maple®, we evaluated (1.80) and substituted it into (1.8.29). The result was then substituted into (1.7.3):

$$\begin{aligned} \frac{C(T)}{b_0^2} = -\frac{1}{8}\{-5 & \\ +h \quad & [\tfrac{1}{2}\lambda^6 - \tfrac{1}{2}sign(\lambda\sigma - 2\sigma)\lambda^6 - 9\lambda^4 + 9sign(\lambda\sigma - 2\sigma)\lambda^4 \\ & +16\lambda^3 - 16sign(\lambda\sigma - 2\sigma)\lambda^3 + 1 + 16sign(\lambda\sigma - 2\sigma)] \\ +h^2 \quad & [\lambda^6 - sign(\lambda\sigma - 2\sigma)\lambda^6 - 18\lambda^4 + 18sign(\lambda\sigma - 2\sigma)\lambda^4 \\ & -32sign(\lambda\sigma - 2\sigma)\lambda^3 + 18\lambda^2 + 16 + 32sign(\lambda\sigma - 2\sigma)] \\ +h^3 \quad & [\tfrac{11}{2}\lambda^6 - \tfrac{1}{2}sign(\lambda\sigma - 2\sigma)\lambda^6 - 9\lambda^4 + 9sign(\lambda\sigma - 2\sigma)\lambda^4 \\ & -16\lambda^3 - 16sign(\lambda\sigma - 2\sigma)\lambda^3 + 18\lambda^2 + 10 \\ & +16sign(\lambda\sigma - 2\sigma)] \\ \} & \end{aligned} \tag{1.8.31}$$

In (1.8.31) the function “sign(x)” returns a value of unity with the same sign as x. The operand (λσ-2σ) will be positive for a well width greater than the hardcore diameter (λ>2) and negative for a well width less than the hardcore diameter (λ<2). For (λ=2) (1.8.31) gives the same answer for sign(x) = 1 as it does for sign(x) = -1. This is the result presented by Hauge. With the sign() function evaluated (1.8.31) becomes:

$$\begin{aligned} \frac{C(T)}{b_0^2} = \frac{-1}{8}\{-5 & \\ & +h\left[\lambda^6 - 18\lambda^4 + 32\lambda^3 - 15\right] \\ & +h^2\left[2\lambda^6 - 36\lambda^4 + 32\lambda^3 + 18\lambda^2 - 16\right] \\ & +h^3\left[6\lambda^6 - 18\lambda^4 + 18\lambda^2 - 6\right] \end{aligned}$$

$$\} \qquad \lambda < 2$$

$$\frac{C(T)}{b_0^2} = \frac{-1}{8}\left\{-5 + 17h + h^2\left[-32\lambda^3 + 18\lambda^2 + 48\right]\right.$$
$$\left. + h^3\left[5\lambda^6 - 32\lambda^3 + 18\lambda^2 + 26\right]\ \right\} \qquad \lambda > 2 \qquad (1.8.32)$$

1.9 THIRD VIRIAL COEFFICIENT FROM VOLUME OF OVERLAPPING SPHERES

The third virial coefficient for the hard sphere can also be thought of as the volume of all possible positions of the third sphere for all configurations of 3 overlapping spheres in which the first sphere is fixed at the origin, and sphere 2 and 3 are allowed to take any position as long as the center of any sphere is within the volume enclosed by the other two.

Since the first sphere has its position fixed at the origin we must begin with the second sphere. Let us start by assuming the second sphere is centered on the x-axis (or from another perspective, choose the x-axis such that it passes through the center of spheres 1 and 2).

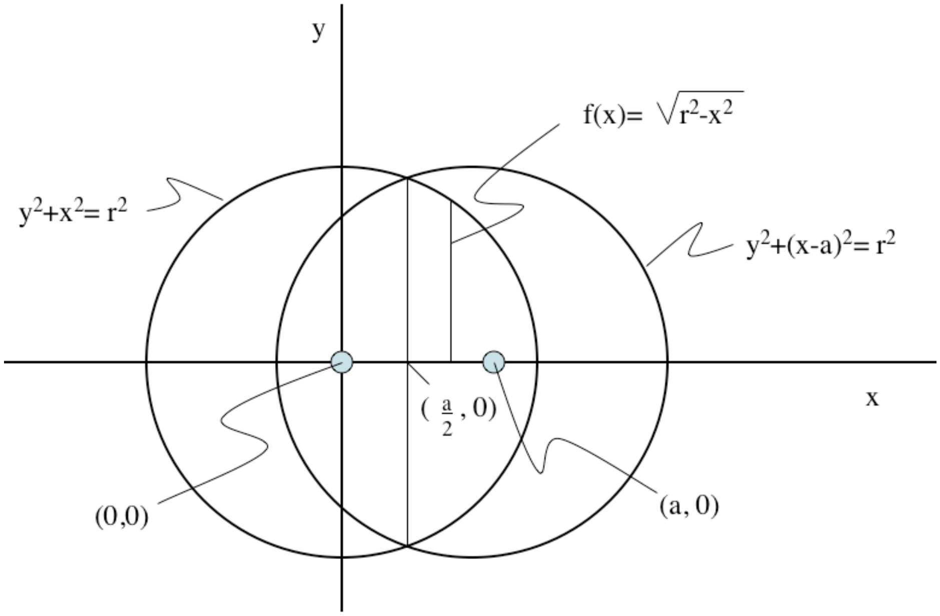

Figure 1.4 – Two overlapping circles.

If we call the distance between the two spheres ‘a’ and the radius of the spheres ‘r’, then the equations that describe the surfaces in the x-y plane are:

$$y^2 + x^2 = r^2 \tag{1.9.1}$$

$$y^2 + (x-a)^2 = r^2 \tag{1.9.2}$$

The center of the third sphere can be any point within the volume of overlap between the first two spheres. This can be understood by examining the cluster integral (1.8.2). The integrand is $(-1)^3$ when the distances $r_{1,2}$, $r_{1,3}$, and $r_{2,3}$ are less than or equal to the hard sphere diameter (σ) and is zero everywhere else. Since the integral is constant, we only need the volume in which the integrand is non-negative, or the volume available to a third sphere when two spheres are placed around one centered at the origin such that all centers fall within each other's bounds.

Since the center of sphere 2 is at (a,0,0), the volume available to the third sphere is bisected with a plane at x=a/2. If we can calculate the volume on one half of the plane, we can double it to find the volume available to the third sphere with the second at (a,0,0). The height of the curve that bounds the volume on the right half is a function of x:

$$f(x) = \sqrt{r^2 - x^2} \tag{1.9.3}$$

We now need the volume bounded by x=a/2 to the left, f(x) to the top, -f(x) to the bottom, and x=r to the right. This can be calculated by rotating f(x) around the x-axis on the interval a/2 to r. The general form of the volume produced when a radius, R(x), is rotated around the x-axis (disk integration) is:

$$V = \pi \int_a^b [R(x)]^2 \, dx \tag{1.9.4}$$

Remembering that this will be half the volume we are interested in (because we ignored the volume to the left of x=a/2):

$$\begin{aligned} \frac{1}{2}V &= \pi \int_{\frac{a}{2}}^{r} [f(x)]^2 \, dx = \pi \int_{\frac{a}{2}}^{r} \left(\sqrt{r^2 - x^2}\right)^2 dx \\ &= \pi \int_{\frac{a}{2}}^{r} \left(r^2 - x^2\right) dx = \pi \left[r^2 x - \frac{x^3}{3}\right]_{\frac{a}{2}}^{r} = \pi \left[r^3 - \frac{r^3}{2} - \frac{r^2 a}{2} + \frac{a^3}{24}\right] \end{aligned} \tag{1.9.5}$$

or, for the total volume (V):

$$V = 2\pi\left(\frac{2r^3}{3} - \frac{r^2 a}{2} + \frac{a^3}{24}\right) \tag{1.9.6}$$

This is only the value of the volume for one position of sphere 2, but sphere 2 can be anywhere within sphere 1. We must now integrate (1.9.6) over all positions of sphere 2. For the case of the hard sphere, r = σ and a can have any value less than or equal to σ. From (1.7.3) and (1.8.2):

$$C(T) = -\frac{1}{3}\int\int f_{1,2}f_{1,3}f_{2,3}d\mathbf{r_2}d\mathbf{r_3} \tag{1.9.7}$$

Since the integrand can only be $(-1)^3$ or zero, we know C(T) will be positive. If we now use the variable r to describe the distance between the centers of sphere 1 and sphere 2, not to be confused with the radius of spheres above, then using (1.9.6) to solve (1.9.7):

$$\begin{aligned} C_{HS}(T) &= \frac{1}{3}\int V d\mathbf{r_2} = \frac{4\pi}{3}\int V r^2 dr \\ &= \frac{4\pi}{3}\int_0^\sigma 2\pi\left(\frac{2\sigma^3}{3} - \frac{\sigma^2 r}{2} + \frac{r^3}{24}\right) r^2\,dr = \frac{8\pi^2}{3}\int_0^\sigma \left(\frac{2\sigma^3 r^2}{3} - \frac{\sigma^2 r^3}{2} + \frac{r^5}{24}\right) dr \\ &= \frac{8\pi^2}{3}\left[\frac{2\sigma^3 r^3}{9} - \frac{\sigma^2 r^4}{8} + \frac{r^6}{144}\right]_0^\sigma = \frac{8\pi^2}{3}\left[\frac{2\sigma^6}{9} - \frac{\sigma^6}{8} + \frac{\sigma^6}{144}\right] \\ &= \frac{8\pi^2\sigma^6}{3}\left(\frac{32-18+1}{144}\right) = \frac{5\pi^2\sigma^6}{18} = \frac{5}{8}b_0^2 \end{aligned} \tag{1.9.8}$$

which reproduces Boltzmann's[1] result from (1.8.1). The next step is applying this to method to the square-well potential.

As in the case of the hard sphere potential, the cluster integrals that describe the virial coefficients for the square-well potential are constant over different regions of the integral. The integrals can therefore be reduced to a sum of the product of the value of the integrand, the volume of space it takes that value, and any constants in front of the integral for each integrand value.

For the third virial coefficient, the integrand ($f_{1,2}f_{1,3}f_{2,3}$) can take the values (-1*-1*-1), (-1*-1*h), (-1*h*h), and (h*h*h), where h is defined in (1.7.10). We ignore the permutations for now, but account for them later. For the square-well potential we imagine the overlap of three spheres with an inner and outer radius.

The inner radius is the hard-core and has the value σ_1 and the outer radius is the well width ($\lambda\sigma_1$) or σ_2.

We must calculate the volume for each value of the integrand separately. Starting with (-1*-1*-1):

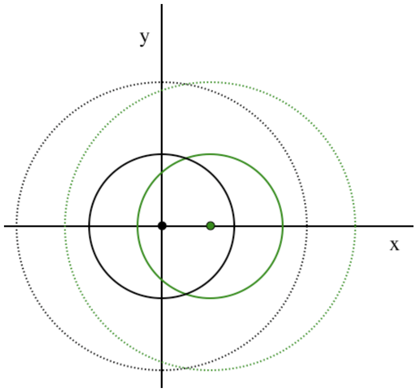

Figure 1.5 – Cross section of two overlapping square-well potentials within the hard-core radius.

From the figure, we can see that the problem reduces to that of a hard sphere. We also note, that the total of all the volumes of interest is the volume from the hard sphere case, with a hard-core diameter equal to σ_2. Or, if we define I_1 as the contribution of the (-1*-1*-1) case to $C_{SW}(T)$:

$$I_1 = \frac{5}{8} b_0^2 \tag{1.9.9}$$

Next, we consider the case when the integrand is (-1*-1*h), with its contribution being I_2. We chose the $f_{1,2}$-bond to be the bond that equals h. Since we will still integrate over all possible positions, and the labels are for convenience, this does not affect the value of the integral, although we still need to account for permutations later.

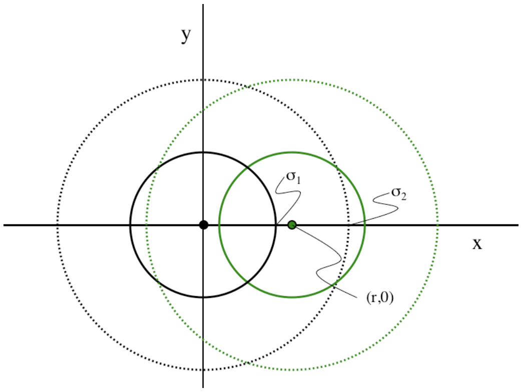

Figure 1.6 - Cross section of two overlapping square-well potentials outside the hard-core radius.

The center of the third sphere has the available volume bounded by the overlap of the two inner spheres (radii σ_1) because $f_{1,3}$ and $f_{2,3}$ must be –1. This volume may still be described by (1.9.6). The lower bound for the distance between 1 and 2 (r) is σ_1, but the upper bound depends on the value of σ_2 as shown in figure 1.7.

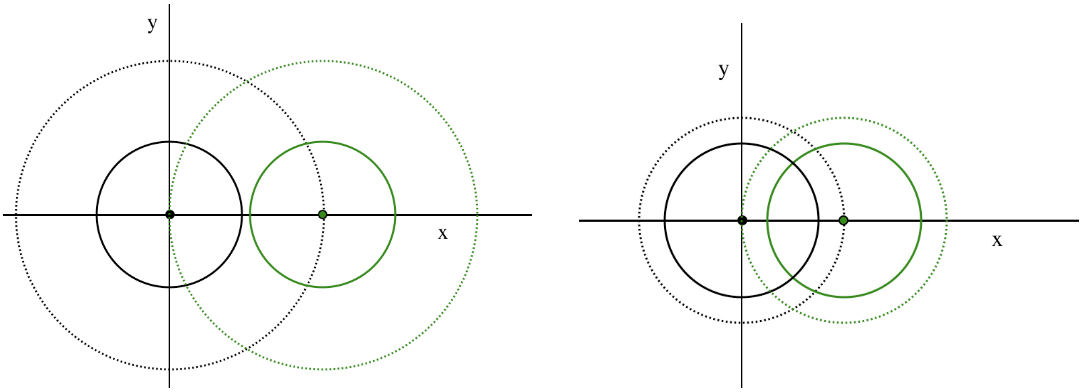

Figure 1.7 - Cross section of two overlapping square-well potentials outside the hard-core radius for $\lambda>2$ and $\lambda<2$.

For $2\sigma_1 < \sigma_2$, the upper bound of r is $2\sigma_1$ and for $2\sigma_1 > \sigma_2$, the upper bound is σ_2, or more generally $\sigma_1 \leq r \leq \min(2\sigma_1, \sigma_2)$.

Now we must account for the permutations. Since the integrand's value can come from (-1*-1*h) or (-1*h*-1) or (h*-1*-1), we must multiply our result by 3. So from (1.9.7) we have:

$$I_2 = 3h\left(-\frac{4\pi}{3}\right)\int_{\sigma_1}^{min(2\sigma_1,\sigma_2)} Vr^2dr \tag{1.9.10}$$

Substituting (1.9.6) into (1.9.10):

$$I_2 = -4\pi h\int_{\sigma_1}^{min(2\sigma_1,\sigma_2)} 2\pi\left(\frac{2\sigma_1^3}{3}-\frac{\sigma_1^2 r}{2}+\frac{r^3}{24}\right)r^2dr = -8\pi^2 h\int_{\sigma_1}^{min(2\sigma_1,\sigma_2)}\left(\frac{2\sigma_1^3r^2}{3}-\frac{\sigma_1^2r^3}{2}+\frac{r^5}{24}\right)dr$$

$$= -8\pi^2 h\left[\frac{2\sigma_1^3r^3}{9}-\frac{\sigma_1^2r^4}{8}+\frac{r^6}{144}\right]_{\sigma_1}^{min(2\sigma_1,\sigma_2)} \tag{1.9.11}$$

Recalling that $\lambda\sigma_1 = \sigma_2$, and solving (1.9.11) for $\lambda>2$ ($\min(2\sigma_1, \sigma_2) = 2\sigma_1$):

$$I_2 = -8\pi^2 h\left[\frac{2\sigma_1^3r^3}{9}-\frac{\sigma_1^2r^4}{8}+\frac{r^6}{144}\right]_{\sigma_1}^{2\sigma_1} = -8\pi^2\sigma_1^6 h\left[\frac{2}{9}2^3-\frac{1}{8}2^4+\frac{2^6}{144}-\frac{2}{9}+\frac{1}{8}-\frac{1}{144}\right]$$

$$= \frac{-8\pi^2\sigma_1^6 h}{144}\left[256-288+64-32+18-1\right] = -\frac{b_0^2}{8}(17h) \qquad \lambda>2 \tag{1.9.12}$$

And for λ<2 ($\min(2\sigma_1, \sigma_2) = \sigma_2 = \lambda\sigma_1$):

$$I_2 = -8\pi^2 h \left[\frac{2\sigma_1^3 r^3}{9} - \frac{\sigma_1^2 r^4}{8} + \frac{r^6}{144}\right]_{\sigma_1}^{\lambda\sigma_1} = -8\pi^2\sigma_1^6 h \left[\frac{2\lambda^3}{9} - \frac{\lambda^4}{8} + \frac{\lambda^6}{144} - \frac{2}{9} + \frac{1}{8} - \frac{1}{144}\right]$$

$$= \frac{-8\pi^2\sigma_1^6 h}{144}\left[32\lambda^3 - 18\lambda^4 + \lambda^6 - 32 + 18 - 1\right] = -\frac{b_0^2}{8} h\left[\lambda^6 - 18\lambda^4 + 32\lambda^3 - 15\right]$$

λ<2 (1.9.13)

Next we examine the integrand value of (-1*h*h) and define its contribution to C(T) as I_3. Again, we must consider the cases λ>2 and λ<2 separately. As always, they should converge for the case λ=2. We choose the $f_{1,2}$-bond to have the value -1. The distance between spheres 1 and 2 must be less than the hard-core radius, $0 \le r \le \sigma_1$.

First we look at λ>2:

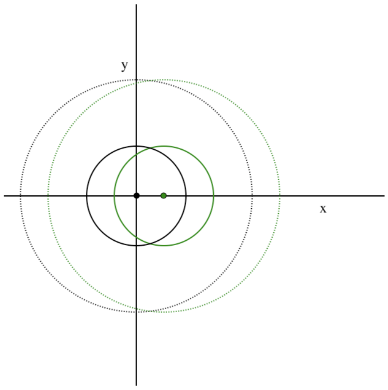

Figure 1.8 - Cross section of two overlapping square-well potentials within the hard-core radius for λ>2.

The center of sphere 3 must be placed within the two outer shells of sphere 1 and 2. We can see that this volume is the volume of overlap of sphere with radius σ_2 minus the volume of the two smaller spheres. The volume displaced by the two smaller spheres is 2 times the volume of the spheres minus their overlap volume. Then, introducing the notation for the volume of overlap of two spheres with radii σ_i and $\sigma_j \equiv V_{i,j}$ and the notation for the volume of a sphere with radius $\sigma_i \equiv V_i$:

$$V = V_{2,2} - 2V_1 + V_{1,1} \tag{1.9.14}$$

$V_{2,2}$ and $V_{1,1}$ are calculated using (1.9.6) and V_1 is simply the volume of a sphere ($4/3\pi r^3$):

$$V = 2\pi\left(\frac{2\sigma_2^3}{3} - \frac{\sigma_2^2 r}{2} + \frac{r^3}{24}\right) - 2\left(\frac{4}{3}\pi\sigma_1^3\right) + 2\pi\left(\frac{2\sigma_1^3}{3} - \frac{\sigma_1^2 r}{2} + \frac{r^3}{24}\right) \qquad (1.9.15)$$

As in (1.9.10) we must account for the permutations. Since the integrand's value can come from (-1*h*h) or (h*h*-1) or (h*-1*h), we must multiply the integral by 3. We also include the value of the integrand (-h^2) and the coefficient in front of the integral (1.9.7) (-1/3). Integrating (1.9.15) for all possible positions of sphere 2 and including the coefficients:

$$I_3 = h^2 \int V d\mathbf{r_2} = 4\pi h^2 \int_0^{\sigma_1} V r^2 dr \qquad (1.9.16)$$

For a description of the solution to (1.9.16), see appendix 1. The result of the integral in (1.9.16) is:

$$I_3 = -\frac{b_0^2}{8} h^2 \left[-32\lambda^3 + 18\lambda^2 + 48\right] \qquad \lambda>2 \qquad (1.9.17)$$

Now we examine (-1*h*h) for λ<2.

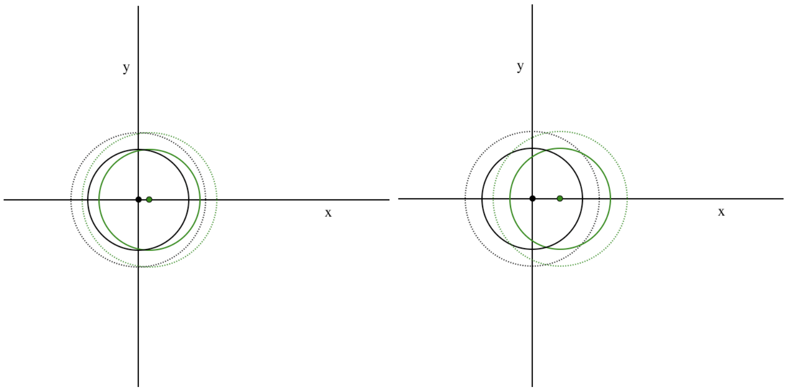

Figure 1.9 - Cross section of two overlapping square-well potentials within the hard-core radius for λ<2.

From figure 1.9 we can see that the solution for λ>2 will not work for λ<2 because the volume of the inner spheres is not completely contained within the overlap of the outer shells when the distance increases beyond the $\sigma_2 - \sigma_1$.

Instead, we choose the $f_{1,2}$-bond to have the value h.

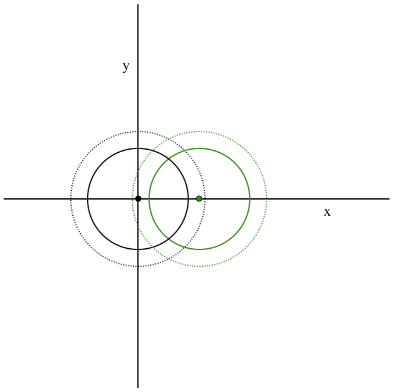

Figure 1.10 - Cross section of two overlapping square-well potentials outside the hard-core radius for λ<2.

The center of the third sphere must be placed in the inner sphere of one sphere and inside the outer shell of the other. The volume available to sphere 3 is the volume of overlap of spheres with radii σ_2 and σ_1 minus the overlap of two spheres of radius σ_1.

$$V = V_{1,2} - V_{1,1} \tag{1.9.18}$$

We now need an expression for the volume of two overlapping sphere with different radii. First we find an expression for the volume of a sphere cap as a function of its height.

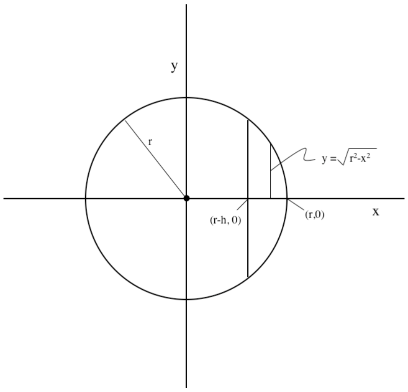

Figure 1.11 - Cross section of a sphere cap.

From (1.9.4):

$$V = \pi \int_{r-h}^{r} \left(\sqrt{r^2 - x^2}\right)^2 dx = \pi \left[r^2 x - \frac{x^3}{3}\right]_{r-h}^{r} = \pi \left[r^3 - \frac{r^3}{3} - r^2(r-h) + \frac{(r-h)^3}{3}\right]$$

$$= \frac{\pi}{3}\left[2r^3 - 3r^3 + 3r^2 h + r^3 - 3r^2 h + 3rh^2 - h^3\right] = \frac{\pi h^2}{3}(3r - h) \tag{1.9.19}$$

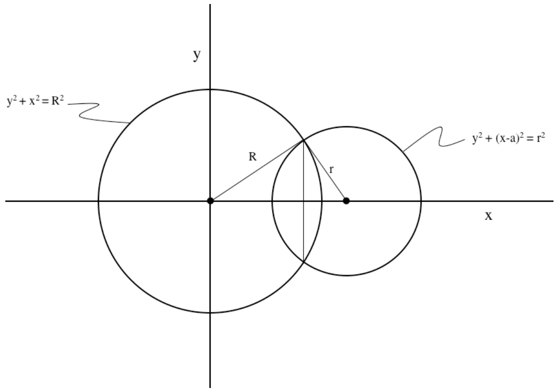

Figure 1.12 - Cross section of two overlapping spheres with different radii.

We can see that the volume of overlap is the sum of the two sphere caps. We need the value of x at the plane that divides the two caps.

$$y^2 + x^2 = R^2 \tag{1.9.20}$$

$$y^2 + (x-a)^2 = r^2 \tag{1.9.21}$$

$$y^2 = R^2 - x^2 = r^2 - x^2 + 2xa - a^2 \tag{1.9.22}$$

$$x = \frac{R^2 - r^2 + a^2}{2a} \tag{1.9.23}$$

The height of the right cap (h_R) and the left cap (h_r) are:

$$h_R = R - \frac{R^2 - r^2 + a^2}{2a} = \frac{(-R + r + a)(R + r - a)}{2a} \tag{1.9.24}$$

$$h_r = \frac{R^2 - r^2 + a^2}{2a} - (a - r) = \frac{(R - r + a)(R + r - a)}{2a} \tag{1.9.25}$$

And substituting (1.9.24) and (1.9.25) into (1.9.19):

$$V_{r,R} = \frac{\pi\,(R + r - a)^2\,(a^2 + 2ar + 2aR + 6rR - 3r^2 - 3R^2)}{12a} \tag{1.9.26}$$

Using (1.9.26) and (1.9.6) in (1.9.18) we can calculate the volume available for the center of sphere 3 (here, again r is the distance that separates sphere 1 and sphere 2):

$$V = \frac{\pi\,(\sigma_2 + \sigma_1 - r)^2\,(r^2 + 2r\sigma_1 + 2r\sigma_2 + 6\sigma_1\sigma_2 - 3\sigma_1^2 - 3\sigma_2^2)}{12r} - 2\pi\left(\frac{2\sigma_1^3}{3} - \frac{\sigma_1^2 r}{2} + \frac{r^3}{24}\right) \tag{1.9.27}$$

Again we need to multiply by 3 since we assumed the $f_{2,3}$-bond was –1. We also need to multiply by the value of the integrand ($-h^2$) and the coefficient of the integral in (1.9.7) (-1/3), giving us I_3 in the same form as (1.9.16), but now using (1.9.27) as the volume. Solving (1.9.16) with (1.9.27) we have (for a detailed solution see appendix 1):

$$I_3 = -\frac{b_0^2}{8}h^2\left[2\lambda^6 - 36\lambda^4 + 32\lambda^3 + 18\lambda^2 - 16\right] \qquad \lambda<2 \qquad (1.9.28)$$

Finally, we evaluate the portion of the C(T) integral where the integrand takes the value (h*h*h) and label its contribution I_4. The center of sphere 2 must lie within the outer shell of sphere 1, and the center of sphere 3 lies within the outer shells of both 1 and 2. There is no permutation factor to include in this integration. Again it is necessary to calculate $\lambda<2$ and $\lambda>2$ separately.

For $\lambda>2$ we have to break the integral into three parts. First is the region where the two smaller spheres of 1 and 2 are completely inside the overlapping volume of the outer shells. The second region is where some of the inner sphere of 1 lies outside the outer shell of 2 and vice versa, and the inner spheres still overlap. In third region the inner spheres do not overlap.

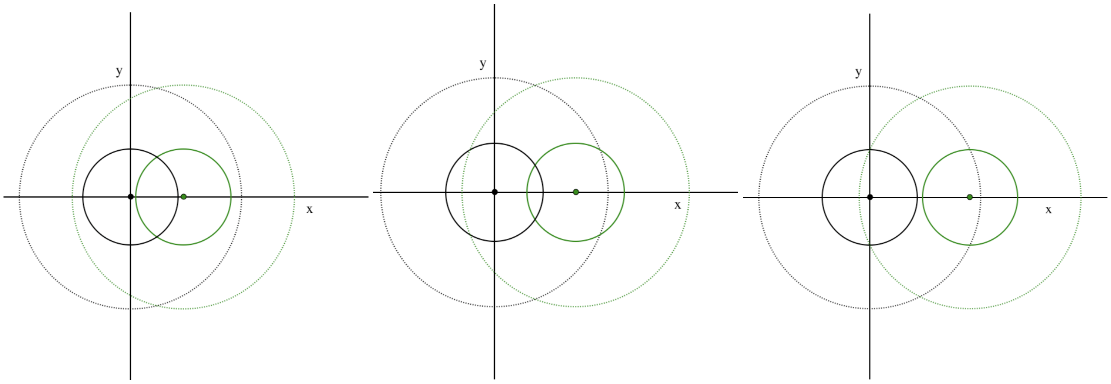

Figure 1.13 - Cross section of two overlapping square-well potentials outside the hard-core radius for $\lambda>2$ at increasing distances.

The first case, where the smaller spheres are completely surrounded, is in the range $\sigma_1 \le r \le \sigma_2 - \sigma_1$. The volume in this region can be calculated by (1.9.14).

The second region is in the range $\sigma_2 - \sigma_1 \le r \le 2\sigma_1$. The volume in the second region can be calculated from the volume of overlap of the two outside spheres ($V_{2,2}$) subtracting out the contribution of each of the outer sphere/inner sphere overlap ($2V_{1,2}$) and adding back in the volume that was subtracted twice ($V_{1,1}$):

$$V = V_{2,2} - 2V_{1,2} + V_{1,1} \tag{1.9.29}$$

The third region is in the range $2\sigma_1 \le r \le \sigma_2$. In this region there is no overlap between the inner spheres, and hence no volume subtracted twice, so we can set $V_{1,1}$ equal to zero and use the volume given by (1.9.29).

$$V = V_{2,2} - 2V_{1,2} \tag{1.9.30}$$

Since there are no permutations, we only need to multiply the integral by the value of the integrand (h^3) and the coefficient of the integral from (1.9.7):

$$I_4 = -\frac{4\pi h^3}{3}\left[\int_{\sigma_1}^{\sigma_2-\sigma_1} V_a r^2 dr + \int_{\sigma_2-\sigma_1}^{2\sigma_1} V_b r^2 dr \int_{2\sigma_1}^{\sigma_2} V_c r^2 dr\right] \tag{1.9.31}$$

where V_a is the volume in (1.9.14), V_b is the volume in (1.9.29) and V_c is the volume in (1.9.30). The solution to (1.9.31) is (for the detailed solution see appendix 1):

$$I_4 = -\frac{b_0^2}{8}h^3\left[5\lambda^6 - 32\lambda^3 + 18\lambda^2 + 26\right] \qquad \lambda>2 \tag{1.9.32}$$

It should be noted that for the case $\lambda>3$: $2\sigma_1 < \sigma_2 - \sigma_1$, which means that the inner spheres stop overlapping before they have some of their volume outside the bounds of the outer sphere. This changes the ranges of regions 1, 2 and 3 to $\sigma_1 < r_a < 2\sigma_1 < r_b < \sigma_2 - \sigma_1 < r_c < \sigma_2$. V_a and V_c are unchanged, but V_b becomes:

$$V_b = V_{2,2} - 2V_1 \tag{1.9.33}$$

Despite the change to V_b and the ranges integrated over, the solution to $\lambda>3$ simplifies to (1.9.32) (see appendix 1 for more detail).

Lastly, we must evaluate I_4 for $\lambda<2$.

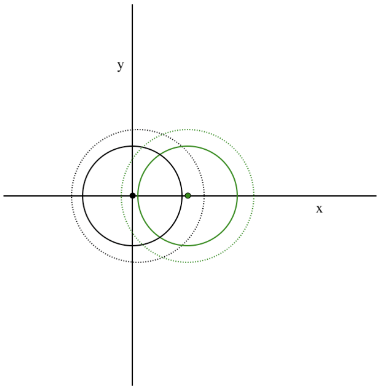

Figure 1.14 - Cross section of two overlapping square-well potentials outside the hard-core radius for λ<2.

For all $\sigma_1 < r < \sigma_2$, the inner spheres overlap and are never completely inside of the overlap of the outer spheres. The volume available to the center of the third sphere is, therefore, always described by (1.9.29). As with λ>2, there are no other permutations so the only coefficients for I_4 are from the value of the integrand (h^3) and (1.9.4) (-1/3), making I_4:

$$I_4 = -\frac{4\pi h^3}{3} \int_{\sigma_1}^{\sigma_2} \left[V_{2,2} - 2V_{1,2} + V_{1,1} \right] r^2 \ dr \tag{1.9.34}$$

Integrating (1.9.34) (for more detail see appendix 1):

$$I_4 = -\frac{b_0^2}{8} h^3 \left[6\lambda^6 - 18\lambda^4 + 18\lambda^2 - 6 \right] \qquad \lambda<2 \tag{1.9.35}$$

Having solved (1.9.7) for all non-zero values of the integrand, we can now calculate $C_{SW}(T)$:

$$C_{SW}(T) = I_1 + I_2 + I_3 + I_4 \tag{1.9.36}$$

For λ<2 $C_{SW}(T)$ is the sum of (1.9.9), (1.9.13), (1.9.28) and (1.9.35):

$$\begin{aligned} C_{SW}(T) = -\frac{b_0^2}{8} \{ & -5 \\ & +h \left[\lambda^6 - 18\lambda^4 + 32\lambda^3 - 15 \right] \\ & +h^2 \left[2\lambda^6 - 36\lambda^4 + 32\lambda^3 + 18\lambda^2 - 16 \right] \\ & +h^3 \left[6\lambda^6 - 18\lambda^4 + 18\lambda^2 - 6 \right] \\ & \} \qquad \lambda < 2 \end{aligned} \tag{1.9.37}$$

For λ>2 $C_{SW}(T)$ is the sum of (1.9.9), (1.9.12), (1.9.17) and (1.9.32):

$$C_{SW}(T) = -\frac{b_0^2}{8}\left\{-5 + 17h + h^2\left[-32\lambda^3 + 18\lambda^2 + 48\right]\right.$$
$$\left. + h^3\left[5\lambda^6 - 32\lambda^3 + 18\lambda^2 + 26\right]\ \right\} \qquad (1.9.38)$$

Note that (1.9.37) and (1.9.38) match Hauge's[2] result from Fourier transform (1.8.32). The calculation of virial coefficients through the analysis of overlapping spheres is more intuitive and direct than the Fourier transform, despite the condensed derivation of the later. It also has implications for higher order virial coefficients that the Fourier transform cannot describe.

1.10 FOURTH VIRIAL COEFFICIENT

The fourth virial coefficient is the sum of three cluster diagrams.

$\beta_3(\mathrm{T}) = \frac{1}{\mathrm{V}}$ [

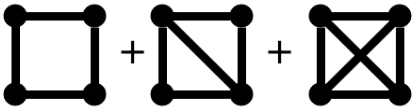

] (1.10.1)

Remembering that each cluster diagram has implicit in it a coefficient equal to the number of ways it may be relabeled without changing the connectivity. For the first cluster in (1.10.1) this coefficient is (1/8):

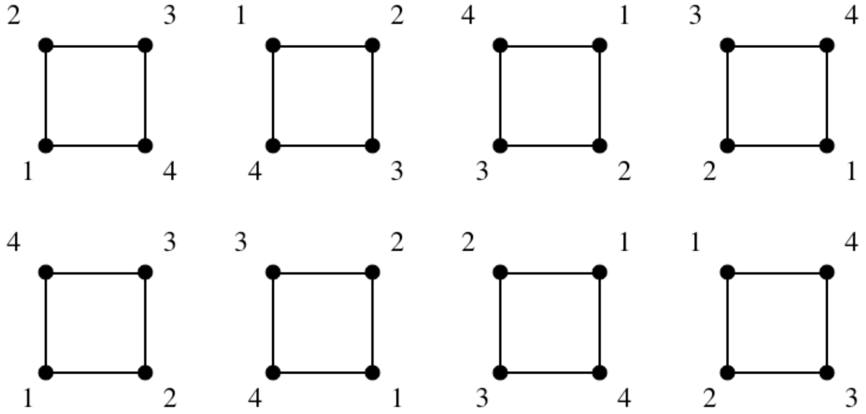

Figure 1.15 – Labeling possibilities for D_1.

For the second cluster in (1.10.1) the coefficient is (1/4)

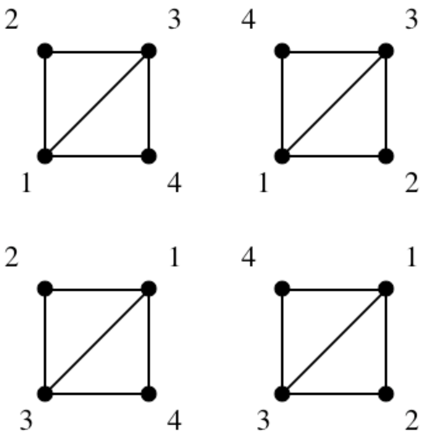

Figure 1.16 - Labeling possibilities for D_2.

For the third cluster in (1.10.1) the coefficient is (1/24):

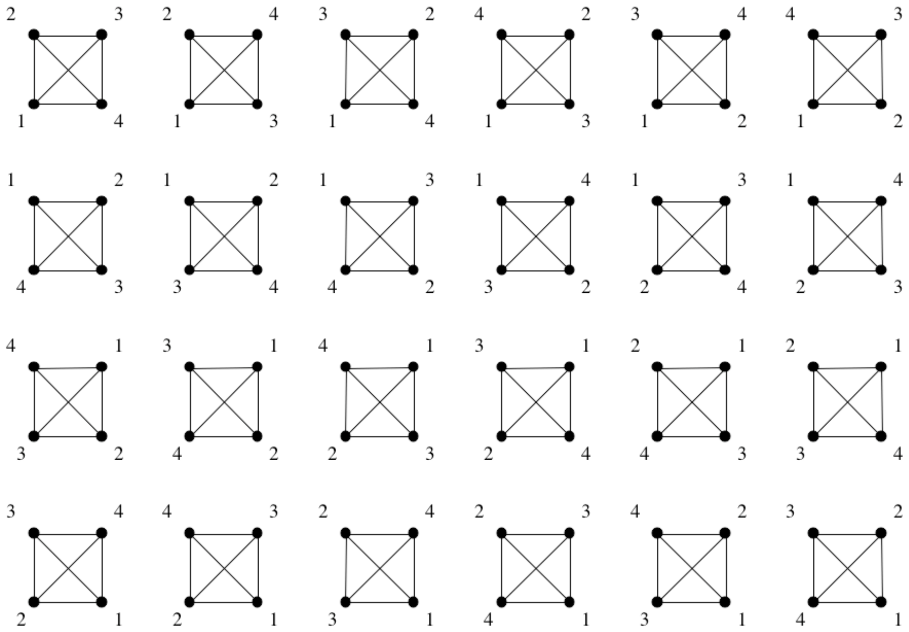

Figure 1.17 - Labeling possibilities for D_3.

As with (1.4.16) the term V^{-1} can be omitted by fixing the position of the first particle to the origin, giving β_3 as:

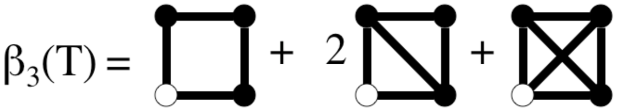

(1.10.2)

For the first and last cluster in (1.10.1) all particles are identical, but in the second integral there are particles with 3 bonds and particles with 2 bonds. We therefore need to perform the integral with both choices for the fixed particle, however in the absence of an external potential the integrals will be equal, and we may simply double the result.

Then from (1.4.25):

$$D(T) = -\frac{3}{4}\beta_3 \tag{1.10.3}$$

By labeling the integrals in (1.10.1) in order as D_1, D_2 and D_3; D(T) can be expressed as:

$$D(T) = D_1 + D_2 + D_3 \tag{1.10.4}$$

The coefficients implicit in (1.10.2) have been reduced by from those in (1.10.1) by fixing the first particle. The coefficient in the first integral (D_1) is now (1/2):

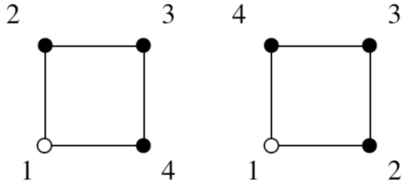

Figure 1.18 - Labeling possibilities for D_1 with particle 1 fixed.

and when combined with (1.10.3) makes D_1:

$$D_1 = -\frac{3}{8}\int\int\int f_{1,2}f_{2,3}f_{3,4}f_{1,4}d\mathbf{r_2}d\mathbf{r_3}d\mathbf{r_4} \tag{1.10.5}$$

The coefficient in the second diagram from (1.10.2) is (1/2):

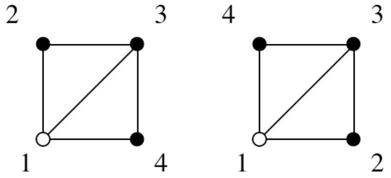

Figure 1.19 - Labeling possibilities for D_2 with particle 1 fixed.

When the coefficient in front of the second diagram in (1.10.2) (2) the factor of 1/2 implicit in the diagram, and the coefficient of (-3/4) from (1.10.3) are combined D_2 is:

$$D_2 = -\frac{3}{4}\int\int\int f_{1,2}f_{2,3}f_{3,4}f_{1,4}f_{1,3}d\mathbf{r_2}d\mathbf{r_3}d\mathbf{r_4} \tag{1.10.6}$$

The coefficient in the final diagram in (1.10.2) is (1/6):

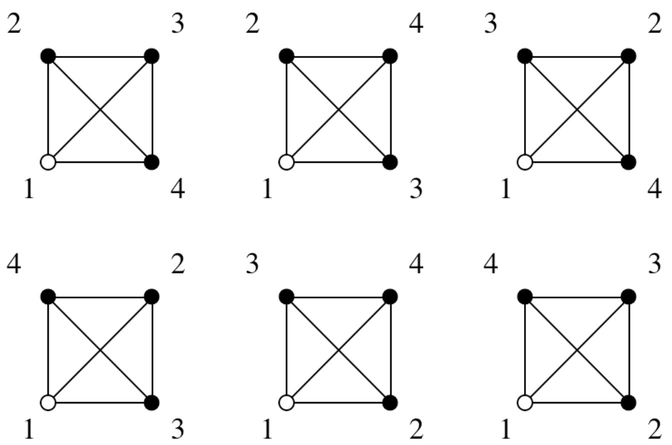

Figure 1.20 - Labeling possibilities for D_3 with particle 1 fixed.

and when combined with (1.10.3) gives:

$$D_3 = -\frac{1}{8}\int\int\int f_{1,2}f_{2,3}f_{3,4}f_{1,4}f_{1,3}f_{2,4}d\mathbf{r_2}d\mathbf{r_3}d\mathbf{r_4} \tag{1.10.7}$$

The fourth virial coefficient was solved for the hard-sphere potential by Boltzmann[3]:

$$\frac{D(T)}{b_0^3} = \frac{2707}{4480} + \frac{219\sqrt{2}}{2240\pi} - \frac{4131}{4480}\frac{arccos(\frac{1}{3})}{\pi} \tag{1.10.8}$$

The fourth virial coefficient has not been completely solved for the square-well potential.

1.11 FOURTH VIRIAL COEFFICIENT D_1

The first integral in the fourth virial coefficient is D_1 (1.10.5). D_1 was solved for the square-potential by Barker and Monaghan[4]:

$$\frac{D_1(T)}{b_0^3} = -\frac{1}{560}\left[544\lambda^9h^4 - h^3(1+h)\zeta_1 + 24h^2(1+h)^2\zeta_2 - h(1+h)^3\zeta_3 + 544(1+h)^4\right] \tag{1.11.1}$$

With ζ_1, ζ_2, and ζ_3 defined as:

$$\zeta_1 = 3150\lambda^6 - 1134\lambda^4 + 162\lambda^2 - 2 \tag{1.11.2}$$

$$\zeta_2 = 420\lambda^3 - 324\lambda^2 + 40 \tag{1.11.3}$$

$$\zeta_3 = \begin{cases} \begin{array}{l} \lambda^9 - 81\lambda^7 + 315\lambda^6 + 567\lambda^5 - 5103\lambda^4 \\ \qquad +8505\lambda^3 - 2187\lambda^2 + 159, \end{array} & 2 \le \lambda \le 3 \\ \qquad 6720, & \lambda \ge 2 \end{cases}$$

(1.11.4)

Or, with D_1 in the same form as (1.9.37) and (1.9.38):

$$\begin{aligned} D_1(T) = -\frac{b_0^3}{560}\Big\{ \; & 544 + h\left[-\lambda^9 + 81\lambda^7 - 315\lambda^6 - 567\lambda^5 + 5103\lambda^4 - 8505\lambda^3 + 2187\lambda^2 + 2017\right] \\ & +h^2\left[-3\lambda^9 + 243\lambda^7 - 945\lambda^6 - 1701\lambda^5 + 15309\lambda^4 - 15435\lambda^3 - 1215\lambda^2 + 3747\right] \\ & +h^3\left[-3\lambda^9 + 243\lambda^7 - 4095\lambda^6 - 1701\lambda^5 + 16443\lambda^4 - 5355\lambda^3 - 9153\lambda^2 + 3621\right] \\ & +h^4\left[543\lambda^9 + 81\lambda^7 - 3465\lambda^6 - 567\lambda^5 + 6237\lambda^4 + 1575\lambda^3 - 5751\lambda^2 + 1347\right] \Big\} \end{aligned}$$

(1.11.5)

Barker and Monaghan present this as a solution for 2 ≤ λ ≤ 3, but Hauge[5] has shown that it applies to all possible well widths (λ ≥ 1).

There are three important features that must exist in all solutions to the cluster integrals for the square-well potential. First, if h is set to –1 then the solution should give the value for a hard sphere with the core radius equal to λσ. The f-bond inside of a hard sphere's radius is –1, so by setting h to –1 we are simply extending the hard-core radius to the well width.

For example, the solution to D_1 for a hard sphere is:

$$D_1(T) = -544\frac{b_0^3}{560} = -\frac{8\pi^3\sigma^9}{27}\frac{544}{560} \qquad (1.11.6)$$

and for h=-1 (1.11.5) gives:

$$\begin{aligned} D_1(T) = -\frac{b_0^3}{560}\Big\{ \; & 544 - \left[-\lambda^9 + 81\lambda^7 - 315\lambda^6 - 567\lambda^5 + 5103\lambda^4 - 8505\lambda^3 + 2187\lambda^2 + 2017\right] \\ & + \left[-3\lambda^9 + 243\lambda^7 - 945\lambda^6 - 1701\lambda^5 + 15309\lambda^4 - 15435\lambda^3 - 1215\lambda^2 + 3747\right] \\ & - \left[-3\lambda^9 + 243\lambda^7 - 4095\lambda^6 - 1701\lambda^5 + 16443\lambda^4 - 5355\lambda^3 - 9153\lambda^2 + 3621\right] \\ & + \left[543\lambda^9 + 81\lambda^7 - 3465\lambda^6 - 567\lambda^5 + 6237\lambda^4 + 1575\lambda^3 - 5751\lambda^2 + 1347\right] \Big\} \end{aligned}$$

(1.11.7)

All of the terms in (1.11.7) cancel except those with a factor of λ^9, leaving:

$$D_1(T) = -\frac{b_0^3}{560}\left\{544\lambda^9\right\} = -\frac{8\pi^3\sigma^9\lambda^9}{27}\frac{544}{560} \qquad (1.11.8)$$

Clearly (1.11.8) is the value for (1.11.6) when σ → λσ.

The second feature of the solutions of cluster diagrams for the square-well potential is that they give the solution for a hard sphere potential when λ is set to 1. This is equivalent to having an infinitely thin well, or no well at all. For λ = 1, (1.11.5) becomes:

$$\begin{aligned} D_1(T) = -\frac{b_0^3}{560}\{544 + h\,[-1 + 81 - 315 - 567 + 5103 - 8505 + 2187 + 2017] \\ +h^2\,[-3 + 243 - 945 - 1701 + 15309 - 15435 - 1215 + 3747] \\ +h^3\,[-3 + 243 - 4095 - 1701 + 16443 - 5355 - 9153 + 3621] \\ +h^4\,[543 + 81 - 3465 - 567 + 6237 + 1575 - 5751 + 1347]\quad\} \end{aligned} \tag{1.11.9}$$

All the terms in each h^n grouping cancel, leaving only:

$$D_1(T) = -\frac{b_0^3}{560}544 \tag{1.11.10}$$

again leaving the value for a hard sphere.

The third common feature to all square-well cluster integrals is that for h=0 the integral again gives the value for the hard sphere. Here we are setting the interaction potential inside the well equal to the interaction at large distances (zero). It is obvious that when h=0 (1.11.5) gives (1.11.6).

These three features are present in all solutions to square-well virial cluster diagrams presented so far (1.7.15), (1.8.32), (1.9.37) and (1.9.38). These features are valuable methods for testing the accuracy of a solution to one of the cluster diagrams.

For example in the same paper Barker and Monaghan[4] presented their solution to D_1 they also presented solutions to D_2 and D_3. The solution for D_3, fails all three testes, although it should be noted that the authors only claim accuracy within 1% of the real solution for D_3.

1.12 FOURTH VIRIAL COEFFICIENT D_2

Barker and Monaghan[4] also presented results for D_2 when λ ≥ 2.

$$\frac{D_2(T)}{b_0^3} = -\frac{3}{4}\left[-\frac{6347}{3360}(1+h)^5 + \frac{1847}{105}h(1+h)^4 - \frac{\xi_1(\lambda)}{5040}h^2(1+h)^3 + \frac{\xi_2(\lambda)}{17640}h^3(1+h)^2 - \frac{\xi_3(\lambda)}{181440}h^4(1+h) + \frac{6347}{3360}\lambda^9 h^9\right]$$

(1.12.1)

where:

$$\xi_1(\lambda) = \begin{cases} 24\lambda^9 - 1944\lambda^7 + 7560\lambda^6 + 13608\lambda^5 - 122472\lambda^4 \\ \qquad +241920\lambda^3 - 72252\lambda^2 + 166101, & 2 \le \lambda \le 3 \\ 37800\lambda^3 - 19764\lambda^2 + 323565, & \lambda \ge 3 \end{cases} \tag{1.12.2}$$

$$\xi_2(\lambda) = 1411200\lambda^3 - 1070496\lambda^2 + 59535\lambda + 89040 \tag{1.12.3}$$

$$\xi_3(\lambda) = 4173120\lambda^6 - 2653560\lambda^5 + 181440\lambda^3 + 11664\lambda^2 + 1026 \tag{1.12.4}$$

note that in [4] the first fraction in (1.12.1) is incorrectly given as (6437/3360).

Or, with D_2 in the same form as (1.9.37), (1.9.38) and (1.11.5):

$$\begin{aligned} D_2(T) = -\frac{b_0^3}{4480}\{&-6347 + 27369h \\ &+h^2[-16\lambda^9 + 1296\lambda^7 - 5040\lambda^6 - 9072\lambda^5 + 81648\lambda^4 \\ &\qquad -161280\lambda^3 + 48168\lambda^2 + 62212] \\ &+h^3[-48\lambda^9 + 3888\lambda^7 - 15120\lambda^6 - 27216\lambda^5 + 244944\lambda^4 \\ &\qquad -215040\lambda^3 - 59400\lambda^2 + 11340\lambda - 24088] \\ &+h^4[-48\lambda^9 + 3888\lambda^7 - 92400\lambda^6 + 21924\lambda^5 + 244944\lambda^4 \\ &\qquad +50400\lambda^3 - 263520\lambda^2 + 22680\lambda - 93620] \\ &+h^5[6331\lambda^9 + 1296\lambda^7 - 82320\lambda^6 + 40068\lambda^5 + 81648\lambda^4 \\ &\qquad +104160\lambda^3 - 155952\lambda^2 + 11340\lambda - 41036] \ \} \end{aligned} \tag{1.12.5}$$

The second cluster integral contributing to the fourth virial coefficient for a square-well potential, defined in (1.10.6), was solved for all well widths by Hauge[5] using a Fourier transform in a similar manner to his solution for the third virial coefficient. His result confirmed the D_2 presented by Barker and Monaghan for λ ≥ 2. Hauge's D_2 for λ ≤ 2:

$$\begin{aligned} D_2(T) = -\frac{b_0^2}{4480}\{&-6347 \\ &+h\left[51\lambda^9 - 2376\lambda^7 + 6720\lambda^6 + 18144\lambda^5 - 103572\lambda^4 + 134400\lambda^3 - 23328\lambda^2 - 30039\right] \\ &+h^2\left[1964\lambda^9 - 11340\lambda^8 + 9504\lambda^7 + 23520\lambda^6 + 76356\lambda^5 - 356832\lambda^4 \right. \\ &\qquad \left. +253680\lambda^3 + 74952\lambda^2 - 71804\right] \end{aligned}$$

$$
\begin{aligned}
&+h^3\left[8768^9-34020\lambda^8-19224\lambda^7+149520\lambda^6+117180\lambda^5-470988\lambda^4\right.\\
&\qquad\qquad\qquad\qquad\left.+62160\lambda^3+265464\lambda^2+11340\lambda-90200\right]\\
&+h^4\left[11848\lambda^9-34020\lambda^8-76464\lambda^7+178080\lambda^6+127008\lambda^5-285768\lambda^4\right.\\
&\qquad\qquad\qquad\qquad\left.-102480\lambda^3+212544\lambda^2+22680\lambda-53428\right]\\
&+h^5\left[11340\lambda^9-11340\lambda^8-45360\lambda^7+45360\lambda^6+68040\lambda^5-68040\lambda^4\right.\\
&\qquad\qquad\qquad\qquad\left.-45360\lambda^3+45360\lambda^2+11340\lambda-11340\right]\quad\Big\}
\end{aligned}
\tag{1.12.6}
$$

Equations (1.12.5) and (1.12.6) passes the three tests for a square-well virial coefficient. If h is –1, both give the solution for a hard sphere with a hard-core radius of λσ; if λ is 1, both give the solution for a hard sphere; and if h is 0, both equations give the solution for a hard sphere. All coefficients in each h grouping cancel each other when λ is 1, and each set of coefficients grouped by powers of λ cancel when h is –1 with the exception of λ^9 which gives $-6347\lambda^9$.

There are a few other features common to all square-well virial solutions. They are always be expressible in 3*(i+1)-order polynomials times powers of h up to the number of f-bonds in the integral, where i is the same i in(1.4.18) (λ^3 for B(T), λ^6 for C(T), λ^9 for D(T) etc.) . Each polynomial can be factored and contains the term $(\lambda -1)^n$, where n is the power of h the polynomial corresponds to. For example, h^4 in D_1 from Barker and Monaghan (1.11.5):

$$
\begin{aligned}
&543\lambda^9+81\lambda^7-3465\lambda^6-567\lambda^5+6237\lambda^4+1575\lambda^3-5751\lambda^2+1347\\
&\qquad=3(181\lambda^5+724\lambda^4+1837\lambda^3+2573\lambda^2+1796\lambda+449)(\lambda-1)^4
\end{aligned}
\tag{1.12.7}
$$

Or from h^5 for D2 (1.12.6):

$$
\begin{aligned}
&11340\lambda^9-11340\lambda^8-45360\lambda^7+45360\lambda^6+68040\lambda^5-68040\lambda^4\\
&\qquad-45360\lambda^3+45360\lambda^2+11340\lambda-11340\\
&\qquad\qquad\qquad\qquad\qquad=11340(\lambda+1)^4(\lambda-1)^5
\end{aligned}
\tag{1.12.8}
$$

Just like equations (1.9.37) and (1.9.38) in the case of the third virial coefficient, equations (1.12.5) and (1.12.6) give the same result for λ = 2.

$$
D_2(T)=-\frac{b_0^3}{4480}\left[-6347+27369h-184156h^2+594272h^3-1518980h^4+918540h^5\right]
$$

(1.12.9)

This result is in agreement with the result of Katsura's[6] evaluation of square-wells with equal well widths.

1.13 FOURTH VIRIAL COEFFICIENT D_3

There has not been an analytical solution to the third cluster integral in the fourth virial coefficient for the square-well potential. This can be attributed to the high connectivity of the diagram (known as the complete star):

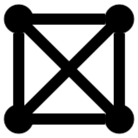

There have been several attempts to calculate D_3 using various methods, most relying on computer simulation or calculation. These methods and their results will be discussed in detail later in this work.

For the hard sphere potential D3 has been solved by Boltzmann[3]:

$$\frac{D_3(T)}{b_0^3} = \frac{712}{4480} + \frac{219\sqrt{2}}{2240\pi} - \frac{4131}{4480}\frac{arccos\left(\frac{1}{3}\right)}{\pi} \tag{1.12.4}$$

Chapter 1 References

[1] Boltzmann L 1899 *Proc. Sect. Sci. K. Acad. Wet., Amsterdam* **7** 484

[2] Hauge E. H. 1965 PhD Thesis Trondheim, Norway

[3] Boltzmann 4th Virial for Hard Spheres

[4] Barker, J. A., and Monaghan, J. J., 1962, *J. Chem. Phys.*, **36**, 2558.

[5] Hauge, E. H., 1963, *J. Chem. Phys.*, **39**, 389.

[6] Katsura, S., 1958, *Phys. Rev.*, **115**, 1417.

Chapter 2
Ratio Integration

2.1 HIGHER ORDER VIRIAL APPROXIMATIONS

Although there have been no analytical solutions to cluster integrals above D_2 for the square-well potential, various techniques have been employed to approximate their values.

Katsura[1] used the Fourier transform on the cluster integrals of the fourth virial coefficient for the square-well potential and broke the problem down with use of the addition theorem of Bessel functions. Then he integrated numerically (by computer) for $\lambda = 2$. Katsura's result became the standard more generalized approximations were measured against.

As mentioned in 1.11, Barker and Monaghan[2] derived the solution for D_1. Their solution hinged on the simplification of the integrals for well widths greater than the hard-core radius ($\lambda \geq 2$). For any triangle, the sum of the length of any two sides must be greater than the remaining side. So for $\lambda \geq 2$, if two f-bonds are within the hard-core, the third must be non-zero. Their solution was found by rearranging the cluster integrals and substituting in step functions of the form:

$$H(f_{1,2}) = \begin{cases} 0, f_{1,2} = 0 \\ 1, f_{1,2} \neq 0 \end{cases} \tag{2.1.1}$$

Although their solution to D_1 was appropriate for all well widths, their solution for D_2 could not be generalized for $\lambda < 2$, and D_3 was integrated using a Monte Carlo technique.

Ree and Hoover[3] were able to simplify the general cluster integrals, and reduce the number of integrals for each virial coefficient regardless of pair potential. The method involved the integration over e-bonds and f-bonds. For example, if we look at an integral for 4 particles with 4 f-bonds and 2 e-bonds:

$$\int\int\int f_{1,2}f_{2,3}f_{3,4}f_{1,4}e_{1,3}e_{2,4}d\mathbf{r_2}d\mathbf{r_3}d\mathbf{r_4} \tag{2.1.2}$$

Represented graphically, with f-bonds represented by a solid line and e-bonds by a dashed line:

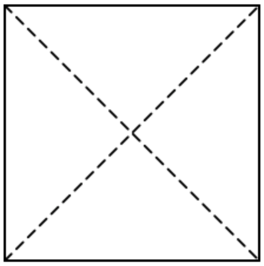

Figure 2.1 – Ree-Hoover diagram for D(T).

This representation is known as a Ree-Hoover diagram. A Ree-Hoover diagram does not contain the black circles that were in the graphical representation of the cluster diagrams. It also does not have any implicit coefficients in it arising from symmetry. It also represents the integrand and not the actual integral (this is a minor detail since integrals and integrands are both commutative and will not be mentioned again).

Substituting $e_{i,j} = f_{i,j} + 1$ into (2.1.2):

$$\int\int\int f_{1,2}f_{2,3}f_{3,4}f_{1,4}(f_{1,3}+1)(f_{2,4}+1)d\mathbf{r_2}d\mathbf{r_3}d\mathbf{r_4}$$

$$= \int\int\int f_{1,2}f_{2,3}f_{3,4}f_{1,4}(f_{1,3}f_{2,4}+f_{1,3}+f_{2,4}+1)d\mathbf{r_2}d\mathbf{r_3}d\mathbf{r_4}$$

$$= \int\int\int f_{1,2}f_{2,3}f_{3,4}f_{1,4}f_{1,3}f_{2,4}d\mathbf{r_2}d\mathbf{r_3}d\mathbf{r_4} + \int\int\int f_{1,2}f_{2,3}f_{3,4}f_{1,4}f_{1,3}d\mathbf{r_2}d\mathbf{r_3}d\mathbf{r_4} + \int\int\int f_{1,2}f_{2,3}f_{3,4}f_{1,4}f_{2,4} + \int\int\int f_{1,2}f_{2,3}f_{3,4}f_{1,4}d\mathbf{r_2}d\mathbf{r_3}d\mathbf{r_4} \tag{2.1.3}$$

or in graphical form:

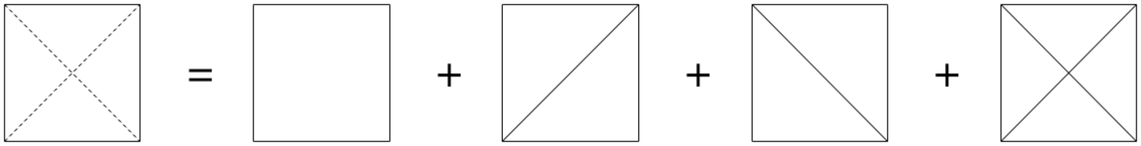

Figure 2.2 – Equivalent cluster diagrams for a Ree-Hoover diagram.

In figure 2.2 the second and third diagrams on the right hand side have the same value and can be represented by the second with a coefficient of 2. The fourth virial coefficient represented in a Ree-Hoover diagram is:

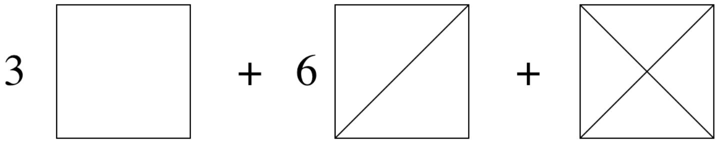

Figure 2.3 – D(T) as cluster diagrams.

which is equivalent to:

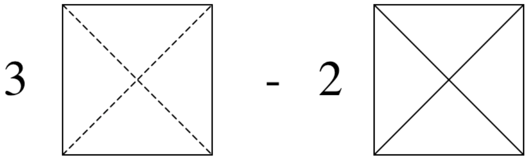

Figure 2.4 – D(T) as Ree-Hoover diagrams.

For the fourth virial coefficient Ree and Hoover reduced the number of integrals that need to be solved from three to two. Although not remarkably helpful for the fourth virial coefficient, this technique reduces the number of integrals significantly for higher ordered virial coefficients (from 10 to 5 for the fifth virial coefficient and from 56 to 23). The fifth virial goes from:

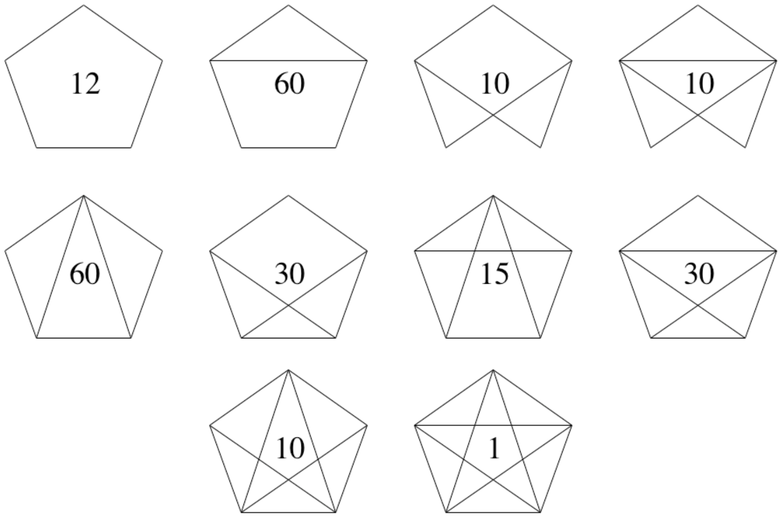

Figure 2.5 – E(T) as cluster diagrams.

(with the coefficients inside the diagrams) to:

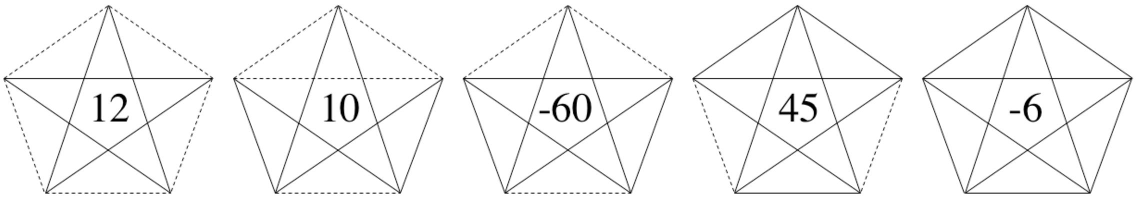

Figure 2.6 – D(T) as Ree-Hoover diagrams.

Masters[4] used the simplified Ree-Hoover diagram equations to evaluate the fourth and fifth virial coefficients for the square-well potential. Particles positions are randomly chosen (in a computer simulation) through a Monte Carlo process. Notice that each diagram in figure 2.6 has the same 5 f-bonds. We can label the particles 1 through 5 in such a way that 1 is always connected to 2 through an f-bond, 2 to 3 and so on, no matter which diagram:

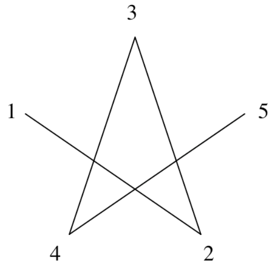

Figure 2.7 – The bonds common to all Ree-Hoover diagrams representing E(T).

Particles are randomly placed in this order, and are rejected if the corresponding f-bond it forms is zero ($r > \lambda\sigma$). After all particles are placed, the configuration is tested to see if it corresponds to any non-zero value of the 5 diagrams in Figure 2.6.

Unlike hard spheres, square-well particles can be separated at a distance where both an f-bond and an e-bond are non-zero, complicating this analysis. Each configuration can therefore correspond to more than one diagram. The assignment of diagrams is facilitated by the use of a look-up table. Look-up tables are also used for the weight and the unlabelling index of each diagram.

The result of the simulation is a matrix of coefficients that correspond to powers of e-bonds and f-bonds for distances within the square-well potential. For example, the result for the fifth virial coefficient is a 77 component matrix consisting of terms $C_{\alpha\beta}$, where:

$$E(T) = -\frac{4}{5!}\sum_{\alpha=0}^{10}\sum_{\beta=0}^{6} C_{\alpha\beta} h^{\alpha} h_1^{\beta} \tag{2.1.4}$$

In (2.1.4) h is still the value of an f-bond inside the well width, and h_1 is the value of an e-bond inside the well width.

Sevick and Monson[5] used Katsura's method of Fourier transform followed by numeric integration to calculate the fourth virial coefficient for square-wells with λ = 1.1, 1.5 and 2.0. Hussein and Ahmed[6] also used Katsura's method to calculate the third and fourth virial coefficients for λ = 2.0 in an arbitrary dimension. Both studies had results that agreed with Katsura's for λ = 2.0 in 3 dimensions.

Singh and Naresh[7] used Mayer Sampling, a technique developed by Singh and Kofke', to study the fourth, fifth and sixth virial coefficients for the square-well potential. Mayer sampling, which will be discussed in detail in chapter 4, is an importance sampling based on a free energy perturbation technique.

Particles, equal to the number of particles in the cluster integral to be calculated, are moved randomly, with the probability of each move determined by the value of the integrand before and after the move. After each attempted move, the value of the integrand for the square-well potential is stored as is the integrand for a reference potential (in this case the hard sphere potential). The solution to the reference cluster integral is then perturbed by the ratio of ensemble average of the integrand for square-well over the ensemble average of the integrand for the reference potential (normalized by the probability distribution):

$$\Gamma(T) = \Gamma_0(T)\frac{\langle \gamma/\pi \rangle}{\langle \gamma_0/\pi \rangle} \tag{2.1.5}$$

In (2.1.5) Γ(T) is the cluster integral, γ is the integrand and π is the probability distribution (usually the absolute value of γ), and the subscript 0 indicates a reference quantity.

All of these techniques have been valuable in extending our understanding of both the square-well potential and virial equation of state. However, each suffers from its own drawbacks and has inherent approximations.

2.2 RATIO INTEGRATION

From section 1.9 we know that the virial coefficients of hard spheres can be expressed as the volume available to overlapping spheres and that the virial coefficients of square-wells can be expressed as a sum of different powers of h from 0 to the number of bonds in the integrals, whose coefficients are functions of the well width.

The total volume of the integration for the square-well potential will be the same as for a hard sphere with a radius of $\lambda\sigma$. The virial coefficient for a square-well potential can be expressed as a function of the percentage of the volume for each of the possible values of the integrand, scaled by the volume of overlap in spheres of radius $\lambda\sigma$, as opposed to functions of the volume itself. For example from (1.9.38) the third virial coefficient for a square-well with λ = 2 is:

$$C(T) = -\frac{b_0^2}{8}\left[-5 + 17h - 136h^2 + 162h^3\right] \tag{2.2.1}$$

If we add the absolute value of all the coefficients inside of the brackets in (2.2.1) we have 320, which is the product of 5 (the value corresponding to the volume of overlap in a hard sphere potential) and 2^6 which is the factor the volume is expanded by for a square-well with a well width of 2. From (1.9.8) we know that for a hard sphere C(T) = $(5/8)b_0^2$. If we factor out the (-5) and (2^6) from (2.2.1) we are left with:

$$C(T) = 2^6 \frac{5}{8} b_0^2 \left[.015625 - .053125h + .425h^2 - .50625h^3\right] \tag{2.2.2}$$

In (2.2.2) the coefficients represent the percentage of the volume of overlap taken up by each integrand value. For example, with a well width of 2, 42.5% of the volume available for three spheres, with a radius of 2σ, to overlap is when two of the spheres are within a distance of σ and the third is at a distance from the first two greater than σ and inside of the 2σ radius imposed on it. This corresponds to an integrand value of $-h^2$ or (-1*h*h). The alternating signs in (2.2.2) are a result of the fact that when a non-zero f-bond doesn't equal h, it is –1.

Equation (2.2.2) demonstrates how a virial coefficient for the square-well potential can be expressed as a sum of volume percentages multiplied by the integrands they correspond to, times the value of the virial coefficient for a hard sphere potential with a radius of λσ.

The hard sphere potential is arguable the simplest pair potential and, as such, has been extensively studied. The available literature data on the virial coefficients of the hard sphere potential are exhaustive. The calculation of virial coefficients for the square-well potential can be simplified by taking advantage of the data already available for virial coefficients of the hard sphere. If the volume of overlap for the hard sphere is known, one only needs the percentage of volume the overlap spends in each value of the integrand, or alternatively put, what percentage of time it spends with each number of spheres at a distance from each other outside the hard-core. The problem is reduced from calculating the volume of the overlap for each integrand value to calculating the percent of the total volume. Many of the values of the hard sphere integrals are known exactly.

This can be accomplished with a simple Monte Carlo hit and miss algorithm. N Particles are randomly placed inside a box (where N is the number of particles in the cluster integral) and then the number of bonds with length σ to $\lambda\sigma$ are counted. This is how we determine the percentage of the volume with each value of h.

We shall first look at the simple case for the third virial coefficient (1.9.7). The first particle is fixed at the origin. The second particle is placed randomly in a cube surrounding the first with x, y and z each randomly chosen between -$\lambda\sigma$ to $\lambda\sigma$.

Two spherical particles require only one variable (distance) to describe their interaction, so we can choose the second particle to be on the positive x-axis (or from another point of view we can choose the x-axis to pass through the second particle). Care must be taken that the probability of finding the second particle at any point on the x-axis is equal to the probability of finding it at the same distance inside the cube. For example if we cannot simply take the position to be:

$$b_x = \lambda\sigma\ rand() \tag{2.2.3}$$

where b_x is the value of the x coordinate of the second (b) particle, and rand() is a function that produces a uniformly distributed random number between 0 and 1. If (2.2.3) were used b_x would be uniformly distributed on the x-axis between 0 and $\lambda\sigma$. However, in three dimensions there are more points available to b_x as distance increases (the probability of finding b_x at any distance should be proportional to the surface area of a sphere with that radius).

Instead we use:

$$b_x = \lambda\sigma\ \sqrt{rand()^2 + rand()^2 + rand()^2} \tag{2.2.4}$$

where, for each occurrence of rand() a different random number is generated. We are essentially placing b in a cube with dimensions x, y and z from 0 to $\lambda\sigma$ and then determining the distance from particle a (at the origin) and assigning that as the x value for b (y and z are zero). Although we do not allow b to have negative value, there is no error introduced because each octant is symmetrical.

By placing b on the x-axis rather than in a three dimensional box we can save computation time when determining its distance from other particles.

The distance between b and a is the value of b_x. If this distance is greater than $\lambda\sigma$ the integrand will be zero and we need to replace b. If the distance between a and b is less than $\lambda\sigma$ we can place the third particle (c).

The third particle must be placed randomly such that it is within a distance of $\lambda\sigma$ from both b and a. The simplest way to do this is to randomly assign a value for x, y and z between $-\lambda\sigma$ and $\lambda\sigma$. We cannot ignore negative coordinates (as we did with b) because the octants are no longer symmetrical:

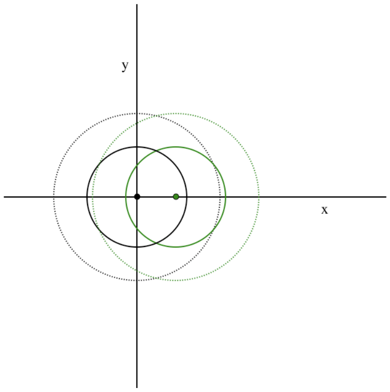

Figure 2.8 – Cross section of two overlapping square-well potentials within the hard-core radius.

The main detraction from this approach is that most of the attempted placements of c will lie at a distance beyond $\lambda\sigma$ with either a or b, only around 12.85% of attempted placements of b and c result in a usable result.

Instead we restrict the placement of c so that is within a box with height and depth equal to $2\lambda\sigma$ ($-\lambda\sigma \le y \le \lambda\sigma$ and $-\lambda\sigma \le z \le \lambda\sigma$), but with width only from $b_x - \lambda\sigma$ to $\lambda\sigma$.

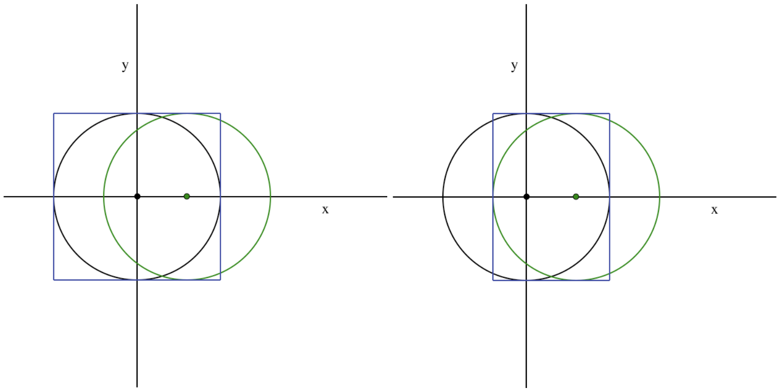

Figure 2.9 - Cross section of two overlapping square-well potentials within the hard-core radius with a box to place a third particle.

As seen in figure 2.9 (in which only solid lines representing a distance of $\lambda\sigma$ around each particle are shown for aesthetics) the probability of a particle randomly inserted in the blue box being in the volume of overlap of the two spheres is much higher for the second box. It should be noted that the particle could be inserted into only positive values for y and z since all quadrants around the x-axis are symmetric, however this does not have any advantage in run speed.

There is a problem with this optimization that must be addressed. For a well width of 2, if we compare $b_x = 1$ and $b_x = 1.5$:

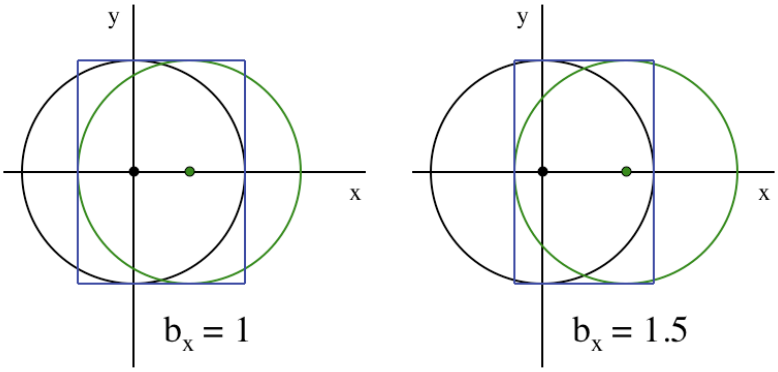

Figure 2.10 - Cross section of two overlapping square-well potentials within the hard-core radius with a box to place a third particle at different separations.

The volume of the $b_x = 1$ box is 48 (3x4x4), and the volume of the $b_x = 1.5$ box is 40 (2.5x4x4). The volume of overlap from (1.9.6) for $b_x = 1$ is $27\pi/4$ and for $b_x = 1.5$, $475\pi/96$. The probability of a particle randomly put in the box being inside the overlap is the overlap volume divided by the volume of the box. For $b_x = 1$ this is .4418 and for $b_x = 1.5$ it is .3886.

The probability of finding a particle inside the overlap needs to be proportional to the volume of overlap alone. From the volumes above $b_x = 1$ should be 1.364 times more likely to have a particle inserted in the overlap. Instead, it is 1.137 times more likely. The result is that contributions from $b_x = 1.5$ are counted more than they should be (or $b_x = 1$ less).

This is overcome by assigning an importance to each b_x as it is chosen, where the importance is equal to the probability of placing a particle inside the box ($-\lambda\sigma \le x \le \lambda\sigma$) and having it end up inside a the smaller box ($b_x - \lambda\sigma \le x \le \lambda\sigma$). Or, if I is importance:

$$I = \frac{2\lambda\sigma - b_x}{2\lambda\sigma} \tag{2.2.5}$$

In (2.2.5) $2\lambda\sigma - b_x$ is the width of the smaller box, and $2\lambda\sigma$ is the max width. After each placement of b that is within the distance $\lambda\sigma$, the importance is calculated. Then c is placed inside the smaller box a number of times proportional to the importance.

This increases the acceptance rate for placement from 12.85% to 39.14%. As we will see this becomes more significant for higher order virial coefficients because the chances of obtaining a non-zero configuration are much lower.

The technique of integrating relative volumes will be referred to in this work as “ratio integration”.

2.3 RESULTS FOR C(T)

The first we integral studied with ratio integration is the third virial coefficient. The third virial coefficient for the square-well provides the perfect test for this integration because the solution is known analytically for all well widths.

All computations in this work were performed on a 1.67 GHz processor. A run consisting of 10^7 successful samples takes about ten seconds and produces results for the four possible values of the integrand $\{ (-1)^{3-i}h^i$ for i = 0, 1, 2 and 3$\}$ that range in accuracy from .096% to .91%. Increasing the number of samples to 10^9 increases the runtime to 17 minutes and the accuracy to a range from .006% to .13%.

The output is the number of times each integrand value is sampled. A typical output for 10^9 samples would be:

λ	-1	h	$-h^2$	h^3
2	15630522	53053895	425035410	506280385
1.5	87768649	232867305	473573669	205790979

Table 2.1 – Ratio integration results in terms of hits for C(T).

or in terms of percentage:

λ	-1	h	$-h^2$	h^3
2	.01563052	.05305388	.42503532	.50628028
1.5	.0877686	.23286716	.47357388	.20579086

Table 2.2 – Ratio integration results in terms of volume percent for C(T).

The simplest test of accuracy, which is also useful for higher order virial coefficients whose integrals cannot been checked analytically, is to compare the percentage of the first integrand to the value $\lambda^{-3(n-1)}$ (where n is the virial coefficient we are examining, in this case 3). For λ = 2 this is 2^{-6} or .015625 and for λ =1.5, .0877915.

To calculate the coefficient for each integrand value, one takes the value of the third virial coefficient for hard spheres and multiplies it by the number of times the integrand value was sampled (from table 2.1) and normalizes it by dividing by the number of times the first integrand was sampled (-1 column in table 2.1). The results for table 2.1 are:

$$C(T) = -\frac{b_0^2}{8}\left[-5 + 16.97h - 135.96h^2 + 161.95h^3\right] \qquad \lambda = 2$$

$$C(T) = -\frac{b_0^2}{8}\left[-5 + 13.27h - 26.98h^2 + 11.72h^3\right] \qquad \lambda = 1.5$$

(2.3.1)

The results for λ = 2 can be compared to the actual value in (2.2.1). For λ =1.5 the analytical answer is (rounded to the hundredths digit):

$$C(T) = -\frac{b_0^2}{8}\left[-5 + 13.27h - 26.97h^2 + 11.72h^3\right] \qquad (2.3.2)$$

Comparison at all well widths (λ) to the analytically calculated coefficients shows good accuracy.

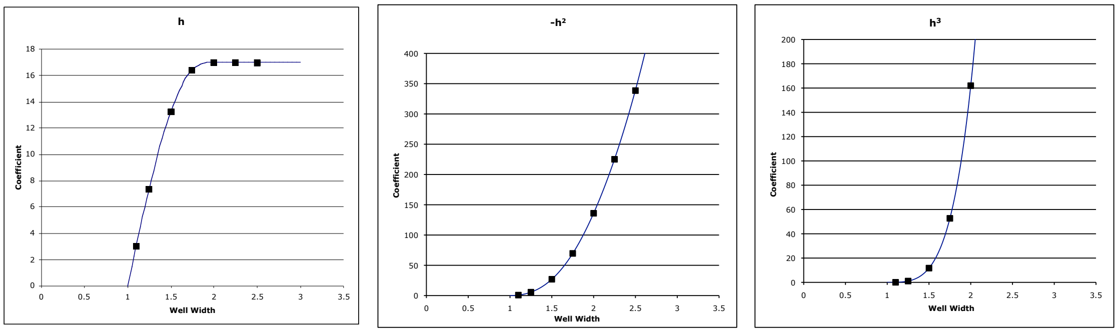

Figure 2.11 – Integrand coefficients for C(T) calculated at different well widths with ratio integration (black squares) and the exact values from equation 1.8.32 (blue lines).

2.4 RESULTS FOR D_1(T)

To further test the ability of the ratio integration technique results for D_1(T) were also calculated and compared to the analytical solution. Again the first particle (a) is taken to be at the origin. The second particle (b) is placed on the x-axis between zero and $\lambda\sigma$ using (2.2.4). The third particle (c) does not have to over lap the first, so it must be allowed to be placed outside the box we have been placing the other particles in. This is accomplished by placing it relative to particle b. So c_x is:

$$c_x = 2\lambda\sigma(\ rand() - .5) + b_x \tag{2.4.1}$$

with y and z coordinates both assigned by:

$$2\lambda\sigma(rand() - .5) \tag{2.4.2}$$

The last particle (d) must overlap c and a. It can be placed in the cube with sides of length $\lambda\sigma$ with a as its center, and reject any placement that leaves it at a distance greater than $\lambda\sigma$ to a or c.

Any random placement that would result in a zero-valued integrand (any placement with a distance greater than $\lambda\sigma$ between particles with an f-bond in the integral of interest) resets the hit-and-miss algorithm. That is to say, if particles b and c are placed successfully, and particle d is placed outside the range of c; b and c must be placed again. If b and c's positions were kept, sampling of less favorable configurations (with only a small volume available to d for a successful placement) would be over-counted (and therefore samplings of favorable configurations would be undercounted).

A plot of 10^9 samples vs. the Barker and Monaghan solution (1.11.5) reveals the high accuracy of the ratio integration technique.

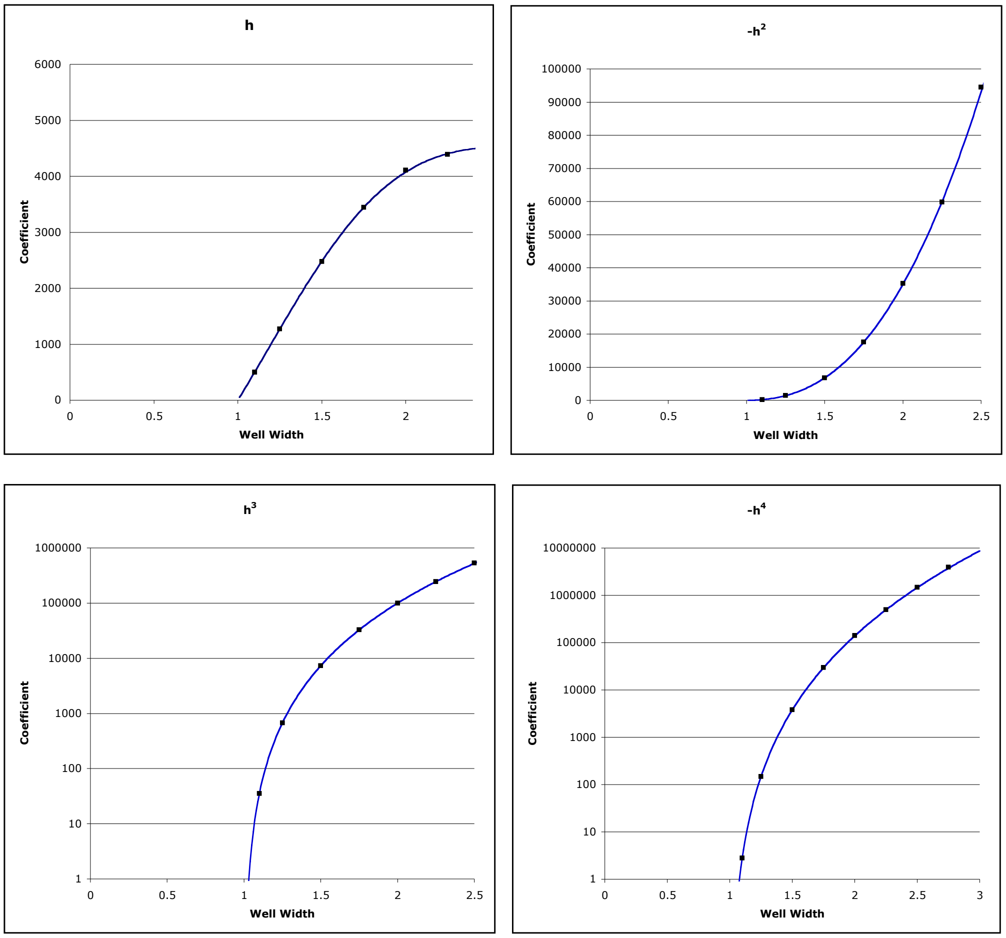

Figure 2.12 - Integrand coefficients for $D_1(T)$ calculated at different well widths with ratio integration (black squares) and exact values (blue lines).

Note that for h^3 and h^4 in figure 2.12 the coefficient axis is in logarithmic scale for ascetics. Each run (10^9 samples) contributed data for each coefficient at the well width sampled (each run contributes one data point to each graph in figure 2.12).

λ	-1	h	$-h^2$	h^3	$-h^4$
1.1	544	501.37	199.42	35.095	2.7945
1.25	544	1272.08	1417.98	671.21	148.01
1.5	544	2479.84	6773.78	7329.62	3785.44
1.75	544	3438.62	17566.56	32669.13	29524.11
2	544	4079.97	34987.11	99675.38	139245
2.25	544	4397.87	59913.77	245101.68	494015.01
2.5	544	4560.94	93064.80	523760.11	1453274
2.75	544	4543.95	135086.90	1013136.6	3739920

Table 2.3 – Integrand coefficients for $D_1(T)$ predicted by ratio integration.

Compared to the exact value (1.11.5):

λ	-1	h	$-h^2$	h^3	$-h^4$
1.1	544	501.30	199.63	34.99	2.80
1.25	544	1271.83	1418	671.37	147.916
1.5	544	2480.87	6777.38	7328.71	3782.22
1.75	544	3442.64	17576.59	32678.49	29499.90
2	544	4075	35007	99687	139215
2.25	544	4402.06	59941.31	245191.10	493894.71
2.5	544	4520.55	93034.35	523950.24	1453146
2.75	544	4543.09	134893.22	1013182.9	3740039

Table 2.4 – Exact integrand coefficients for $D_1(T)$.

The average error in the ratio integration of D1 is .086%.

2.5 RESULTS FOR $D_2(T)$

The integral for D_2 is performed in an analogous way. The only difference is the third particle must lie within $\lambda\sigma$ of the first. We could choose to have the fourth particle lie within $\lambda\sigma$ of the second instead, but it is fastest to put required conditions as early in the Monte Carlo process so zero-valued integrands are rejected as soon as possible.

The D_2 virial integrate is the highest order integral known analytically for a square-well potential, and represents the last chance to test the ratio integration method.

As always, we can calculate the percentage of the volume in the integral where all f-bonds have the value –1. Comparing the results of the ratio integration to the analytical percentage [$100*(\lambda\sigma)^{-9}$] the average error is .94%. The majority of the error occurs at larger well depths, where the expected volume percent for all bonds inside the hard sphere radius is very small. The average error for $\lambda\sigma \leq 2$ is .29%.

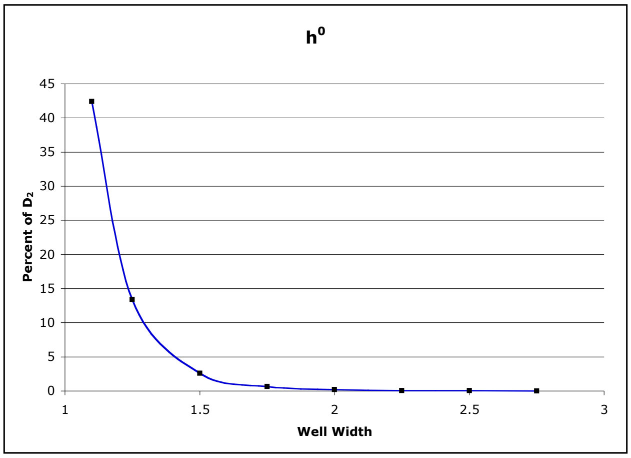

Figure 2.13 - Integrand coefficients for $D_2(T)$ calculated at different well widths with ratio integration (black squares) and exact values (blue lines).

The remaining coefficients can be compared to Barker's D_2 for $\lambda > 2$ (1.12.5) and Hauge's value for $\lambda < 2$ (1.12.6).

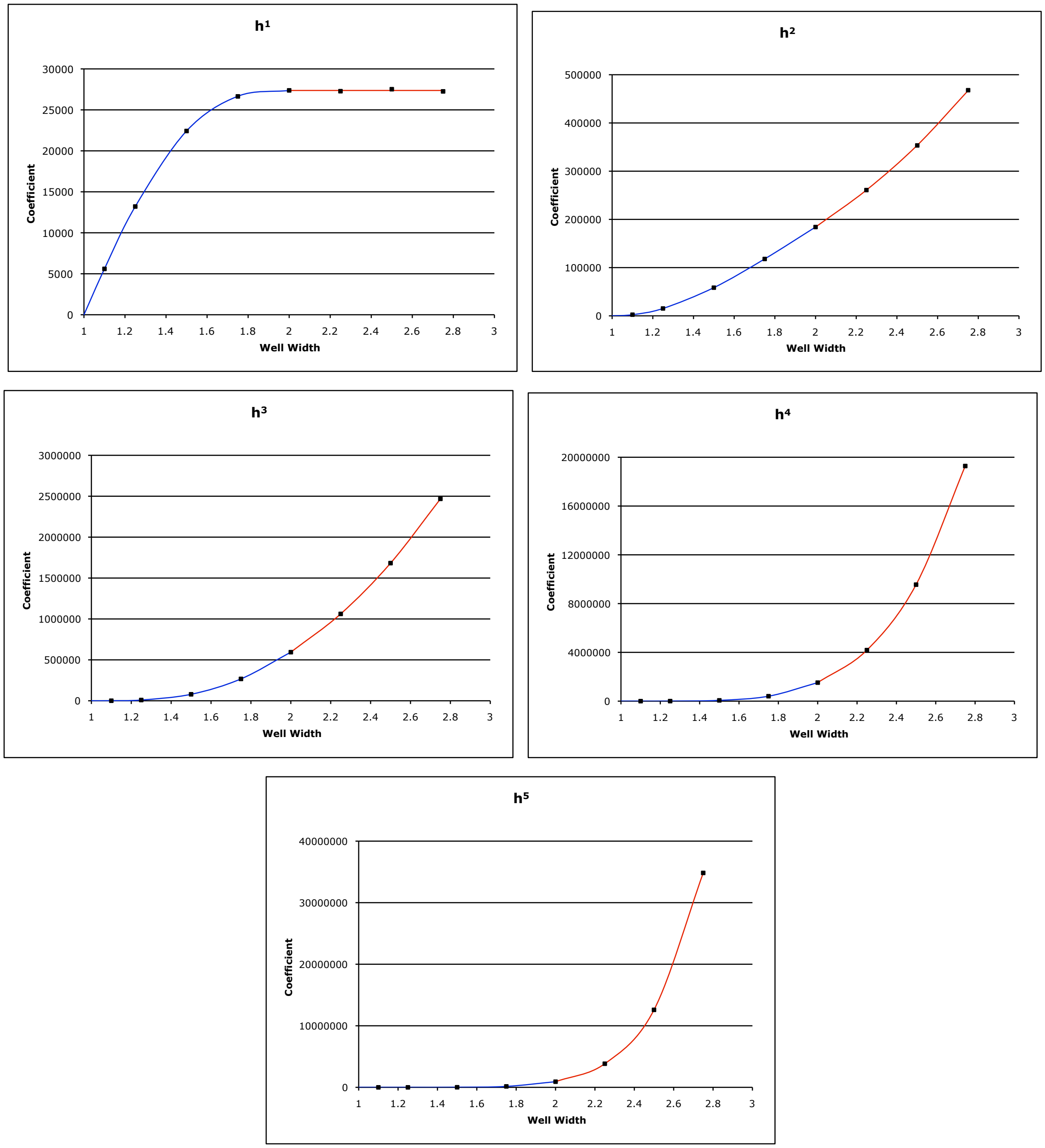

Figure 2.14 – Ratio integration results for D_2 compared to results from Hauge (red) and Barker (blue).

The accuracy for each coefficient is very high with nearly all error arising for near zero values of the coefficients. For example below $\lambda = 2$, h^0 was accurate to within .25% but at $\lambda = 2.75$ the error was 2.9% where h^0 only represents .01% of the integrated volume. Although this is a larger percent error, it is a very small deviation in a small portion of the integral.

Coefficient	Error
h^0	.94%
h^1	.18%
h^2	.06%
h^3	.05%
h^4	.09%
h^5	.39%

Table 2.5 – Average absolute error between predicted and exact coefficients for the well-widths studied.

2.6 RESULTS FOR D_3(T)

The ratio integration method can be used to solve D_3 for the square-well potential as it was used to solve D_1 and D_2. For D_3 each particle placed must be within $\lambda\sigma$ of all particles placed before it.

As with C(T), faster integration can be accomplished by restricting the volume available to the third and fourth particles. We again restrict only the x component (since b is on the x-axis) to within (b_x - σ) and σ. For C(T) we calculated the importance of each placement of b, and sampled c proportionally, with equation (2.2.5). Because we are placing 2 particles in the restricted volume, the importance must be the probability of placing two particles in the smaller volume, which is simply the probability of placing an individual particle squared.

$$I = \frac{(2\lambda\sigma - b_x)^2}{4\lambda^2\sigma^2} \tag{2.6.1}$$

Because the importance only needs to be proportional to the probability, we could ignore the denominator in (2.6.1), however we would not know the maximum samples to be taken before setting the well width. For example, we may sample 500*I for each placement of b (rounded to the nearest integer), leaving a maximum of 500 samples for each placement of b (corresponding to b being placed at the origin) no matter what the well width.

To justify this quick integration technique D_3 was solved in the slower method for several well widths. There was no loss of accuracy despite the large gain in runtime between the two methods.

From rule 1 in section 1.11, we know that the percentage of D_3 volume integral due to all distance being less than σ, should be the $(\lambda\sigma)^{-9}$. We therefore have one last test of accuracy for the ratio integration technique. The average error in the percentage of h^0 is .079%.

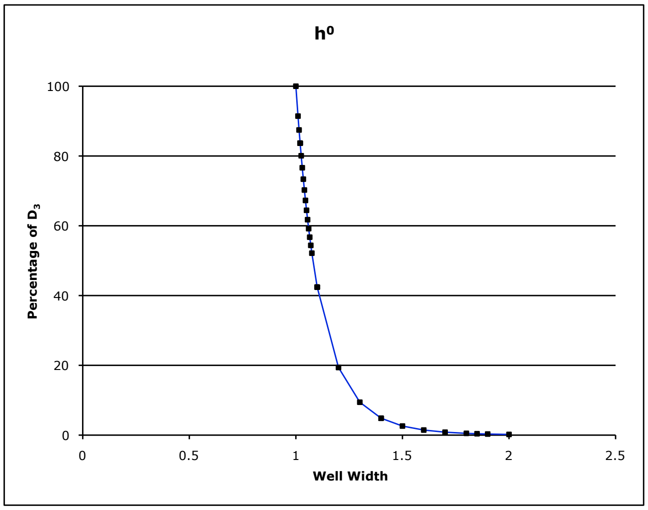

Figure 2.13 – Volume percent of D_3 predicted by ratio integration for the integrand h^0 with a best-fit line.

For each coefficient, the results can be graphed and fitted to a curve. This allows us to determine the solution for an arbitrary well width through interpolation, rather than performing a unique simulation for each well width of interest.

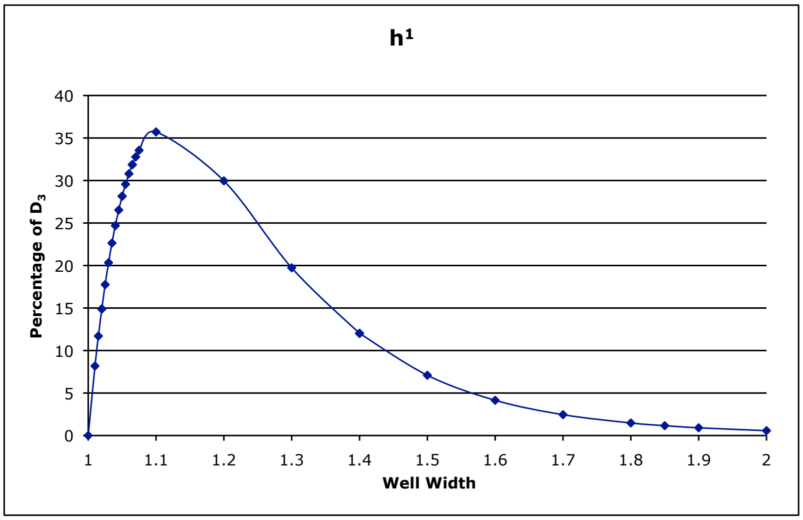

Figure 2.14 – Volume percent of D_3 predicted by ratio integration for the integrand h^1 with a best-fit line.

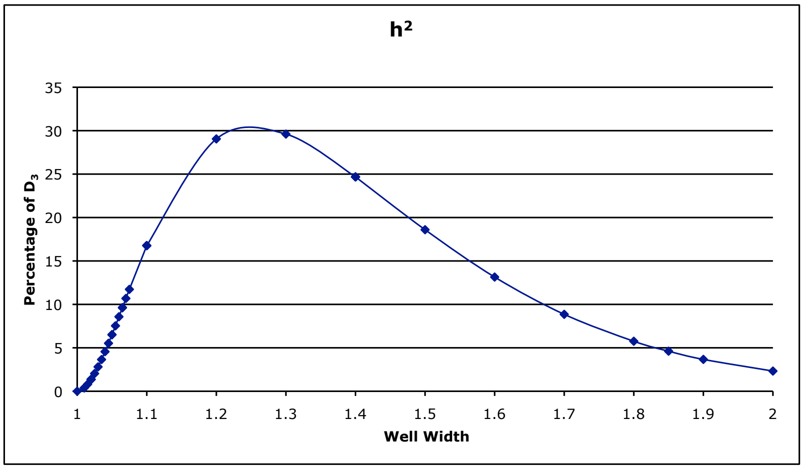

Figure 2.15 – Volume percent of D_3 predicted by ratio integration for the integrand h^2 with a best-fit line.

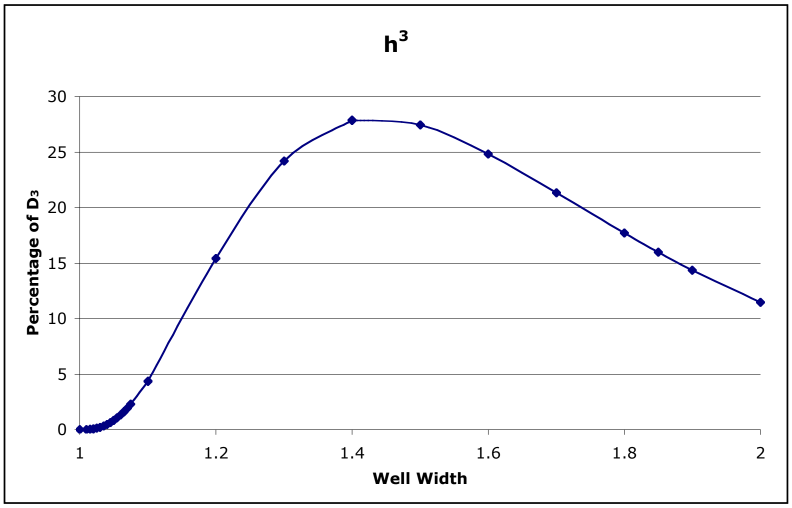

Figure 2.16 – Volume percent of D_3 predicted by ratio integration for the integrand h^3 with a best-fit line.

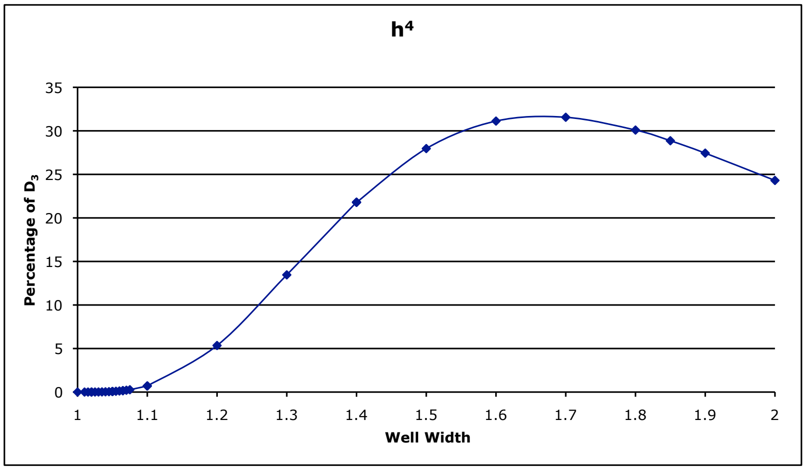

Figure 2.17 – Volume percent of D_3 predicted by ratio integration for the integrand h^4 with a best-fit line.

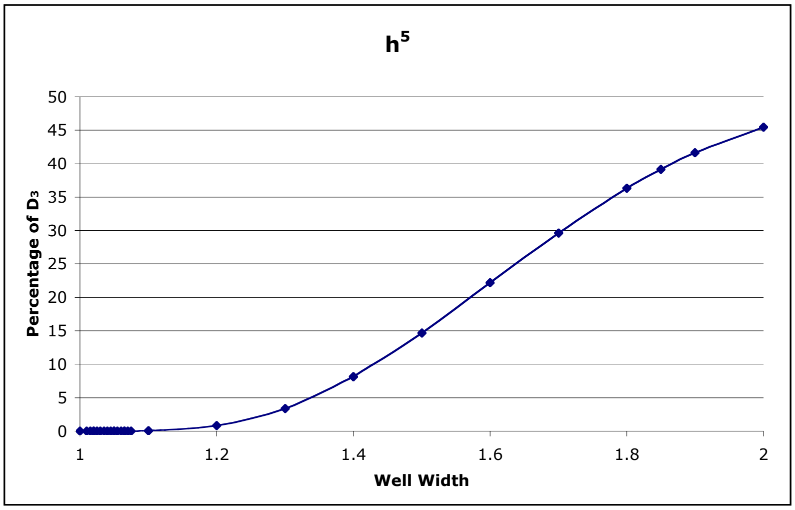

Figure 2.18 – Volume percent of D_3 predicted by ratio integration for the integrand h^5 with a best-fit line.

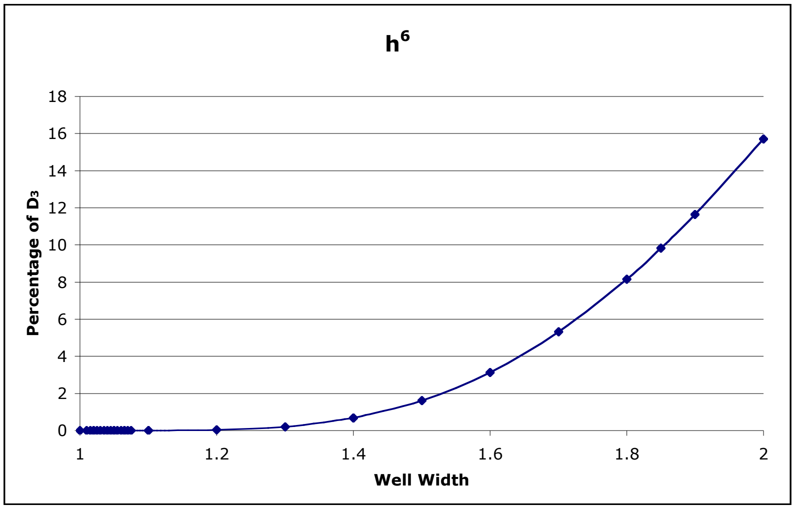

Figure 2.19 – Volume percent of D_3 predicted by ratio integration for the integrand h^6 with a best-fit line.

2.7 RESULTS FOR E(T)

The fifth virial coefficient is described by 10 cluster integrals as shown in Figure 2.5. Ratio integration has been performed on all cluster integrals in the same manner as the D(T) integrals. Each particle is placed inside a set volume and all f-bonds pertaining to that particle and particles already in place are checked to ensure distances are less than $\lambda\sigma$.

As noted in 2.5, particles are ordered to promote early rejection of zero-valued configurations. For example $E_8(T)$ from Figure 2.5 could be labeled either of the following ways:

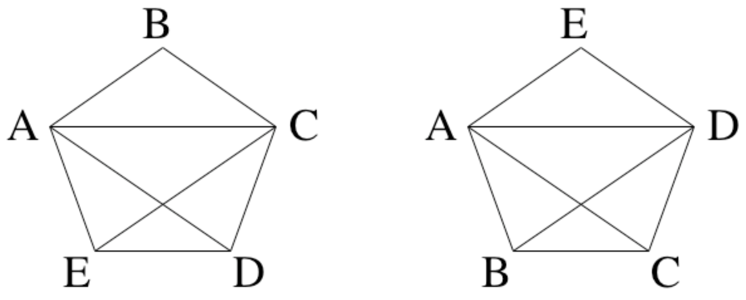

Figure 2.20 – Labeling possibilities for $E_8(T)$.

In the first diagram of figure 2.20 particle D must be placed inside the spheres of A and C, while in the second diagram D must be placed inside the spheres of A, B and C. E must be placed in spheres A, C and D in the first labeling and only inside A and D in the second. Both diagrams should encounter the same percentage of rejections, however fewer restrictions on E for the second diagram and more on D translates into more rejections before E is placed. This means fewer calls to the random number generator and fewer distance calculations (which is the slowest part of the application). The optimal labeling in figure 2.20 decreases the computation time by 15%.

Coefficients are generated in the same manner as section 2.3 using hard sphere literature values[9]. Again, we can graph the coefficients as a function of well depth and determine the values for well depths not run through interpolation.

E10

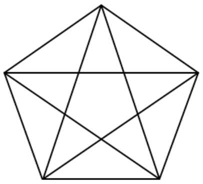

-0.023707

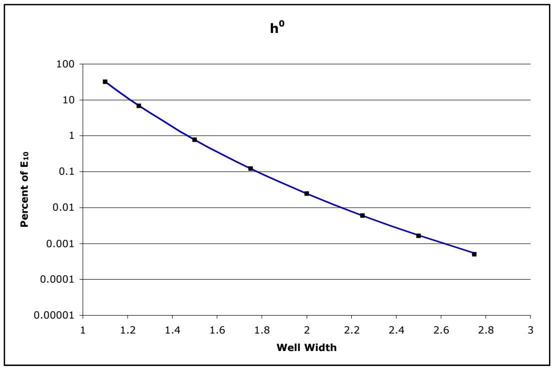
h^0
Percent of E_{10}
100
10
1
0.1
0.01
0.001
0.0001
0.00001
1
1.2
1.4
1.6
1.8
2
2.2
2.4
2.6
2.8
3
Well Width

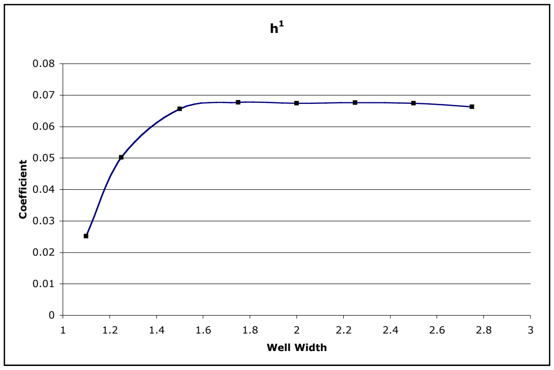
h^1
Coefficient
0.08
0.07
0.06
0.05
0.04
0.03
0.02
0.01
0
1
1.2
1.4
1.6
1.8
2
2.2
2.4
2.6
2.8
3
Well Width

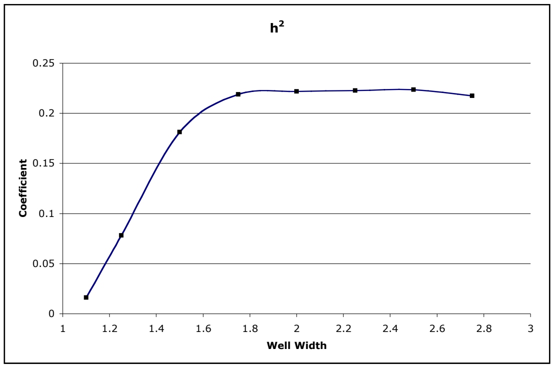
h^2
Coefficient
0.25
0.2
0.15
0.1
0.05
0
1
1.2
1.4
1.6
1.8
2
2.2
2.4
2.6
2.8
3
Well Width

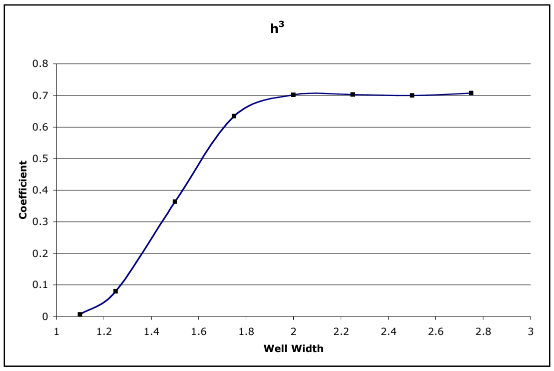
h^3
Coefficient
0.8
0.7
0.6
0.5
0.4
0.3
0.2
0.1
0
1
1.2
1.4
1.6
1.8
2
2.2
2.4
2.6
2.8
3
Well Width

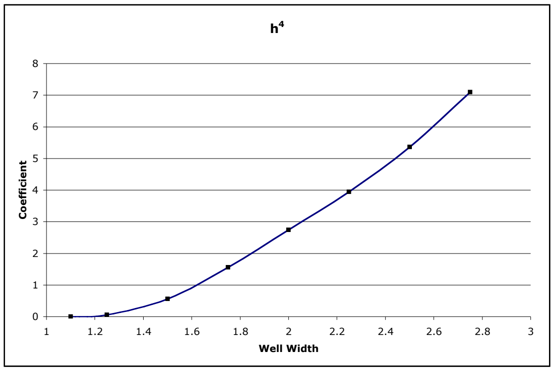
h^4
Coefficient
8
7
6
5
4
3
2
1
0
1
1.2
1.4
1.6
1.8
2
2.2
2.4
2.6
2.8
3
Well Width

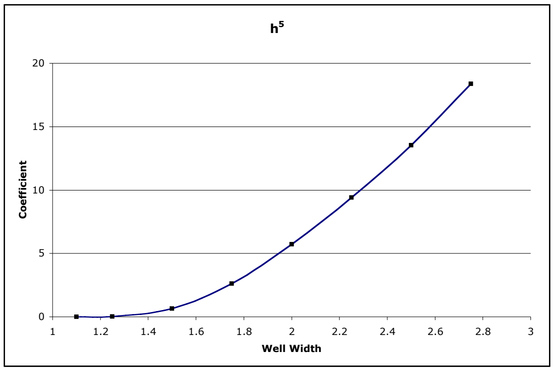
h^5
Coefficient
20
15
10
5
0
1
1.2
1.4
1.6
1.8
2
2.2
2.4
2.6
2.8
3
Well Width

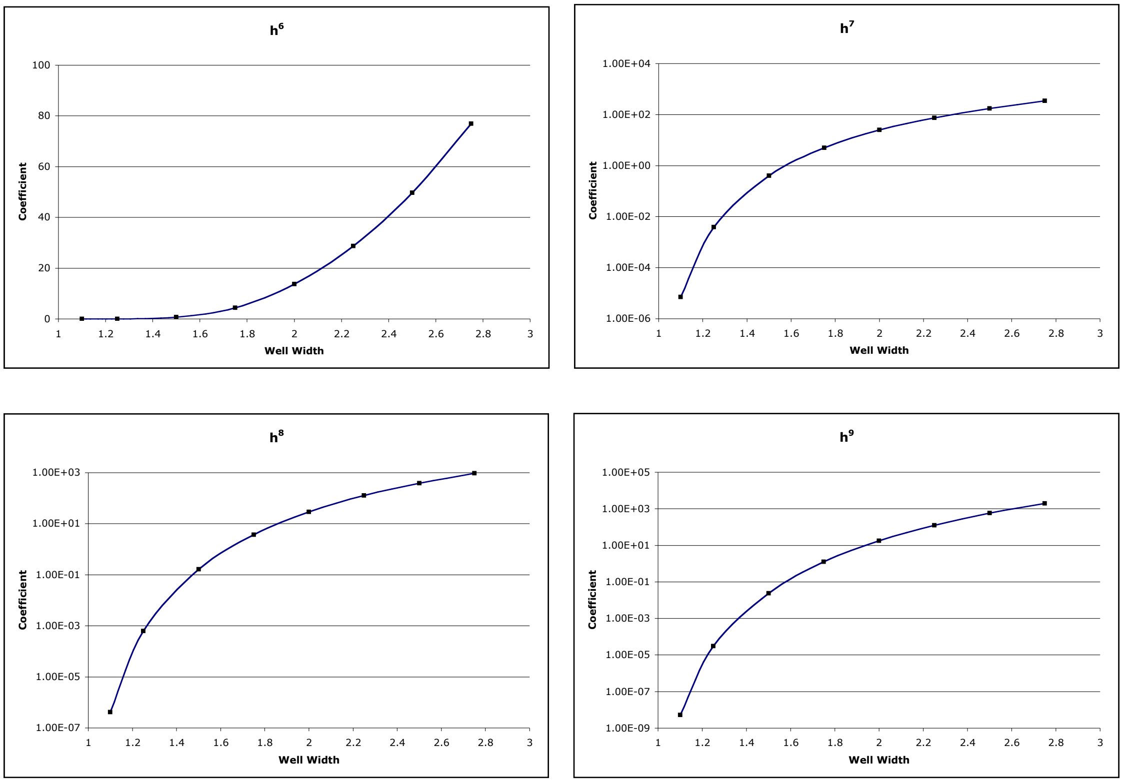

Figure 2.21 – Ratio integration results for $E_{10}(T)$ with diagram and coefficient (squares are simulations, lines are best fit).

E9

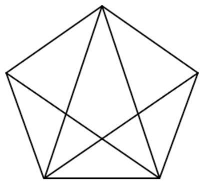

0.30490713

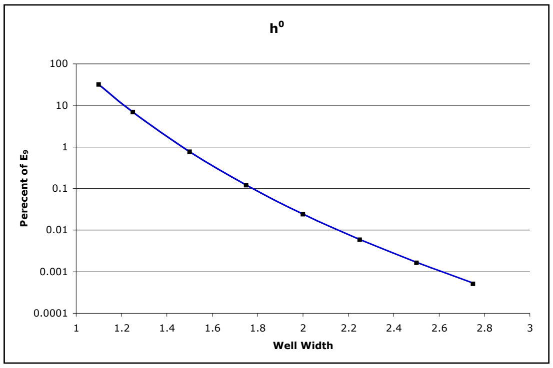

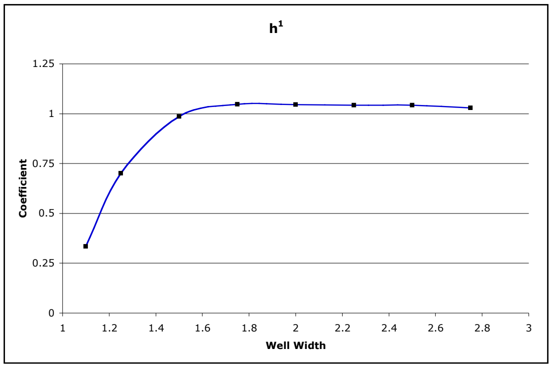

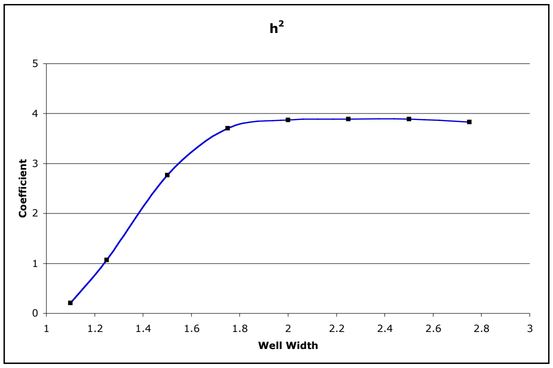

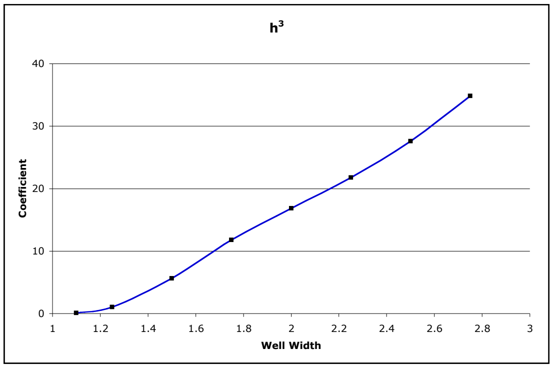

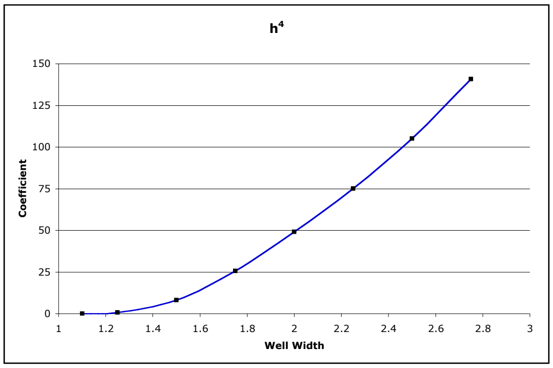

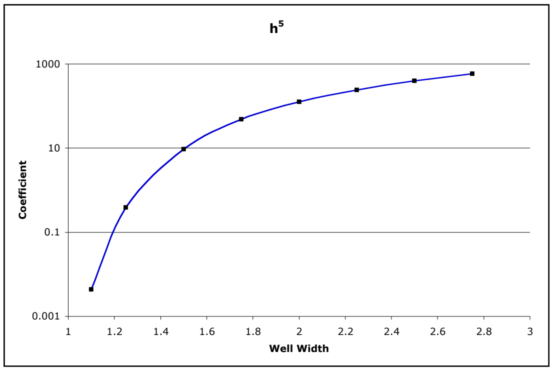

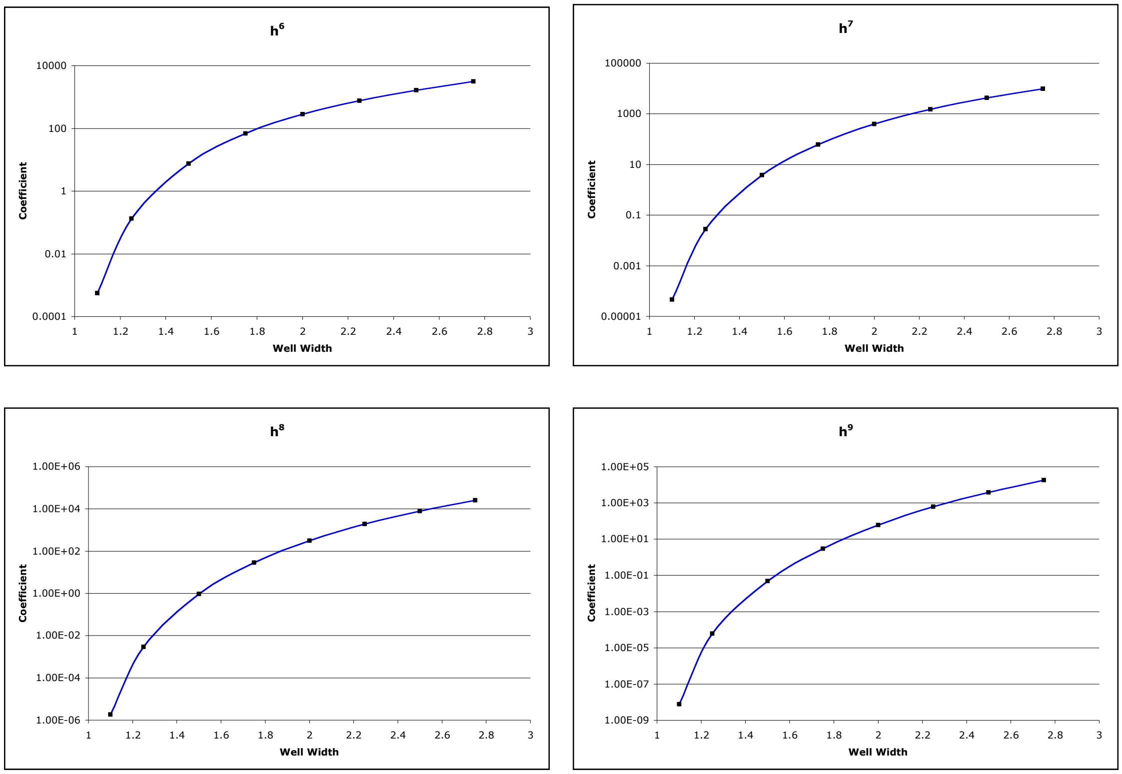

Figure 2.22 – Ratio integration results for $E_9(T)$ with diagram and coefficient (symbols as in 2.21).

E8

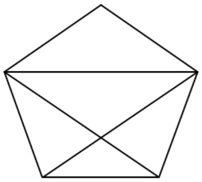

-1.3298074

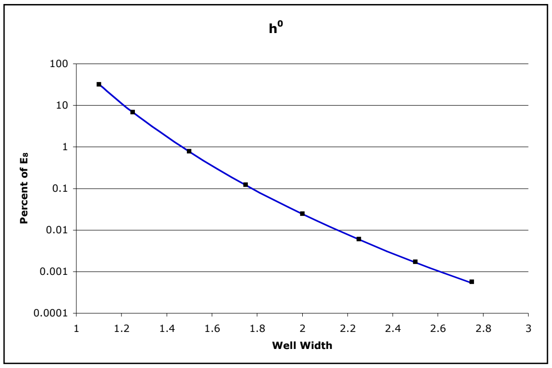
h^0
Percent of E_8
100
10
1
0.1
0.01
0.001
0.0001
1
1.2
1.4
1.6
1.8
2
2.2
2.4
2.6
2.8
3
Well Width

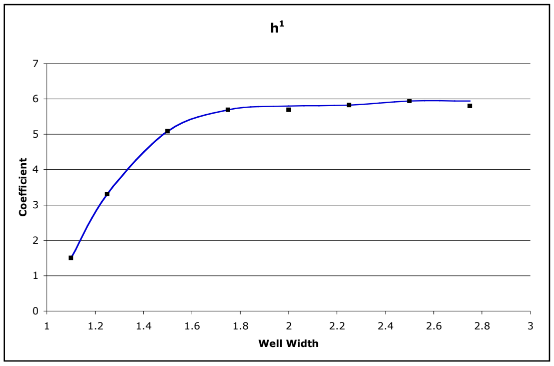
h^1
Coefficient
7
6
5
4
3
2
1
0
1
1.2
1.4
1.6
1.8
2
2.2
2.4
2.6
2.8
3
Well Width

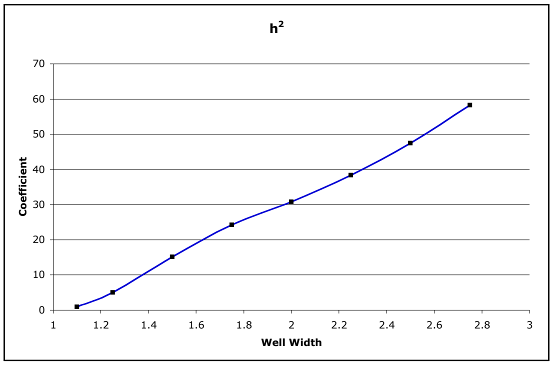
h^2
Coefficient
70
60
50
40
30
20
10
0
1
1.2
1.4
1.6
1.8
2
2.2
2.4
2.6
2.8
3
Well Width

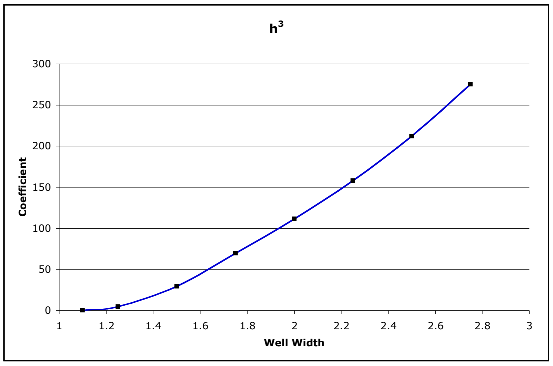
h^3
Coefficient
300
250
200
150
100
50
0
1
1.2
1.4
1.6
1.8
2
2.2
2.4
2.6
2.8
3
Well Width

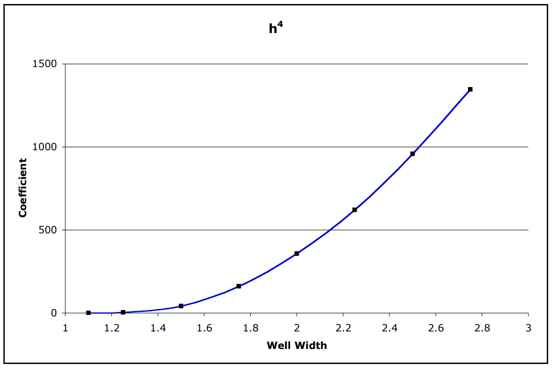
h^4
Coefficient
1500
1000
500
0
1
1.2
1.4
1.6
1.8
2
2.2
2.4
2.6
2.8
3
Well Width

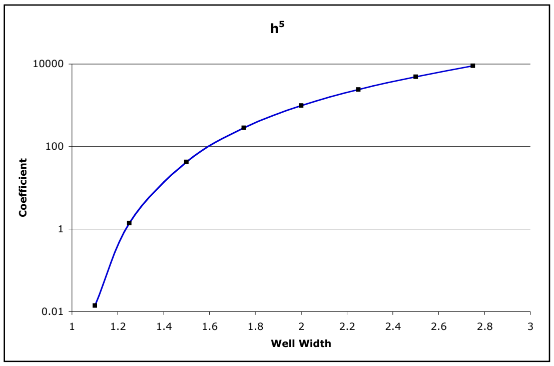
h^5
Coefficient
10000
100
1
0.01
1
1.2
1.4
1.6
1.8
2
2.2
2.4
2.6
2.8
3
Well Width

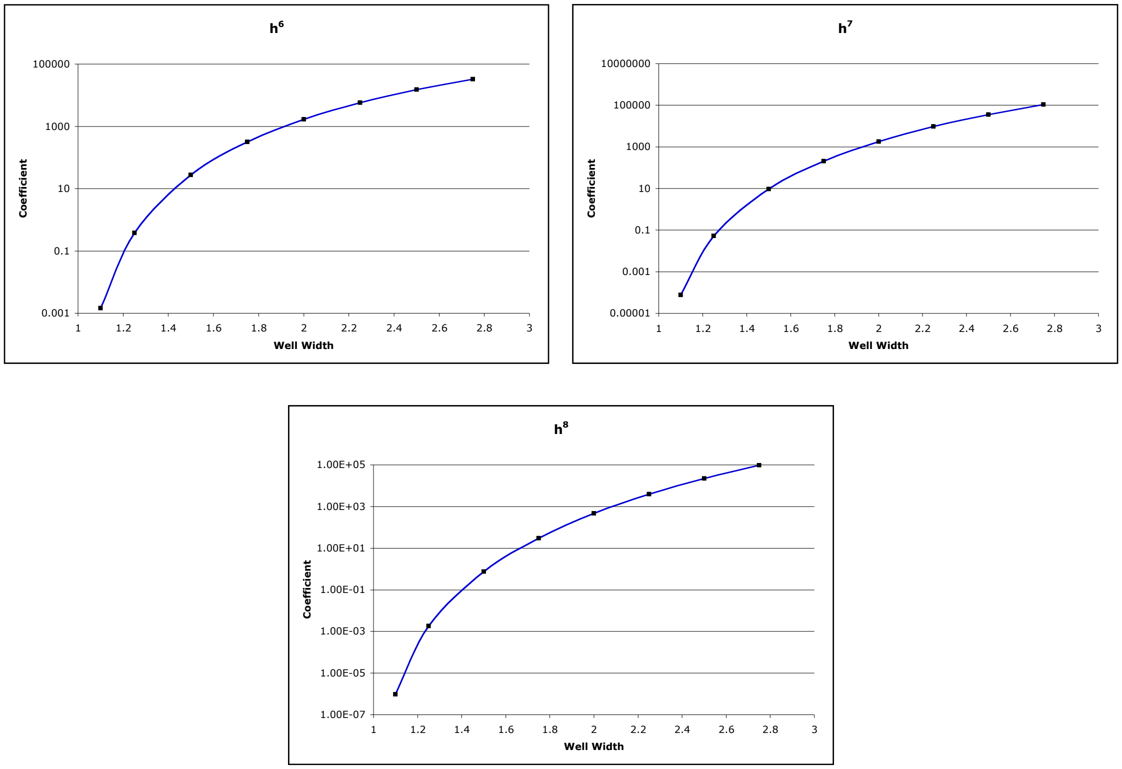

Figure 2.23 – Ratio integration results for $E_8(T)$ with diagram and coefficient (symbols as in 2.21).

E7

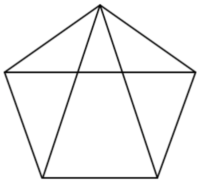

-0.5696582

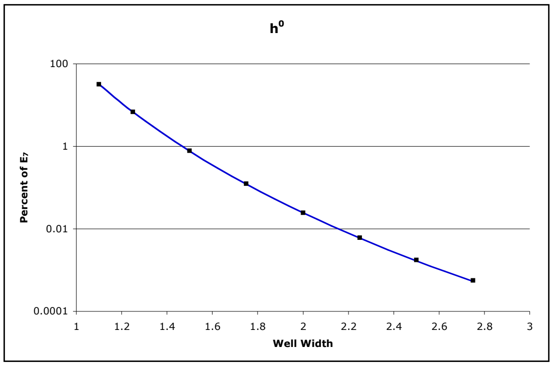
h^0
Percent of E_7
100
1
0.01
0.0001
1
1.2
1.4
1.6
1.8
2
2.2
2.4
2.6
2.8
3
Well Width

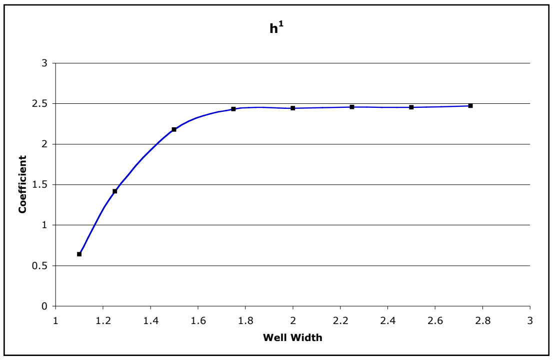
h^1
Coefficient
3
2.5
2
1.5
1
0.5
0
1
1.2
1.4
1.6
1.8
2
2.2
2.4
2.6
2.8
3
Well Width

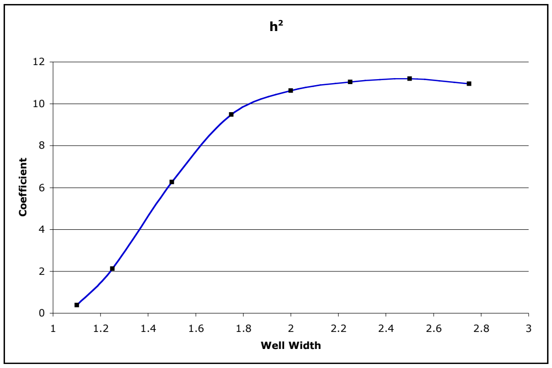
h^2
Coefficient
12
10
8
6
4
2
0
1
1.2
1.4
1.6
1.8
2
2.2
2.4
2.6
2.8
3
Well Width

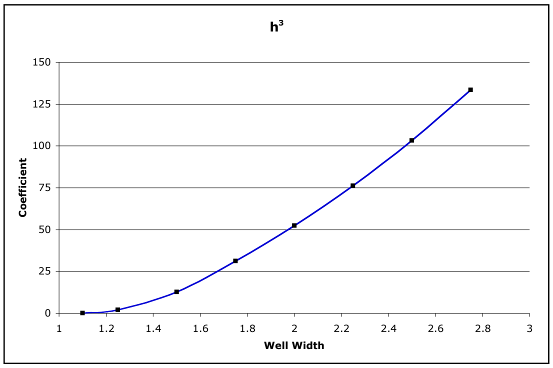
h^3
Coefficient
150
125
100
75
50
25
0
1
1.2
1.4
1.6
1.8
2
2.2
2.4
2.6
2.8
3
Well Width

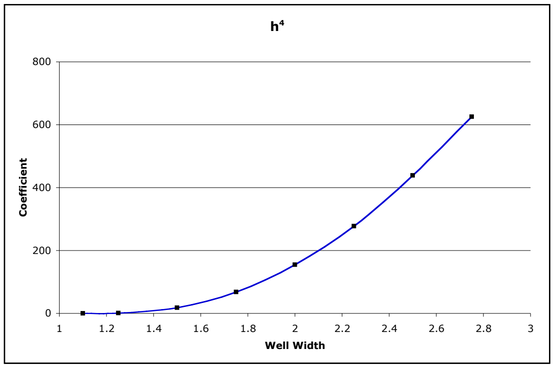
h^4
Coefficient
800
600
400
200
0
1
1.2
1.4
1.6
1.8
2
2.2
2.4
2.6
2.8
3
Well Width

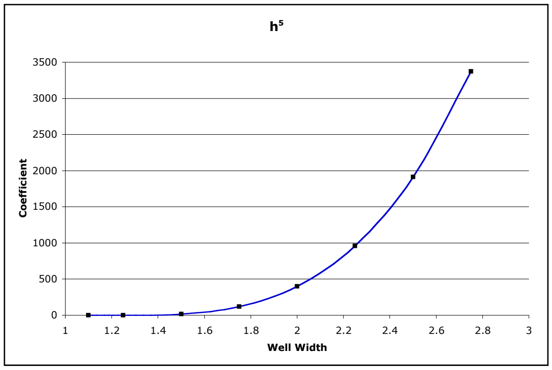
h^5
Coefficient
3500
3000
2500
2000
1500
1000
500
0
1
1.2
1.4
1.6
1.8
2
2.2
2.4
2.6
2.8
3
Well Width

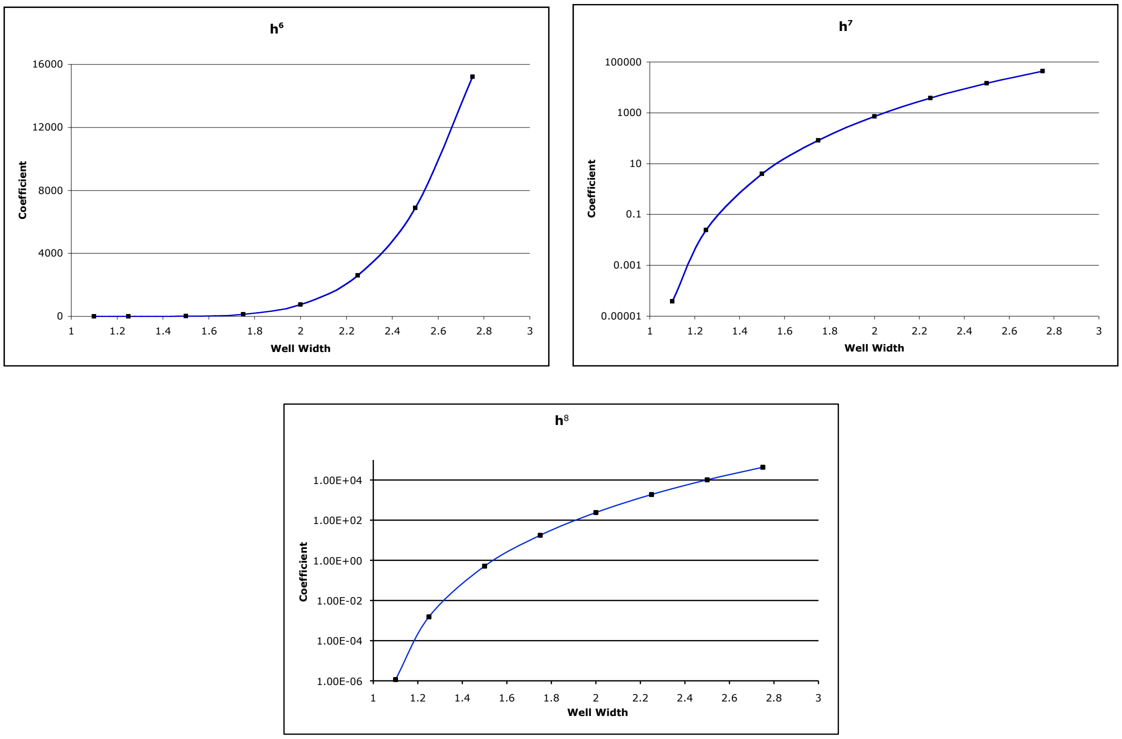

Figure 2.24 – Ratio integration results for $E_7(T)$ with diagram and coefficient (symbols as in 2.21).

E6

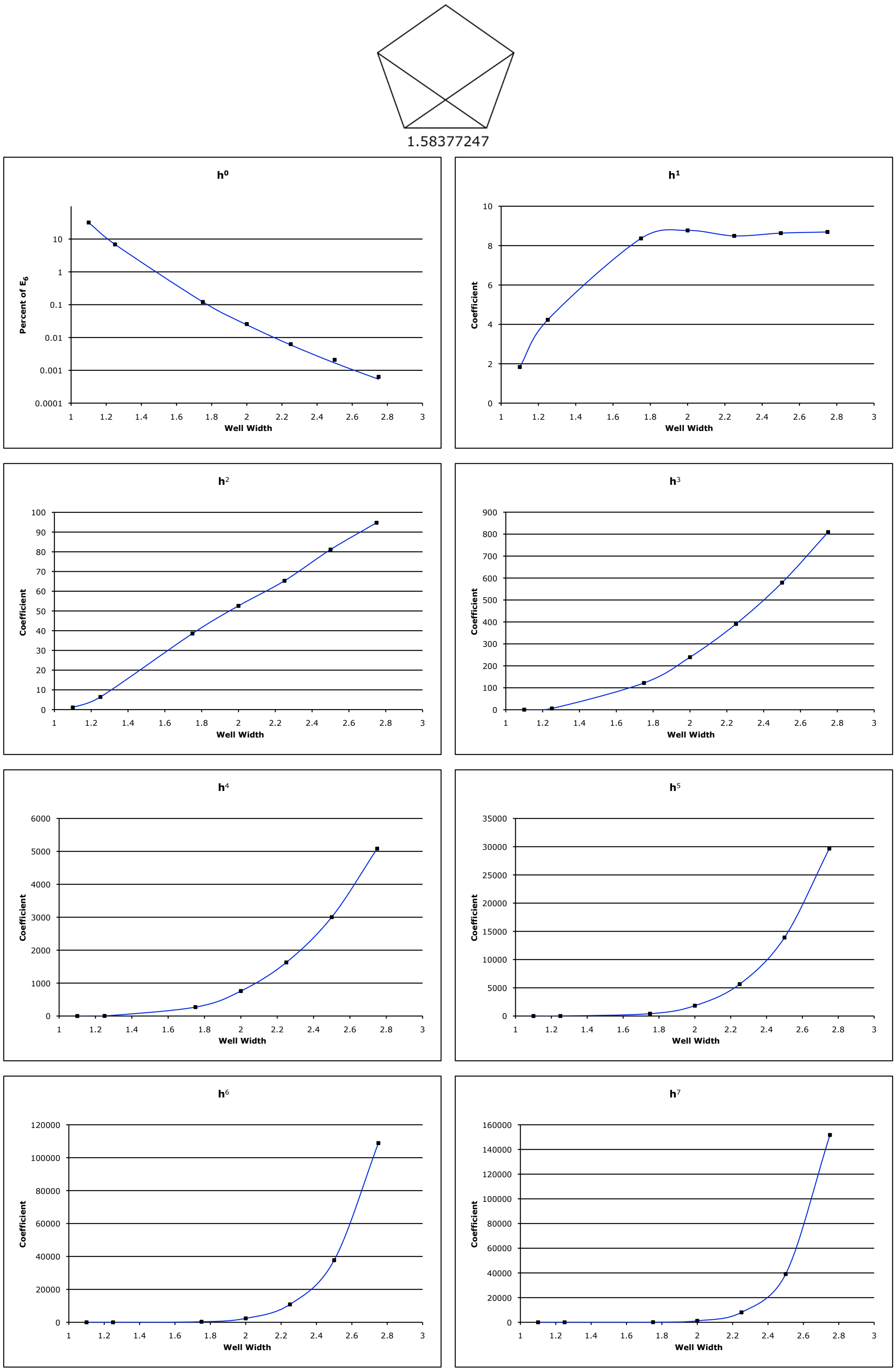

Figure 2.25 – Ratio integration results for $E_6(T)$ with diagram and coefficient (symbols as in 2.21).

E5

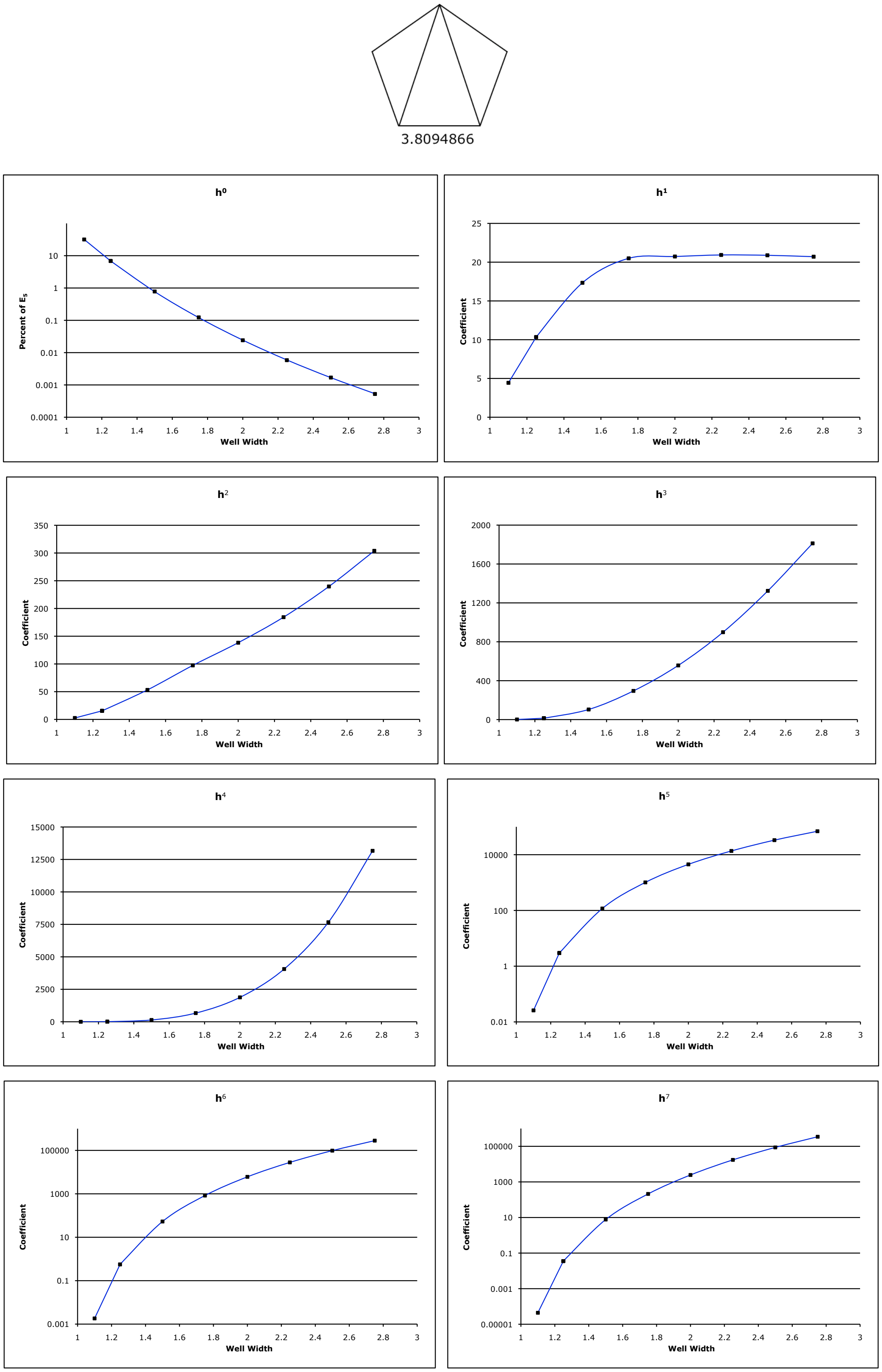

Figure 2.26 – Ratio integration results for $E_5(T)$ with diagram and coefficient (symbols as in 2.21).

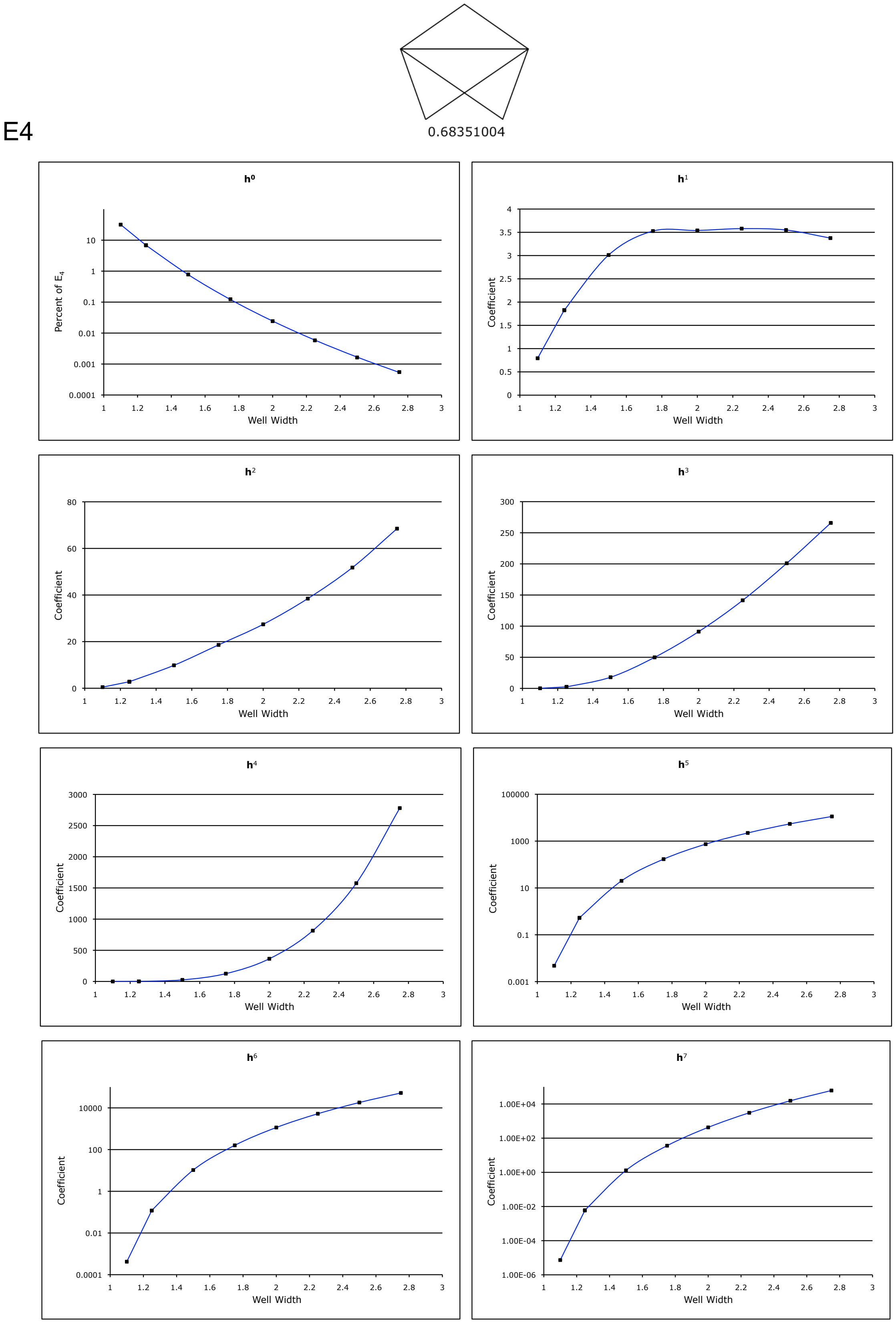

Figure 2.27 – Ratio integration results for $E_4(T)$ with diagram and coefficient (symbols as in 2.21).

E3

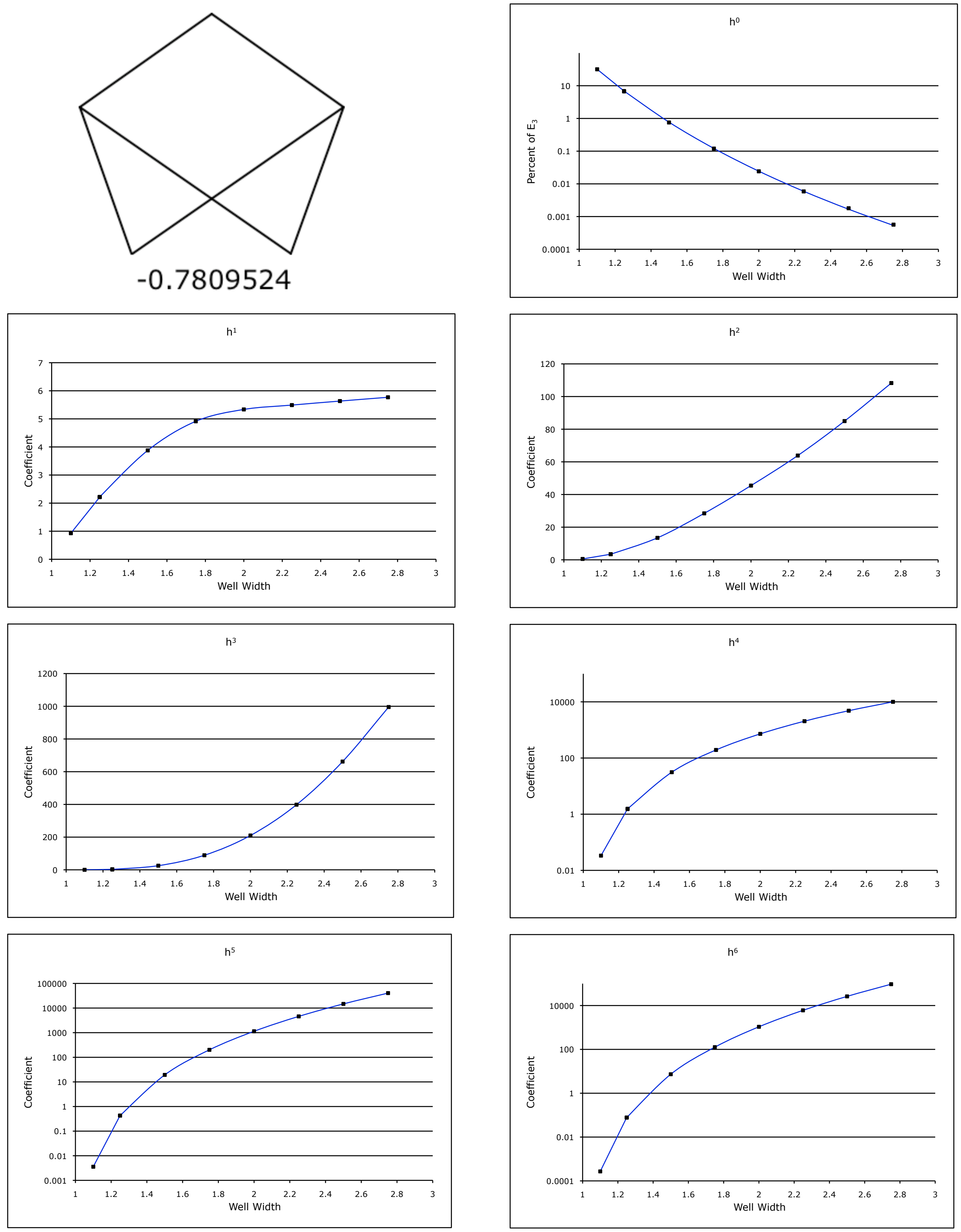

Figure 2.28 – Ratio integration results for $E_3(T)$ with diagram and coefficient (symbols as in 2.21).

E2

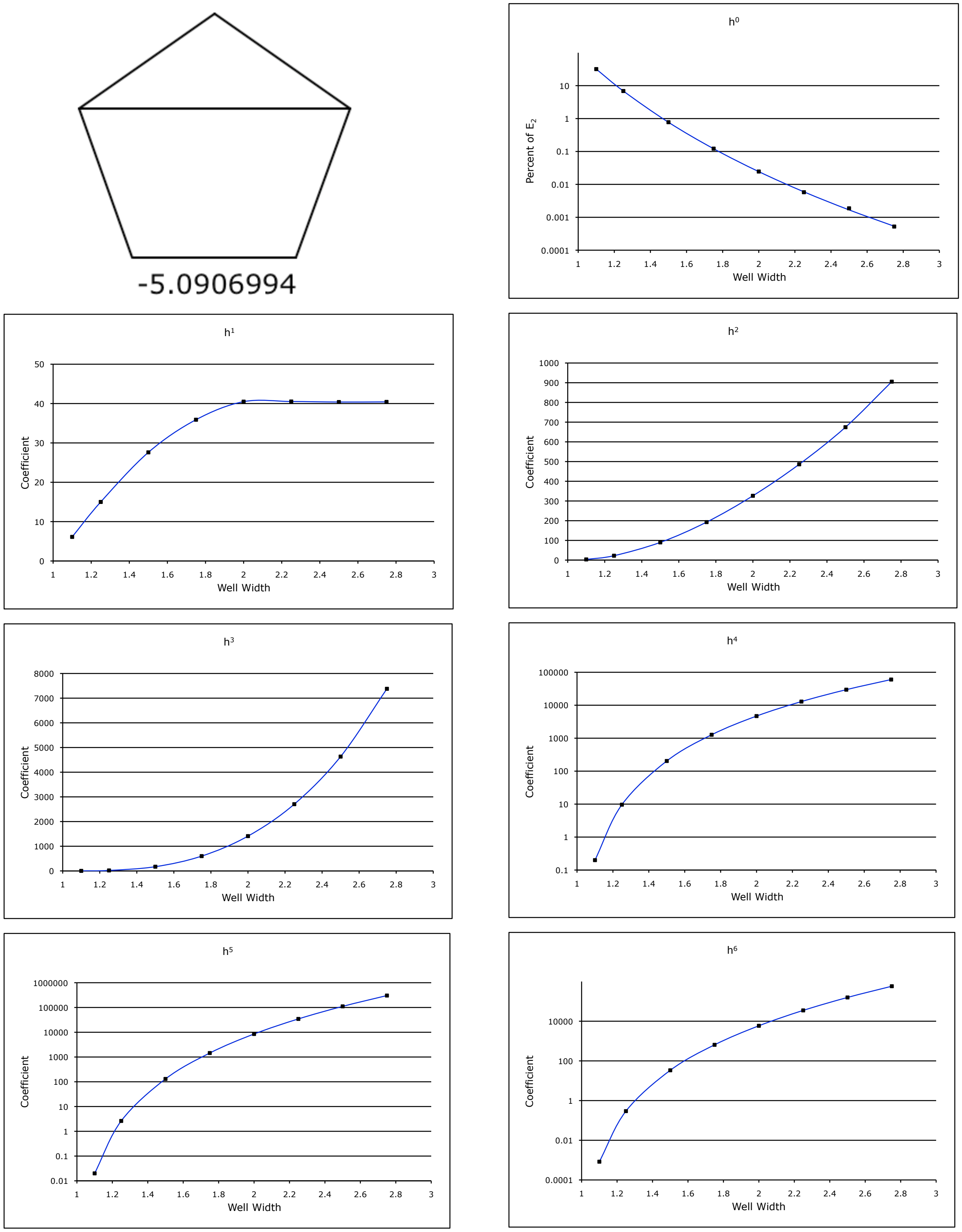

Figure 2.29 – Ratio integration results for $E_2(T)$ with diagram and coefficient (symbols as in 2.21).

E1

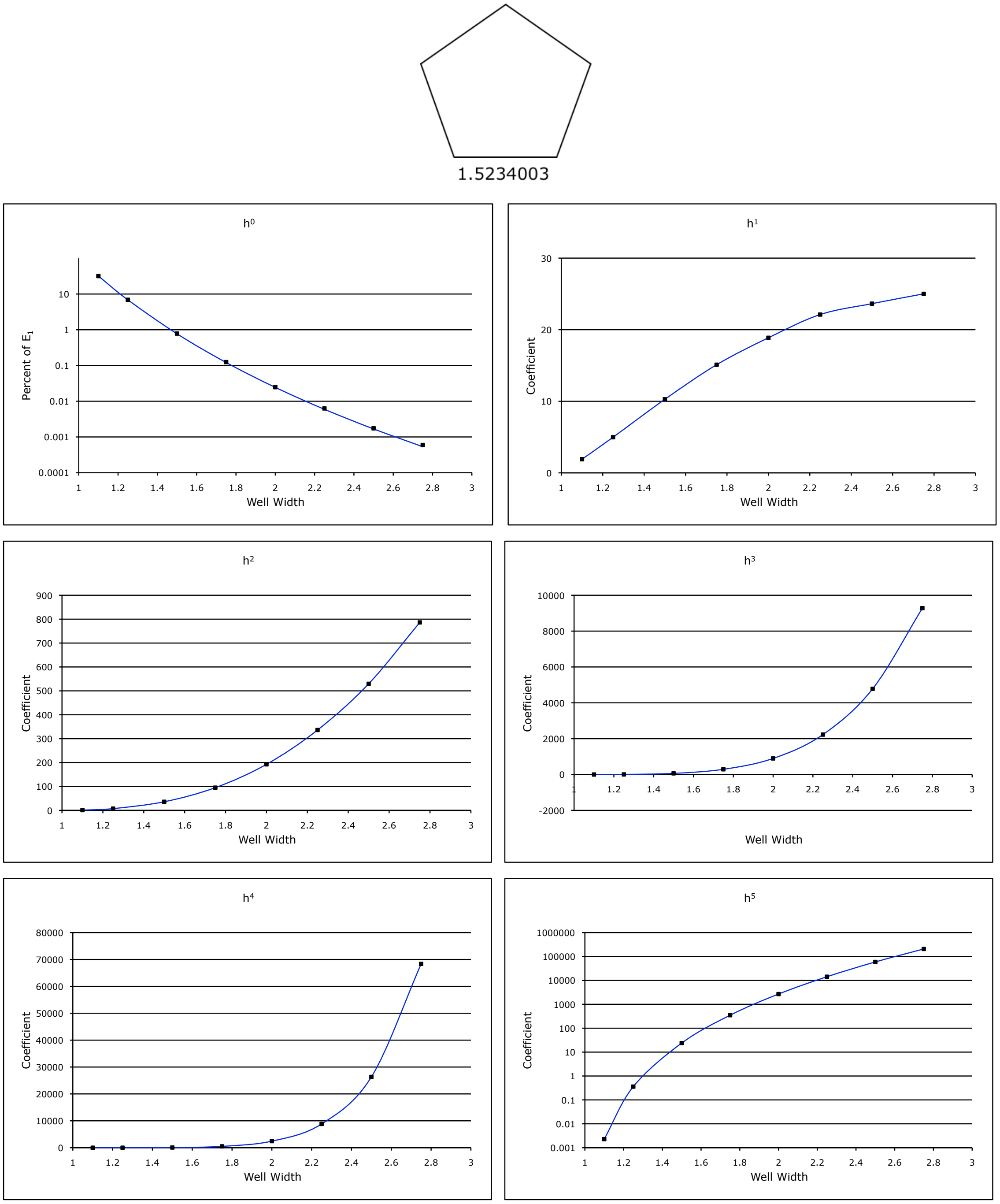

Figure 2.30 – Ratio integration results for $E_1(T)$ with diagram and coefficient (symbols as in 2.21).

2.8 COMPARISON TO OTHER TECHNIQUES

Both the virial equation of state and the square-well potential model have been of particular interest within the study of statistical mechanics. The virial equation of state represents a known solution, through cluster integrals, to thermodynamics without simplification or assumption, the challenge being the evaluation of those integrals. The square-well potential has been of interest as arguably the simplest pair potential to include an attractive component. Not surprisingly, there have been many attempts to calculate the virial coefficients for the square-well model, which have been summarized at the beginning of this chapter.

All solutions to cluster integrals above D_2 for the square-well potential have been some form of numerical integration. Most recently Singh used Mayer sampling (introduced in 2.1 and discussed in detail in chapter 4) to study the fourth, fifth and sixth virial coefficients of the square-well potential.

There are two major advantages to ratio integration over Mayer sampling for the case of the square-well potential. First, Mayer sampling only produces data at a specific values of h for each run. All temperatures in between those sampled must be interpolated. Each run is also specific to the well depth of the potential.

In the case of Mayer sampling for each temperature in the evaluation of the fourth virial coefficient runs of 10^9 samples took approximately 2 hours on a 2.66 GHz processor. For the fifth virial coefficient runs of 10^9 samples took 60 to 65 hours for each temperature.

Ratio integration, by contrast, took 25 minutes for 10^9 samples for the fourth virial coefficient and 20 hours for the fifth on a 1.67 GHz processor. In each run the coefficients of h for each integral are found, so virial coefficients for any well depth or any temperature can be calculated from the results of one run.

The second advantage of ratio integration over Mayer sampling is seen as the number of samples approaches infinity. Every Monte Carlo type sampling has some expected value that is being determined through high volume sampling. An increase of 100 fold typical results in an increase in accuracy of the expected value by one decimal place.

In ratio integration the expected values to be determined are the percentages of volume each possible integrand value takes up in the case of overlapping spheres. Because the sampling process is placing particles randomly in a box and tabulating how often each integrand value comes up, the accuracy can be increased indefinitely by taking more samples.

In Mayer sampling however, the value to be calculated is the complete virial coefficient for a specific temperature but this is done through free-energy perturbation techniques (equation 2.1.5). Even with an infinite number of samples, the integration will converge to some approximation of actual virial coefficient.

This gives ratio integration an advantage over one of the strongest thermodynamic predictors, Monte Carlo simulations. These simulations make random changes to a system, and then reject or accept them according to the probability of finding the system in that state. This essentially provides an ensemble-average by weighting each state’s contribution according to the number of times the simulation finds the system in that state. However, these simulations cannot handle the large number of particles in a macroscopic system. Instead the simulations converge to an approximation.

Comparison with Singh’s results shows good agreement with the features of all plots. Unfortunately numerical results for D(T) and E(T) are not presented, however further comparison between thermodynamic quantities derived from results will compared in the following chapter.

At infinite sampling Monte Carlo simulations also converge to approximate solutions. This is because of limits on the number of particles sampled. In Monte Carlo simulations 10^3 - 10^4 particles are sampled, with some approximation made to boundary conditions. An increase in particles sampled to more realistic magnitude is not possible despite advancements in processor speeds.

The most similar technique to ratio integration is the hit-and-miss Monte Carlo sampling used by Masters to evaluate Ree-Hoover diagrams (discussed in

2.1). The primary difference is that in Masters' approach the volume of the integral is also calculated for each sample and no data from the extensive work on hard spheres is utilized. Every "miss" in the simulation must therefore be accounted for, slowing the simulation. Also, no time saving integration techniques (such as the one explained for figure 2.10) may be taken advantage of.

Ratio integration could be applied to Ree-Hoover diagrams in the same fashion as used to evaluate the tradition cluster integrals. The drawback to this is that the e-bond is non-zero for distances greater than $\lambda\sigma$. So in the diagram:

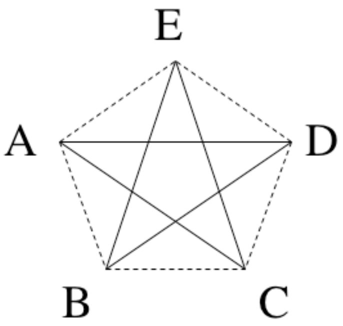

Figure 2.31 – A Ree-Hoover diagram contributing to E(T) (solid lines are f-bonds, dashed lines are e-bonds).

the distance AE can be as large as $2\lambda\sigma$. The volume available to particle D is then $4/3\pi(2\lambda\sigma)^3$. These diagrams are much slower than the ones in which A has an f-bond with all other particles. There are 3 out of 5 of these diagrams in the Ree-Hoover formalization and 4 out of 10 in the traditional representation. Evaluating the diagrams individually allows us to evaluate the accuracy of each diagram by comparing its value for h^0 to the expected one of $(\lambda\sigma)^{-2}$.

The advantage to Ree-Hoover diagrams is minimal for evaluation of the fifth virial coefficient using ratio integration, however they maybe useful in evaluation of the sixth in which the number of diagrams reduce from 56 to 23.

Comparison of Masters results for D(T) and E (T) with the ones presented in 2.4 - 2.7 show general agreement (Masters results for D(T) match those presented by Baxter and Monaghan):

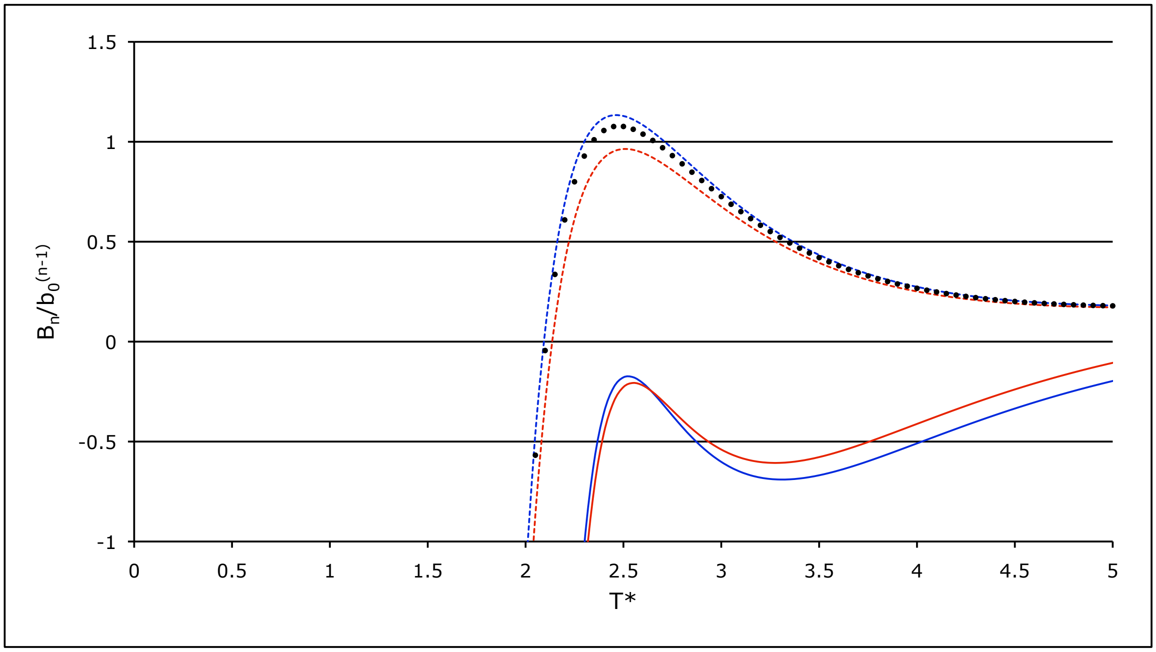

Figure 2.32 – Comparison of D(T) (solid lines) and E(T) (dashed lines) for ratio integration (blue), Masters (red), and Hussein (black).

In figure 2.32 the data from ratio integration is in blue and the data from Masters is in red. The coefficients are for $\lambda = 2$. D(T) is represented with a dashed line and E(T) with a solid line. Masters' values for D(T) match the results predicted by Baxter, however the more accurate results of Hussein are plotted as black dots and fit closer to the data presented here. The coefficients are plotted against the reduced temperature ($T^* = kT/\varepsilon$), where k is Boltzmann's constant and $-\varepsilon$ is the square-well depth.

As T* goes to infinity h goes to 0 and the virial coefficients for the square-well potential should go to the value for a hard sphere. For E(T) (in units reduced by b_0^4) this value is .11025217, the ratio integration goes exactly to this value by construction, however the results from Masters approach .11016211 which may explain the discrepancy in higher values of T*. As T* increases beyond values shown in the graph this discrepancy narrows.

2.9 WELL WIDTH EFFECTS ON VIRIAL COEFFICIENTS

If the temperature scale is given in reduced units ($T^* = kT/\varepsilon$), and the distance scale is in reduced units ($r^* = r/\sigma$) (including distance derived quantities, i.e. $V^* = V/\sigma^3$, $\rho^* = \rho/\sigma^3$), then the only parameter of interest is well width. Not surprisingly the well width has a dramatic effect on the virial coefficients and, through them, the thermodynamics of the system.

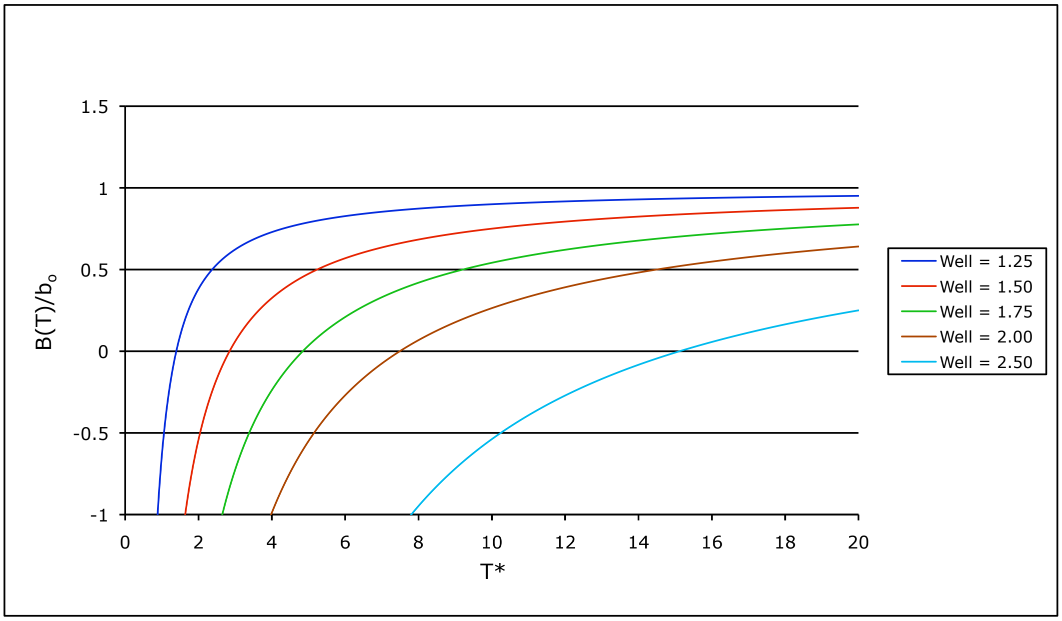

Figure 2.33 – B(T) values for the square well from ratio integration.

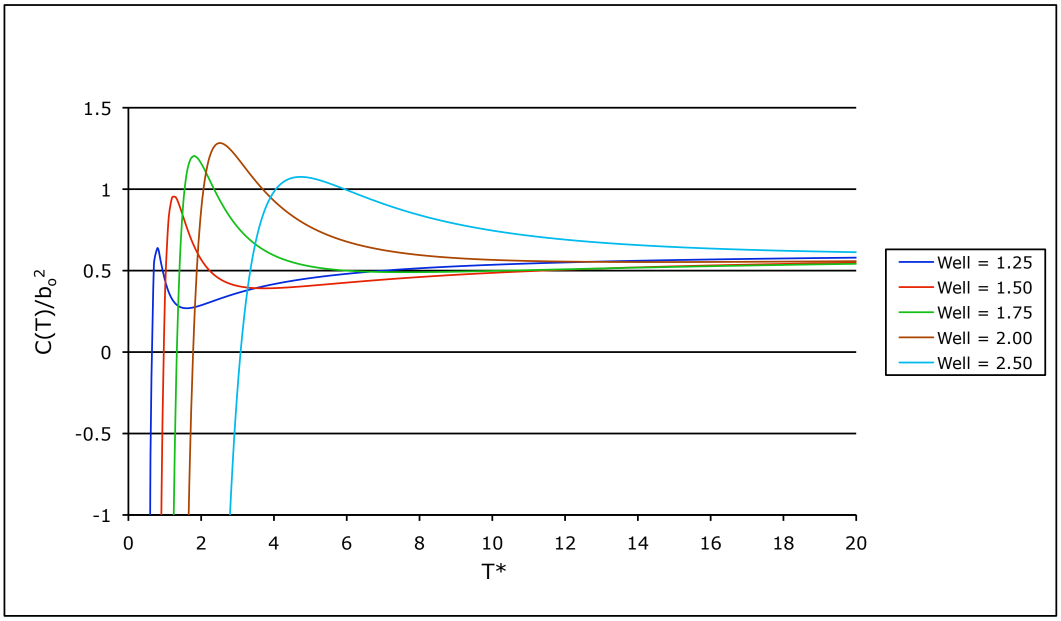

Figure 2.34 – C(T) values for the square well from ratio integration.

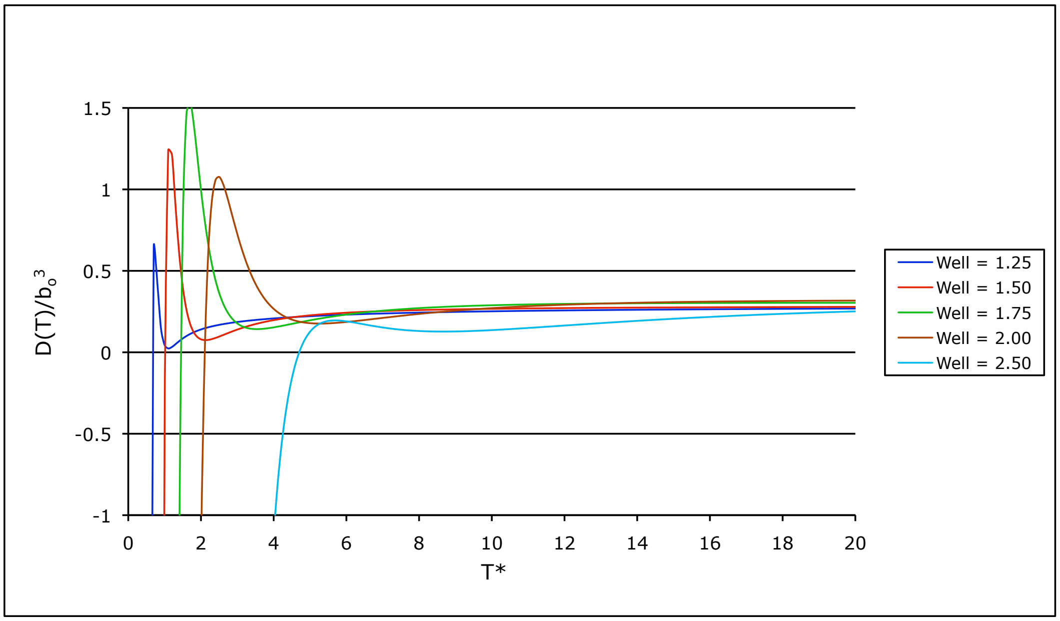

Figure 2.35 – D(T) values for the square well from ratio integration.

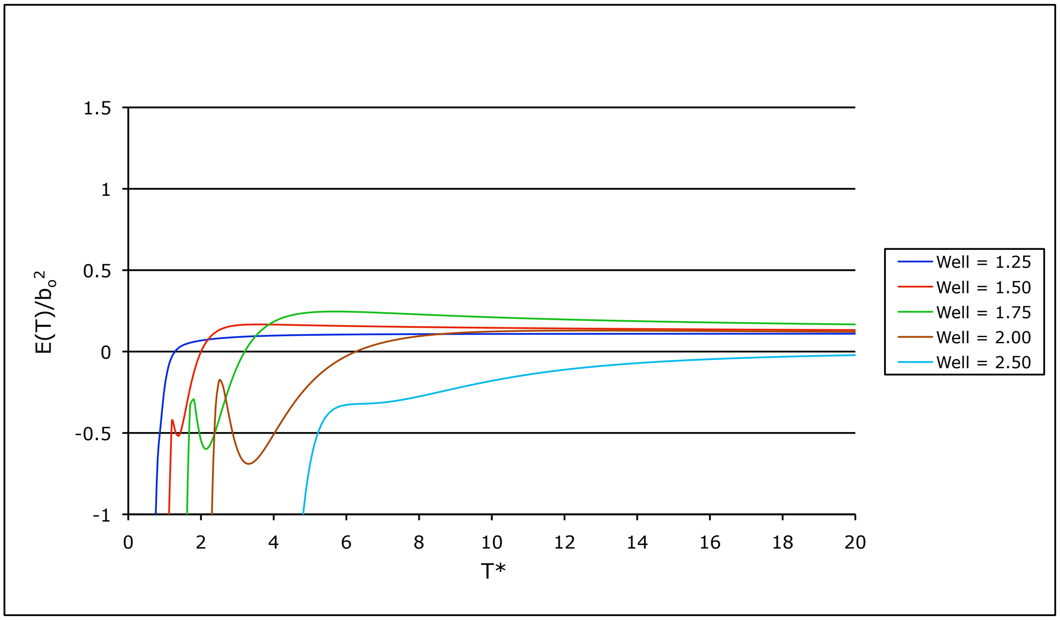

Figure 2.36 – E(T) values for the square well from ratio integration.

Chapter 2 References

[1] Katsura, S., 1958, *Phys. Rev.*, **115**, 1417.

[2] Barker, J. A., and Monaghan, J. J., 1962, *J. Chem. Phys.*, **36**, 2558.

[3] Ree, F. H., Hoover, W. G., 1964, *J. Chem. Phys.*, **40**, 939.

[4] Vlasov, A. Y., You, X. M., Masters, A. J., 2002, *Mol. Phys.*, **100**, 3313.

[5] Sevick, E. M., Monson, P. A., 1991, *J. Chem. Phys.*, **94**, 3070.

[6] Hussein, N. A. R., Ahmed, S. M., 1991, *J. Phys. A: Math. Gen.*, **24**, 289.

[7] Naresh, D. J., Singh, J. K., 2009, *Fluid Phase Equilib.*, **279**, 47.

[8] Singh, J. K., Kofke, D. A., 2004, *Phys. Rev. Lett.*, **92**, 220601-1.

[9] Kratky, K. W., 1976, *Physica A*, **85**, 607.

Chapter 3
Applications

3.1 MAXWELL CONSTRUCTION

The virial expansion represents a complete solution to the thermodynamics of the system it describes. The question becomes how does one calculate quantities of interest from the virial expansion.

A phase diagram displays the equilibrium coexistence lines of different phases as a function of thermodynamic properties (pressure, temperature, etc.). The coexistence curves can be calculated using the Maxwell construction method.

In a Maxwell construction isotherms are plotted in the pressure/volume plane. For the van der Waals equation of state:

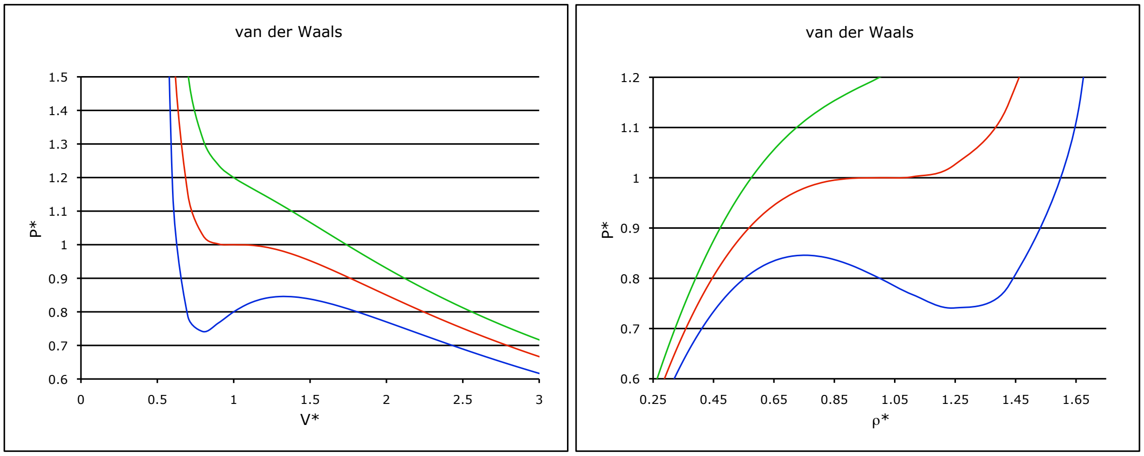

Figure 3.1 – Isotherms for the van der Waal fluid at subcritical (blue), critical (red), and supercritical (green) temperatures.

In figure 3.1 $P^* = P/P_c$, $V^* = V/V_c$ and $\rho^* = \rho/\rho_c$ (where P is the pressure, V is the molar volume and ρ is the molar number density; and the subscript c denotes the value at the critical point). In the figure the blue line is a subcritical isotherm, the red is the isotherm at the critical temperature, and the green is a supercritical isotherm.

Subcritical isotherms have a portion of their graph that has a positive slope when plotted against volume ($\partial P/\partial V > 0$) or negative when plotted against density ($\partial P/\partial \rho < 0$). From the definition of isothermal compressibility:

$$\chi_T = -\frac{1}{V}\left(\frac{\partial V}{\partial P}\right)_T \tag{3.1.1}$$

and since volume must be positive, ($\partial P/\partial V > 0$) results in a negative compressibility, which is unstable.

James Clerk Maxwell[1] corrected for this by replacing a portion of the isotherm with a flat line. The endpoints of which correspond to points on the coexistence curve. The area above the isotherm and below the line must be equal to the area below the isotherm and above the line in the pressure/volume plane.

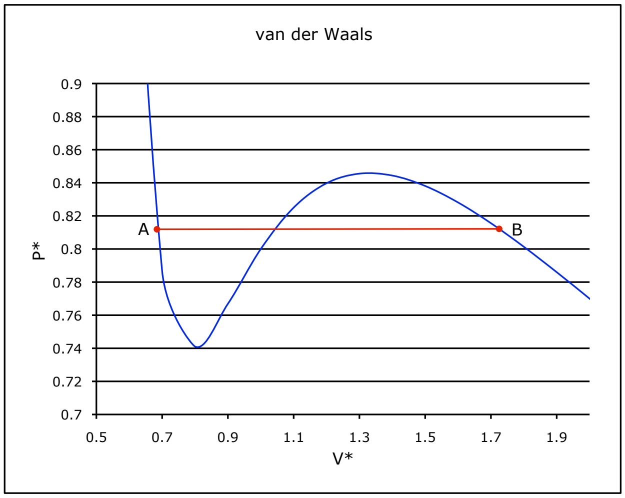

Figure 3.2 – An isotherm for the van der Waal fluid with coexistence points A and B predicted by Maxwell construction.

The Maxwell equal-area construction ensures that the pressure and chemical potential are equal for the liquid and vapor phases. We label the endpoints of the line ‘a’ and ‘b’; and will refer to the area under the line as area 1 and the area above as area 2.

We can see from figure 3.3 that the area of the rectangle ‘a’ and ‘b’ form with the volume axis must be the same as the area under the curve plus area 1 minus area 2. Since area 1 = area 2 we then have:

$$(V_b - V_a)\ P(V_a) = \int_{V_a}^{V_b} P(V)dV \tag{3.1.2}$$

And by definition:

$$(\partial A = -P\partial V)_T \tag{3.1.3}$$

where A is the molar Helmholtz free energy. Since we are evaluating an isotherm (3.1.3) gives us:

$$A_b - A_a = -\int_{V_a}^{V_b} P(V)dv \tag{3.1.4}$$

Combining (3.1.4) with (3.1.2) and noting that $P(V_a) = P(V_b)$, which will now be referred to simply as P :

$$A_b + PV_b = A_a + PV_a \tag{3.1.5}$$

And from the definition of molar Gibbs free energy:

$$G = A + PV \tag{3.1.6}$$

Since the molar Gibbs free energy is the molar chemical potential for a pure substance:

$$\mu_a = \mu_b \quad \text{and} \quad P_a = P_b \tag{3.1.7}$$

3.1.7 is the requirement for phase coexistence.

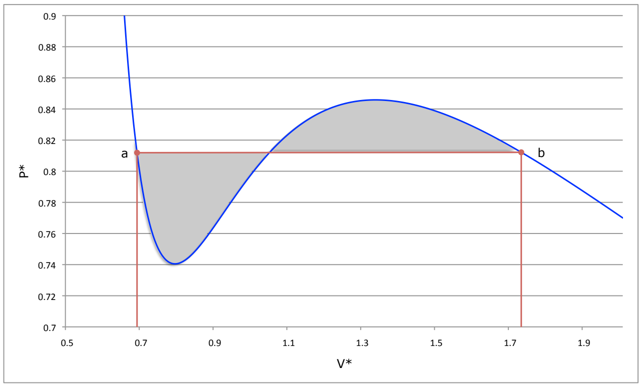

Figure 3.3 – An isotherm for the van der Waal fluid with coexistence points a and b predicted by Maxwell construction with the equal area loops shown.

The isotherms are constructed from the virial equation with the indicated number of coefficients. For the virial equation up to E(T) this is:

$$\beta P = \rho + B(T)\rho^2 + C(T)\rho^3 + D(T)\rho^4 + E(T)\rho^5 \quad (3.1.8)$$

First the lowest density with a pressure common to some higher density (ρ_0) is found.

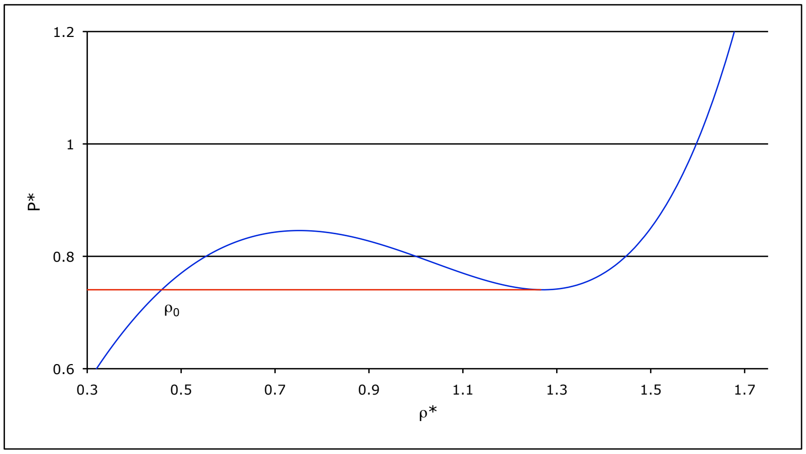

Figure 3.4 – The lowest density whose pressure is found at a higher density.

Densities above ρ_0 are tested for Maxwell's equal area law. The density is increased incrementally a small density step. From the lower density (ρ_1) a density with the same pressure and a positive slope is found (ρ_2).

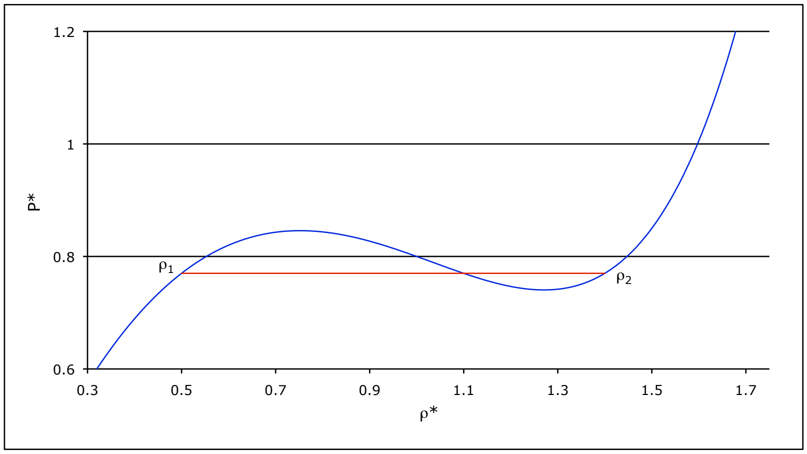

Figure 3.5 - A higher density is chosen by matching pressure of ρ_1.

The area of the rectangle and the area under the curve can be calculated analytically from the virial equation of state. The area is calculated for the isotherm plotted in the pressure/volume plane where the volume is simply $1/\rho$. Incrementally increasing the density rather than the volume has advantages that will be shown later in this section. The coexistence curves are also plotted against the density, making density the better choice.

The area of the rectangle is given by:

$$A_R = P\ (1/\rho_1 - 1/\rho_2) \tag{3.1.9}$$

Where P is the pressure given by ρ_1 and ρ_2, and remembering that ρ_1 corresponds to the larger volume.

The area under the curve is given by:

$$A_C = \int_{\frac{1}{\rho_2}}^{\frac{1}{\rho_1}} \frac{1}{V} + \frac{B(T)}{V^2} + \frac{C(T)}{V^3} + \frac{D(T)}{V^4} + \frac{E(T)}{V^5} dV$$

$$A_C = ln(V) - \frac{B(T)}{V} - 2\frac{C(T)}{V^2} - 3\frac{D(T)}{V^3} - 4\frac{E(T)}{V^4}\Bigg|_{\frac{1}{\rho_2}}^{\frac{1}{\rho_1}} \tag{3.1.10}$$

At low temperatures the volume curve flattens out making the determination of volume given a pressure difficult.

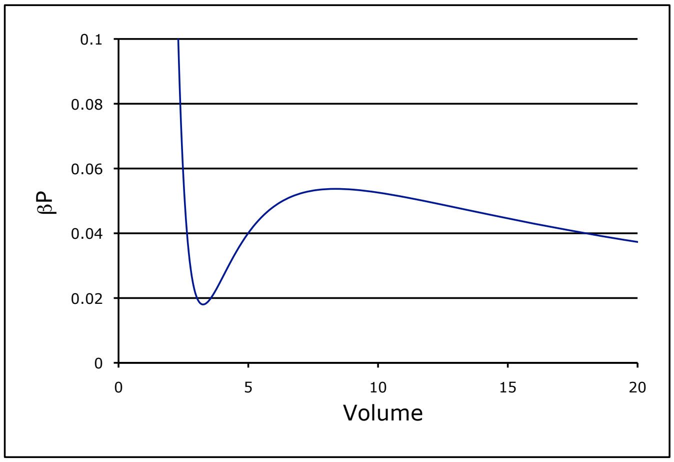

Figure 3.6 – Low temperature isotherm in the pressure-volume plane.

This problem is avoided by choosing the density scale to increment along. The isotherms in figures 3.6 and 3.7 are both from the virial equation of state up to D(T) at T*= 2.43.

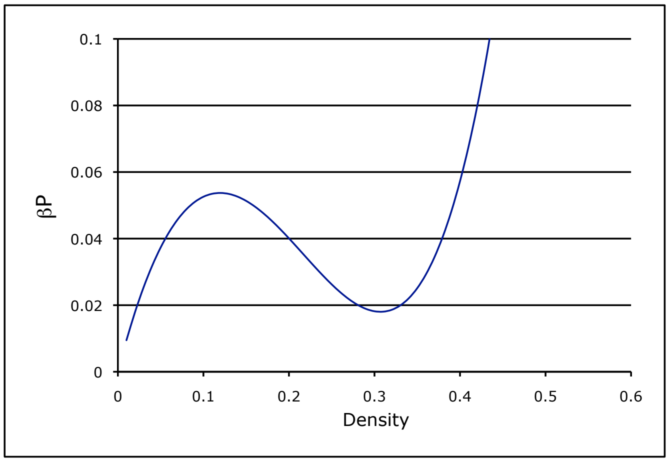

Figure 3.7 – Low temperature isotherm in the pressure-density plane.

Another solution can be calculated from the chemical potential. The chemical potential is given from (1.4.22) or in terms of the virial coefficients:

$$\beta\mu = \ln(\Lambda^3\rho) + 2B(T)\rho + \frac{3}{2}C(T)\rho^2 + \frac{4}{3}D(T)\rho^3 + \frac{5}{4}E(T)\rho^4 \quad (3.1.11)$$

The factor Λ^3 is constant at all densities for each isotherm and because:

$$\ln(\Lambda^3\rho) = \ln\Lambda^3 + \ln\rho \quad (3.1.12)$$

the term ln(Λ^3) can be considered an arbitrary constant.

From (3.1.8) we can calculate the pressure and from (3.1.11) the chemical potential. Recall from (3.1.7) that the conditions for coexistence are equal chemical potentials and pressures in the two states, so graphing chemical potential against pressure:

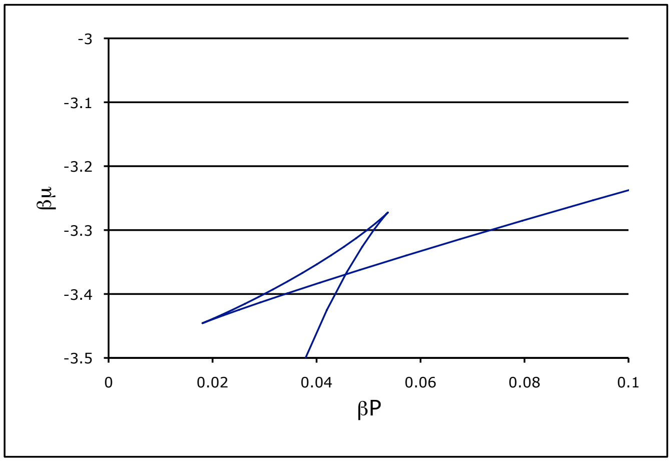

Figure 3.8 – Low temperature isotherm plotted as chemical potential vs. pressure.

In figure 3.8 the intersection at (.046, -3.37) corresponds to the pressure and chemical potential at equilibrium, this point is calculated from (3.1.8) and (3.1.11) for two densities (the liquid and the vapor).

Calculating the coexistence curve from figure 3.8 rather than figure 3.6 can be numerically more convenient at some temperatures, but is not strictly necessary, nor does it guarantee greater accuracy. Solving the equation of state allows one to determine coexistence curves, from it, with arbitrary precision.

3.2 PHASE DIAGRAMS

A reference system is chosen from the literature with values λ = 1.85 and ε/k = 69.4 K. At each well width the square-well depth is chosen to keep B(T) constant at the critical temperature of the reference system (151 K). From 1.7.15, the depth of a potential with a well width of λ, is given by:

$$\varepsilon/k = 151\ln\left(\frac{(e^{69.4/151}-1)(1.85^3-1)}{\lambda^3-1}+1\right) \qquad (3.2.1)$$

For each temperature, the pressure is calculated at some small density. The density is then increased until a density is reached with a pressure that. The area in the rectangle in section 3.1 is then given by:

Applying the Maxwell construction to the results from section 3.2 produces coexistence curves for the virial equation of state. First we construct a diagram with increasing virial order from literature values for λσ = 2. Using (1.7.15) for B(T), (2.2.1) for C(T), Katsura's result for D(T) and Masters result for E(T).

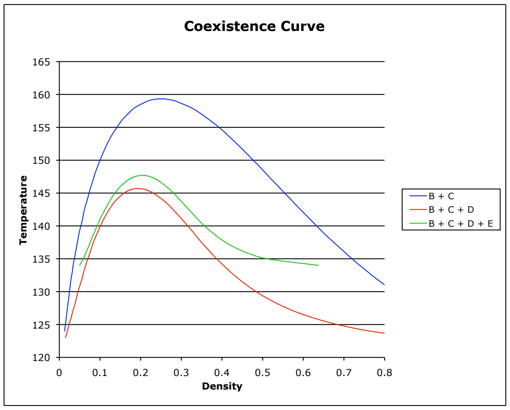

Figure 3.9 – Liquid-vapor coexistence for truncated virial expansion using a Maxwell construction.

The accuracy of the virial equation of state used to calculate the coexistence curves can be increased by including terms from the Carnahan Starling equation of state for hard spheres (defined below). Introducing the packing fraction:

$$\eta = \frac{\pi \rho d^3}{6} \tag{3.2.2}$$

In (3.2.2) d is the hard sphere diameter, which is chosen to be unity by convention. From calculated values in the literature, the virial equation for a hard sphere potential is:

$$\frac{\beta P}{\rho} = 1 + 4\eta + 10\eta^2 + 18.365\eta^3 + 28.225\eta^4 + 39.74\eta^5 + \ldots \tag{3.2.3}$$

Carnahan and Starling approximated the virial equation for hard spheres with:

$$\frac{\beta P}{\rho} = 1 + \sum_{i=1}^{\infty} (i^2 + 3i)\eta^i \tag{3.2.4}$$

which gives:

$$\frac{\beta P}{\rho} = 1 + 4\eta + 10\eta^2 + 18\eta^3 + 28\eta^4 + 40\eta^5 + \ldots \tag{3.2.5}$$

Equation (3.2.4) can be expressed as:

$$\frac{\beta P}{\rho} = \frac{1 + \eta + \eta^2 - \eta^3}{(1 - \eta)^3} \tag{3.2.6}$$

The Carnahan Starling equation of state fits computer simulation data very well. The accuracy and simplicity of (3.2.6) makes it a very popular approximation. The Carnahan Starling equation can be used to supplement our virial equation of state, and provide an approximation for the repulsive part of the potential at higher order coefficients.

For a virial equation up to the fourth coefficient (D) the assumption is the equation of state is:

$$\frac{\beta P}{\rho} = 1 + B(T)\rho + C(T)\rho^2 + D(T)\rho^4 + \sum_{i=5}^{\infty} B_{i+1}(T)\rho^i \tag{3.2.7}$$

where the summation is unknown. If the summation is assumed to be coefficients described by the Carnahan Starling equation of state then (3.2.7) becomes:

$$\frac{\beta P}{\rho} = 1 + \Delta B(T)\rho + \Delta C(T)\rho^2 + \Delta D(T)\rho^4 + \frac{1+\eta+\eta^2-\eta^3}{(1-\eta)^3} \qquad (3.2.8)$$

In (3.2.8) the Δ in front of a coefficient indicates it is the difference between the calculated value and the value corresponding to the hard sphere. This is to compensate for over counting the coefficients calculated for the square-well. For example:

$$\Delta B(T)\rho = B(T)\rho - 4\eta \qquad (3.2.9)$$

When the equation of state is described by (3.2.8) there is significant improvement in the phase diagrams for lower ordered equations of state and smaller adjustments in higher ordered equation of states.

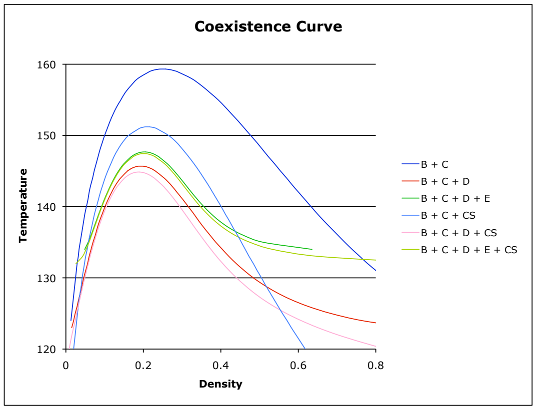

Figure 3.10 – Coexistence curves with truncated virial expansions extended by the Carnahan Starling equation of state.

Inclusion of higher ordered terms in the virial equation of state alternates between increasing and decreasing the critical point, each refinement making a smaller adjustment than the one before. This is due to the large cancellations amongst the virial coefficients in the equation of state. Indeed, the critical point is characterized by:

$$\left(\frac{\partial P}{\partial \rho}\right)_{T=T_c} = 0 \qquad \left(\frac{\partial^2 P}{\partial \rho^2}\right)_{T=T_c} = 0 \qquad (3.2.10)$$

Masters' results for D(T) agrees with Katsura's for a well width of 2.0; however when the more accurate results of Hussein are combined with Masters' results for E(T) the resulting phase diagram shows good agreement with the results from ratio integration.

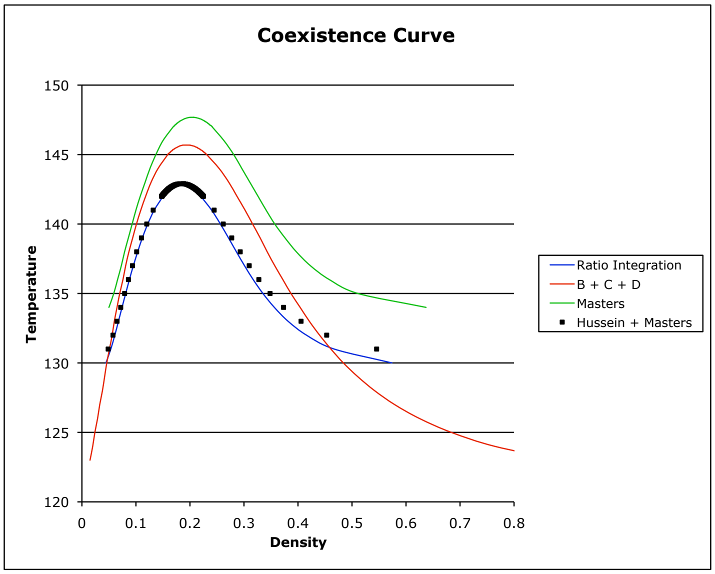

Figure 3.11 – Comparison of coexistence curves between truncated virial expansions with different methods for virial coefficient calculation.

The results for the four difference choices of equations of state at 5 different well widths are graphed in figures 3.12 – 15.

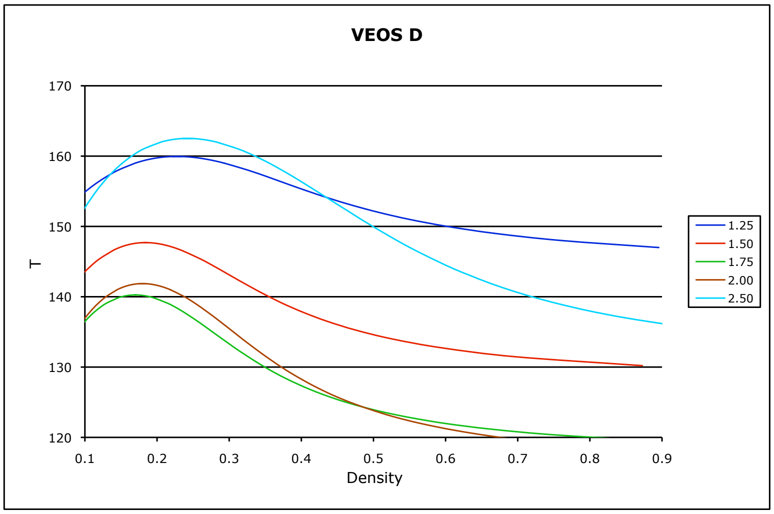

Figure 3.12 – Coexistence curves predicted by a virial expansion truncated at D(T) for different square well widths.

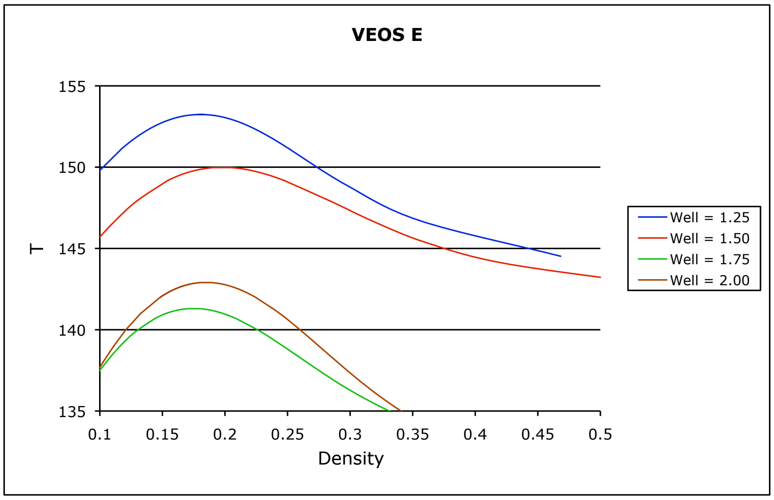

Figure 3.13 - Coexistence curves predicted by a virial expansion truncated at E(T) for different square well widths.

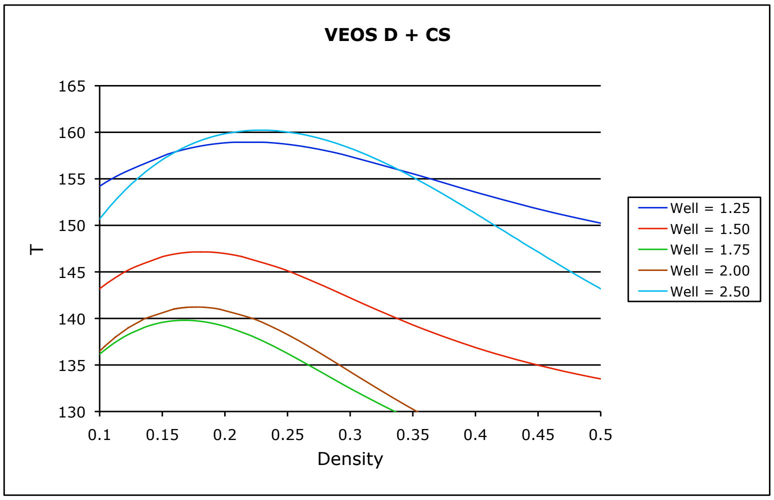

Figure 3.14 - Coexistence curves predicted by a virial expansion truncated at D(T) with the Carnahan Starling equation of state values for higher order coefficients for different square well widths.

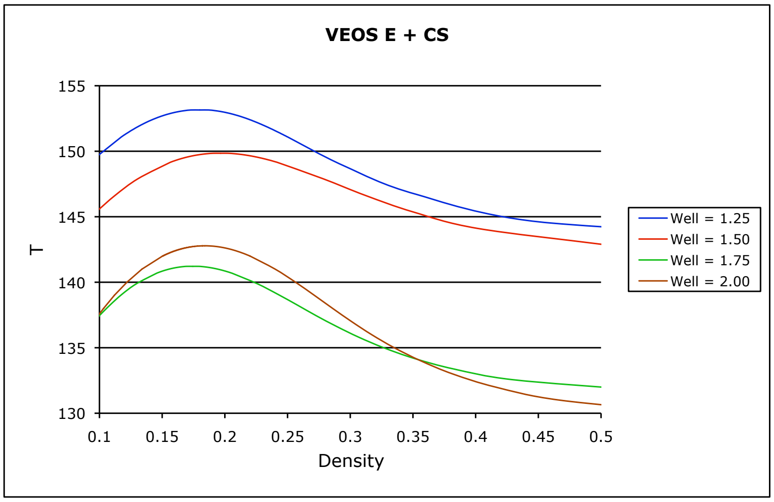

Figure 3.15 - Coexistence curves predicted by a virial expansion truncated at E(T) with the Carnahan Starling equation of state values for higher order coefficients for different square well widths.

In figures 3.16 – 20 the results are graphed grouped by well width.

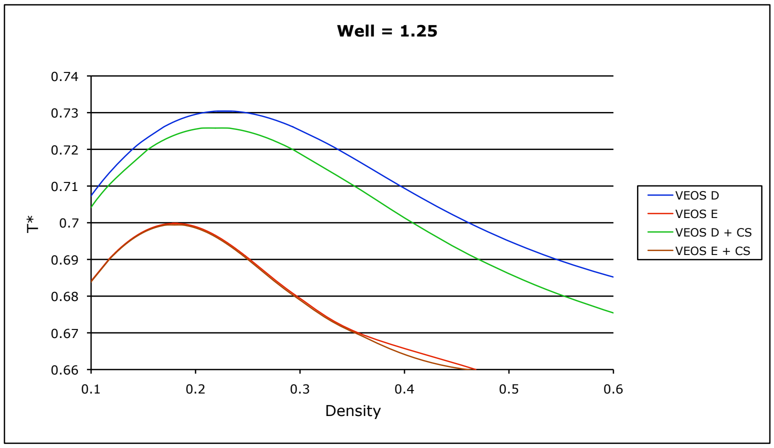

Figure 3.16 – Comparison of coexistence curves predicted by different virial expansions for the square well model with a well width of 1.25.

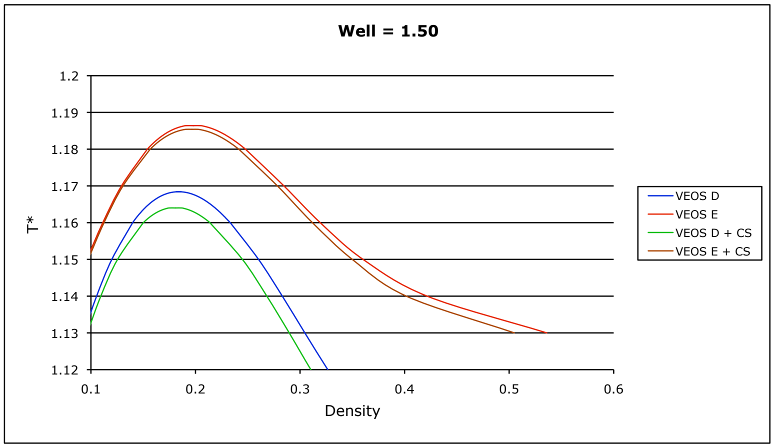

Figure 3.17 - Comparison of coexistence curves predicted by different virial expansions for the square well model with a well width of 1.50.

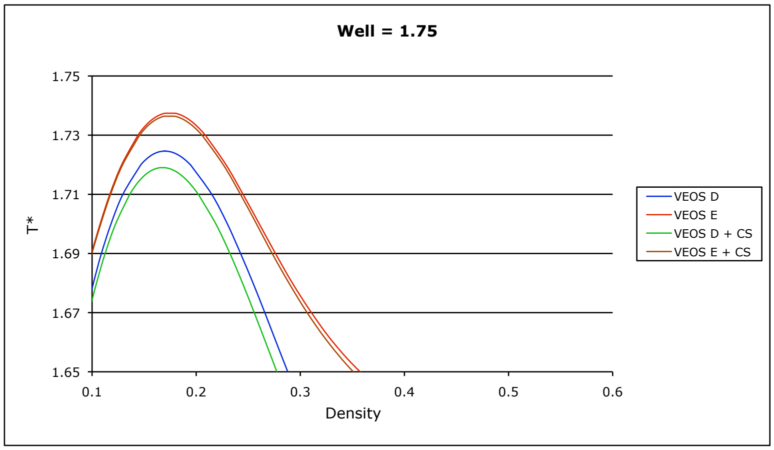

Figure 3.18 - Comparison of coexistence curves predicted by different virial expansions for the square well model with a well width of 1.75.

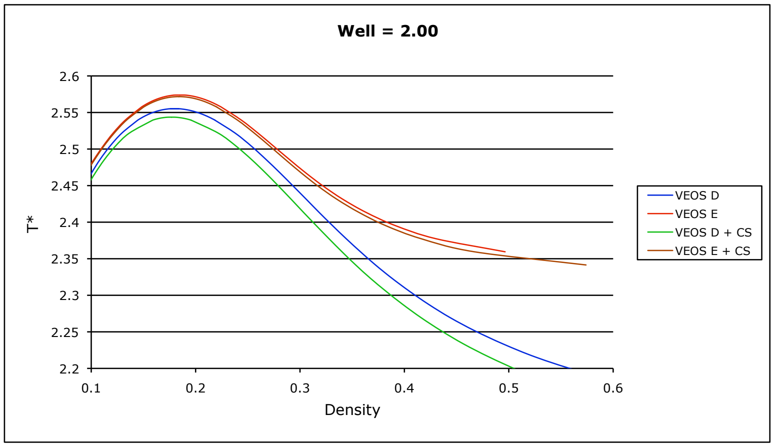

Figure 3.19 - Comparison of coexistence curves predicted by different virial expansions for the square well model with a well width of 2.00.

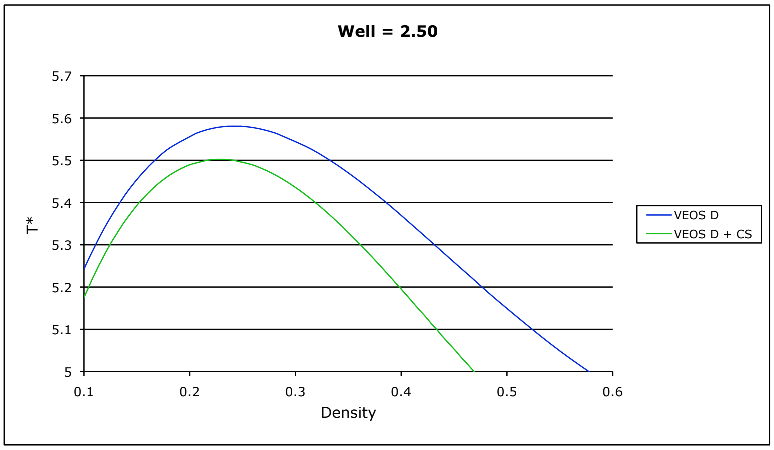

Figure 3.20 - Comparison of coexistence curves predicted by different virial expansions for the square well model with a well width of 2.50.

Coexistence data for the well width of 2.5 could not be calculated for the virial equations of state (VEOS) up to E(T) with or without the Carnahan Starling adjustment. These VEOS predict a negative pressure at low densities that is never positive (see Figure 3.21), and hence has no first loop. Higher ordered virial coefficients may be necessary to calculate coexistence data.

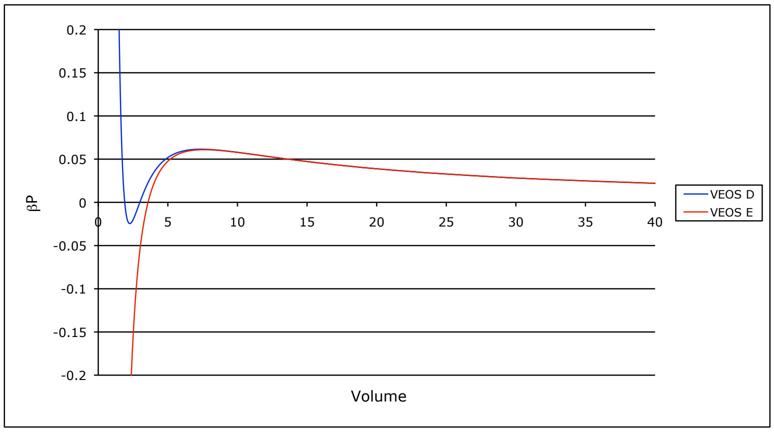

Figure 3.21 – No coexistence data can be determined if there is no loop.

3.3 THERMODYNAMICS FROM THE VIRIAL EXPANSION

The greatest shortcoming of the truncated virial expansion is seen at high densities, where higher ordered virial terms become nontrivial. This greatly affects the accuracy of the phase diagram, since the construction of coexistence curves is accomplished by ensuring that the pressure and chemical potential at high (liquid) and low (gaseous) densities are equal. Therefore, the low-density coexistence data can be off even if the pressure predictions for low density are near exact.

Despite the virial expansions failure to accurately predict coexistence curves this work would be incomplete without them because of their prevalence as a comparison and test for analytical and numeric approximations. Although this failure may seem alarming, it is important to ask why the coexistence curve is chosen as the comparison of choice for different theories.

A complete solution to the thermodynamics of a system should be able to predict free energy, chemical potential and one of pressure, density or temperature given the other two as well as other thermodynamic quantities. In fact the power of the solution is overwhelming, and an infinite number of isotherms, isobars or isochores could be generated to compare with simulations or experimental data. Generating a coexistence curve is a good way to test multiple densities, pressures and temperatures while predicting a physically significant quantity. For this reason phase diagrams are included in nearly all thermodynamic approximations.

It should be noted, however, that the accuracy can be equally important in regions of the phase diagram where "nothing is happening", as in regions where changes of phase do not occur since many practical experimental and engineering applications involve purely gaseous states.

A simple yet perfect illustration of this is the square well model for argon. Hirschfelder[2] has presented a method for approximating potentials with a square well model by fitting the second virial coefficient to experimental data. For argon the square well parameters are $\varepsilon/k = 69.4$ K, $\lambda = 1.85$, and $\sigma = 3.162$ Å.

The first two virial coefficients are calculated using (1.7.15) and (1.8.32) respectively. Using ratio integration the fourth and fifth virial coefficients are calculated for a well width of 1.85 as functions of temperature:

$$\frac{D(T)}{b_o^3} = 0.2869 + 1.062h - 12.10h^2 + 18.36h^3 + 38.67h^4 - 37.25h^5 - 12.73h^6 \tag{3.3.1}$$

$$\frac{E(T)}{b_o^4} = 0.1103 + 1.274h - 7.132h^2 + 43.97h^3 - 269.7h^4 + 352.5h^5 + 227.3h^6 - 376.8h^7 - 77.2h^8 - 6.942h^9 - 0.2362h^{10}$$

(3.3.2)

Isotherms are then produced using the truncated virial expansion up to E(T) and compared to experimental data for argon[3]. In figure 3.22 the temperature is sub-critical and the virial expansions do a poor job above the coexistence density. As the temperature rises above the critical temperature the virial expansion quickly improves to match experimental data. At room temperature (295 K) the virial expansion up to D(T) and E(T) each produce values that deviate from experiments by less than .1% over the entire region.

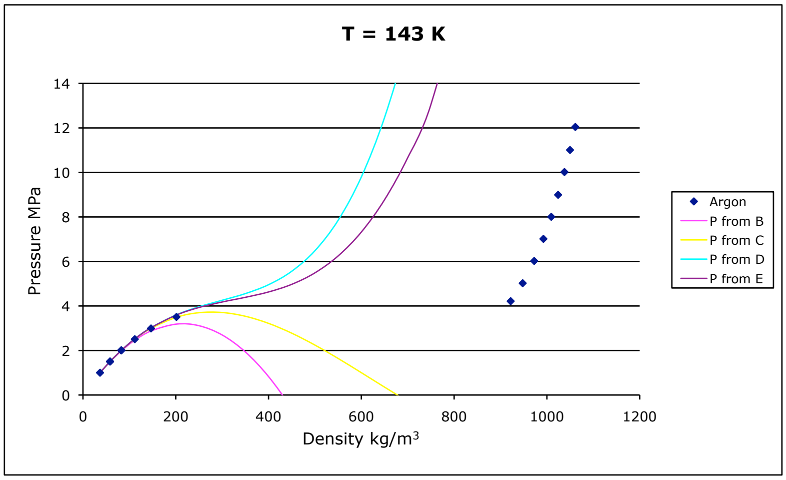

Figure 3.22 – Experimental pressures for argon and pressures predicted by truncated virial expansions at 143 K.

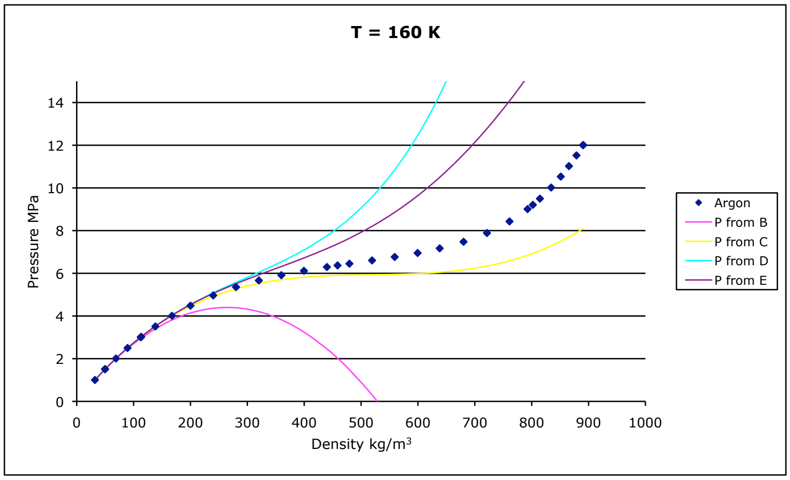

Figure 3.23 – Experimental pressures for argon and pressures predicted by truncated virial expansions at 160 K.

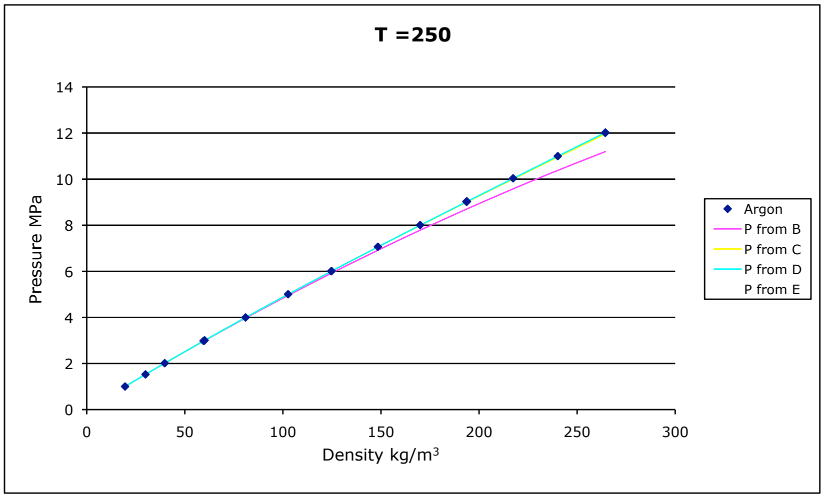

Figure 3.24 – Experimental pressures for argon and pressures predicted by truncated virial expansions at 250 K.

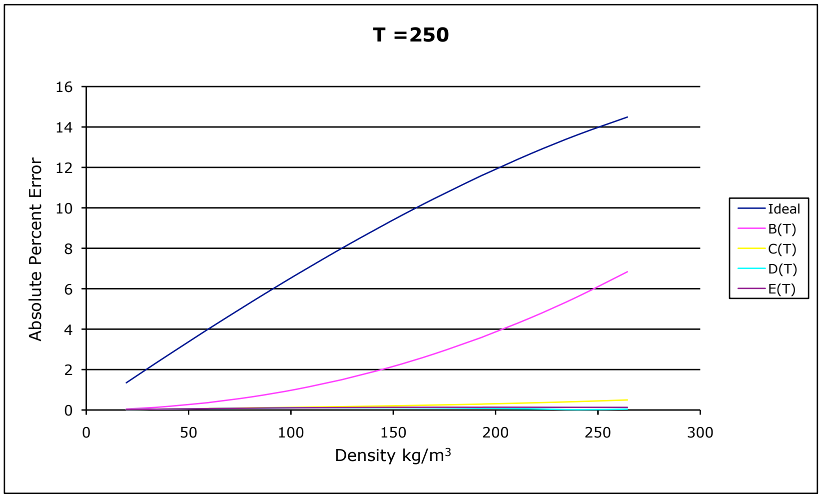

Figure 3.25 – Absolute percent error between experimental data for argon and that predicted by the ideal gas law and the truncated virial expansions at 250 K.

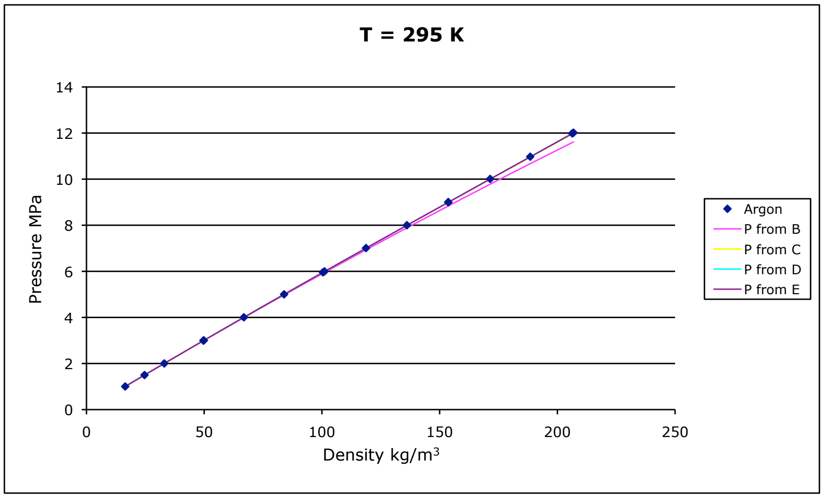

Figure 3.26 – Experimental pressures for argon and pressures predicted by truncated virial expansions at 295 K.

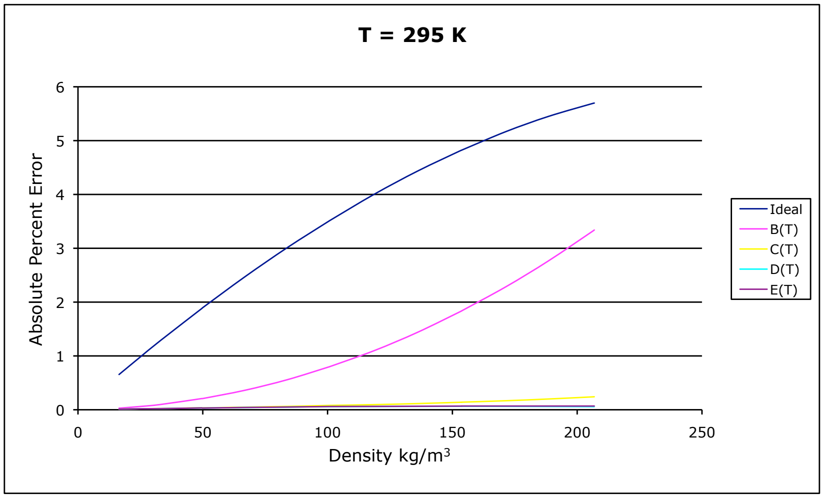

Figure 3.27 – Absolute percent error between experimental data for argon and that predicted by the ideal gas law and the truncated virial expansions at 295 K.

It has been claimed that the square-well potential is an inaccurate model for predicting second virial coefficients of argon[4]. The authors test its accuracy with a technique suggested by Michels et al.[5] in which available experimental data[6] is used to create a graph of b_o $(2\pi\sigma^3/3)$ vs. reduced well depth (ε/k_b) for a given well width using:

$$b_o = \frac{B(T)_{exp}}{1-(\lambda^3-1)(e^{\varepsilon/kT}-1)} \tag{3.3.3}$$

Then the true value for ε/k_b should be given by the intersection of the plots, but the authors show that this is not the case by giving a plot similar to figure 3.28. The authors then suggest that changing λ and ε may improve performance, but fault this approach with having two adjustable parameters. They fail to acknowledge that only λ needs to be changed and ε can be determined with the method they chose to test the square well potential. They also use $\lambda = 1.5$ in their figure instead of the well used value from Hirschfelder of 1.85.

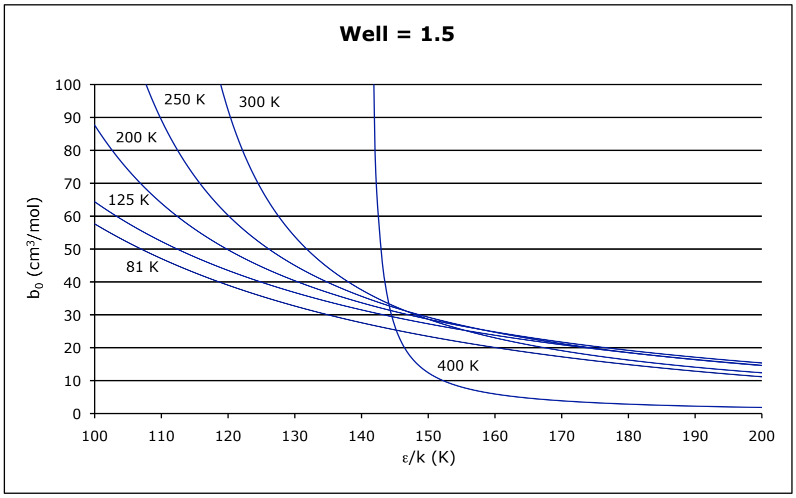

3.28 – Predicted values of b_o from ε/k and experimental argon data for a well width of 1.5.

Using $\lambda = 1.85$ the plot is much closer to converging and seems to confirm the value of $\varepsilon/k = 69.4$ K and $\sigma = 3.162$ Å as shown in figure 3.29. Remarkably when $\lambda = 1.66$ is plotted the predicted b_o converge for $\varepsilon/k = 101.5$ (figure 3.30). This is even more impressive when all the data from [6] are plotted (figure 3.31).

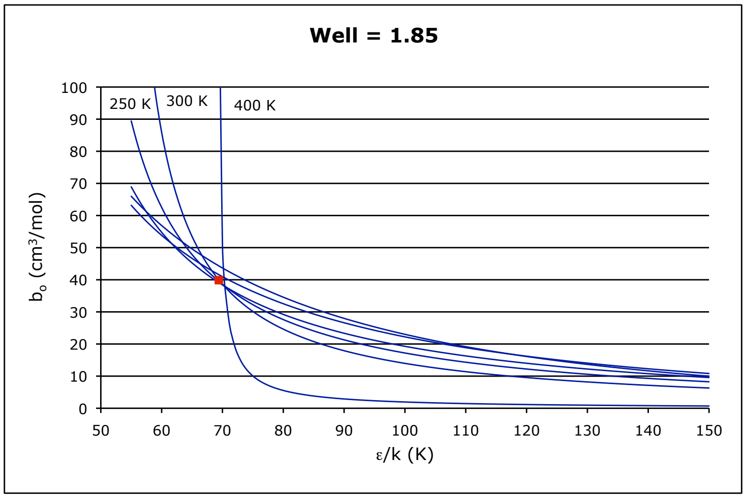

3.29 – Predicted values of b_o from ε/k and experimental argon data for a well width of 1.85. A red square marks the value of $\varepsilon/k = 69.4$ K and $\sigma = 3.162$ Å.

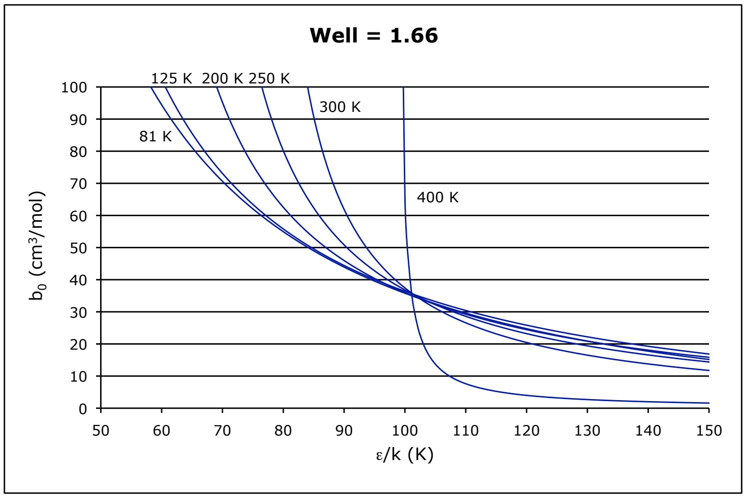

3.30 - Predicted values of b_o from ε/k and experimental argon data for a well width of 1.66.

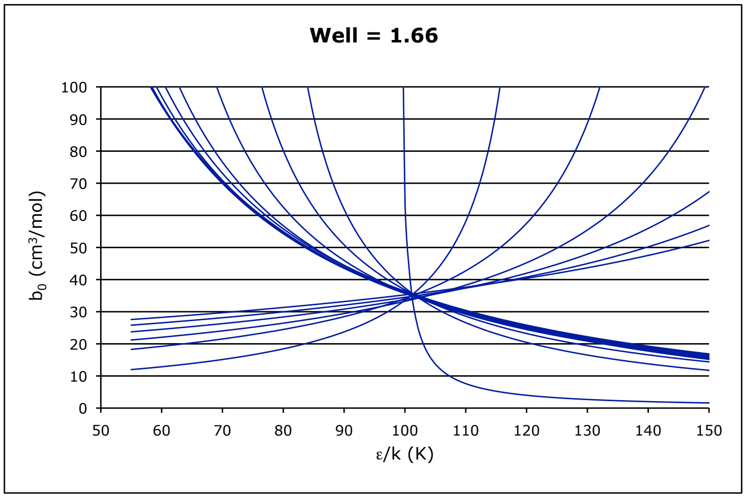

3.31 - Predicted values of b_o from ε/k and experimental argon data for a well width of 1.85 at all available temperatures.

A well width of 1.66 and ε/k = 101.5 K also gives better agreement with experimental data for argon, as shown in figures 3.32-3.34.

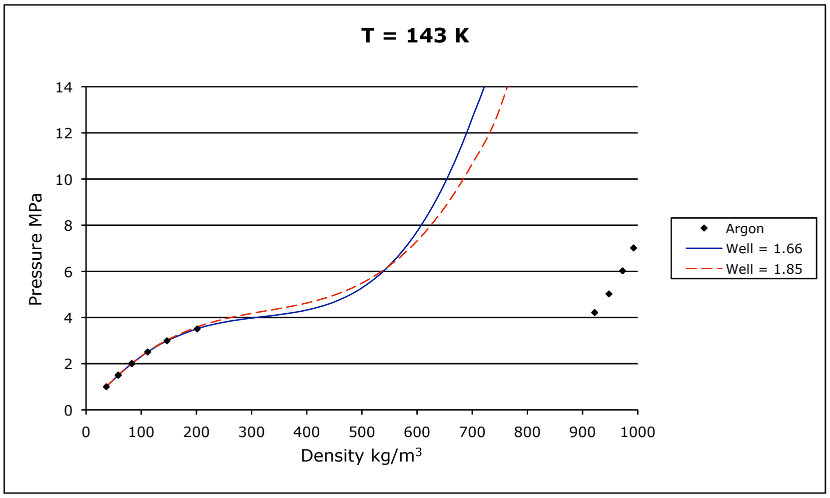

Figure 3.32 – Pressure vs. Density for the truncated virial equation up to E(T) using the values of Hirschfelder (well = 1.85) and the ones derived above (well = 1.66).

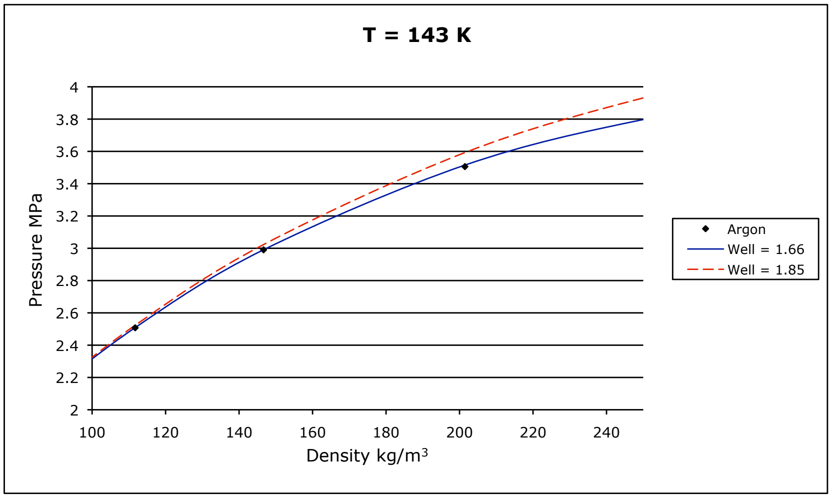

Figure 3.33 – Pressure vs. Density for the truncated virial equation up to E(T) using the values of Hirschfelder (well = 1.85) and the ones derived above (well = 1.66).

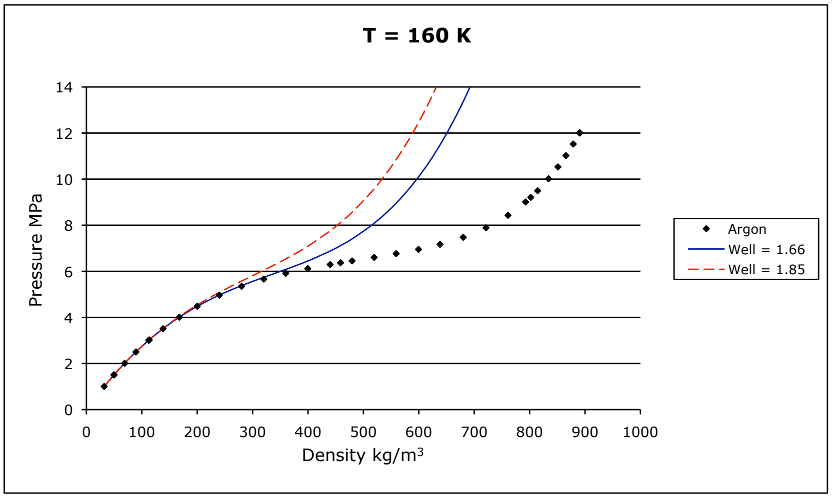

Figure 3.34 – Pressure vs. Density for the truncated virial equation up to D(T) using the values of Hirschfelder (well = 1.85) and the ones derived above (well = 1.66).

It can be difficult to choose parameters to fit the square well potential to second virial data because there are three adjustable parameters. This means vastly different numbers for each can fit the data well. Hirschfelder overcomes this by making an assumption about the size of hard-care diameter. But this can be overcome, as shown above, by graphing b_o against ε/k. Both, by design, show good agreement with experimental values of B(T) (figure 3.35). Hirschfelder's choice shows better agreement with experimentally[7] determined values for C(T) (figure 3.36). However the values obtained by plotting b_o against ε/k describe the thermodynamics of the system better (figures 3.32-3.34).

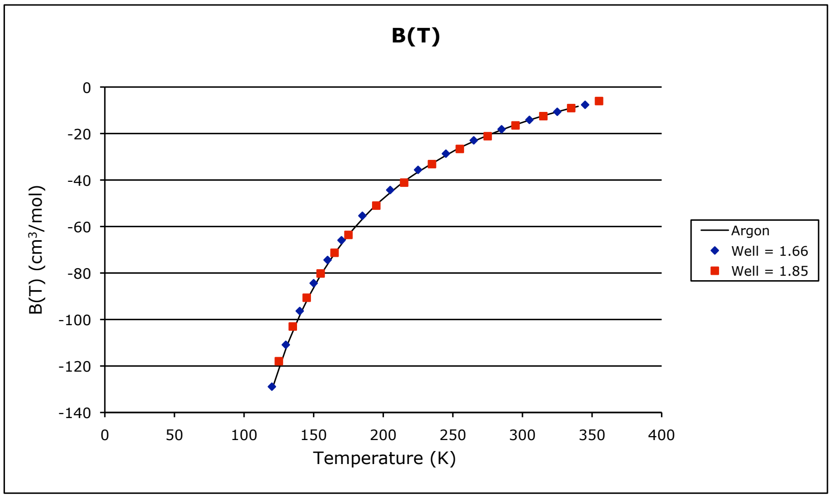

Figure 3.35 – B(T) predicted by the truncated virial expansion for various well widths, and B(T) from experimental data[7].

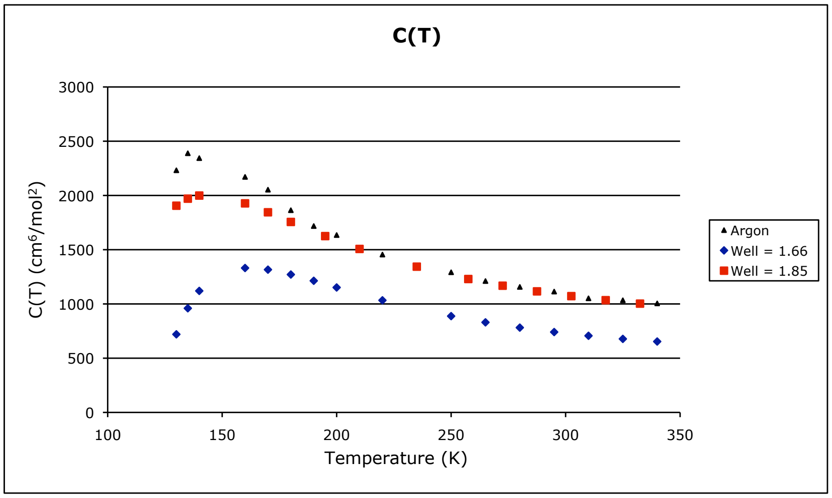

Figure 3.36 – C(T) predicted by the truncated virial expansion for various well widths, and C(T) from experimental data[7].

It can be concluded that virial coefficients can be used to calculate thermodynamic quantities and that the square well model can be used to accurately approximate more general spherically symmetric molecular models for the purpose of calculating virial coefficients. The square well model has the benefit of being able to take advantage of the ratio integration technique discussed in chapter 2. Again, this is useful because only one simulation is needed to calculate virial coefficients at any temperature. This will be used to model new systems in later chapters.

3.4 PADÉ APPROXIMANTS

The virial equation is a power series, which lends itself nicely to the Padé approximation. In a Padé approximation a rational function, R(x), is substituted for a power series, f(x), by ensuring that all derivatives to the highest possible order agree for x=0.

$$
\begin{aligned}
f(0) &= R(0) \\
f'(0) &= R'(0) \\
f''(0) &= R''(0) \\
&\vdots
\end{aligned}
\tag{3.4.1}
$$

with f(x) and R(x) being:

$$f(x) = f_0 + f_1 x + f_2 x^2 + f_3 x^3 + \ldots \tag{3.4.2}$$

$$R(x) = \frac{P(x)}{Q(x)} = \frac{p_0 + p_1 x + p_2 x^2 + \ldots}{1 + q_1 x + q_2 x^2 + \ldots} \tag{3.4.3}$$

where q_0 is 1 by convention. The approximation comes directly from setting the difference between f(x) and R(x) to zero.

$$f(x) - \frac{P(x)}{Q(x)} = 0$$

$$f(x)Q(x) - P(x) = 0$$

$$(f_0 - p_0) + (f_1 + f_0 q_1 - p_1)x + (f_2 + f_1 q_1 + f_0 q_2 - p_2)x^2 + \ldots = 0 \tag{3.4.4}$$

As each derivative is taken and evaluated for x=0, a series of equations is formed.

$$\begin{gathered} f'(0) - R'(0) = 0 \\ f''(0) - R''(0) = 0 \\ f'''(0) - R'''(0) = 0 \\ . \\ . \\ . \end{gathered} \tag{3.4.5}$$

$$\begin{gathered} f_0 - p_0 = 0 \\ f_1 + f_0 q_1 - p_1 = 0 \\ f_2 + f_1 q_1 + f_0 q_2 - p_2 = 0 \\ . \\ . \\ . \end{gathered} \tag{3.4.6}$$

The approximation is used when the power series is only known to some order, N. The order of P(x) and Q(x), L and M respectively, must satisfy:

$$L + M + 1 = N \tag{3.4.7}$$

The Padé approximant is symbolized [L/M], with N choices for L and M. For example, the virial equation truncated after D(T), N = 4:

$$Z = \frac{\beta P}{\rho} = 1 + B(T)\rho + C(T)\rho^2 + D(T)\rho^3 \tag{3.4.8}$$

has approximants [0/3], [1/2], [2/1], and [3/0], where [3/0] is just the truncated power series.

The Padé approximant often is a better approximation of the complete power series than the truncated virial series using the same number of terms, but the most appropriate one must be chosen. For example the exponential function, e^x, can be defined as a power series:

$$e^x = \sum_{n=0}^{\infty} \frac{x^n}{n!} = 1 + x + \frac{x^2}{2!} + \frac{x^3}{3!} + \frac{x^4}{4!} + \dots \tag{3.4.9}$$

In figure 3.37 the approximations for the truncated power series at N=5 are displayed along with the exact value e^x, note that [4/0] represents the truncated power series. The Padé approximant [3/1] does a better job over the region of estimating e^x than the truncated power series.

In figure 3.38 the approximations are shown for N=6. Adding coefficients to the power series increases the accuracy of the approximants and the truncated power series. The range of interest must be taken into consideration when choosing an approximation, in figure 3.38 the truncated power series [5/0] is the most accurate, but the same functions over a different range in figure 3.39 reveal [1/4] to be the most accurate (where figure 3.40 shows the percent error over the range).

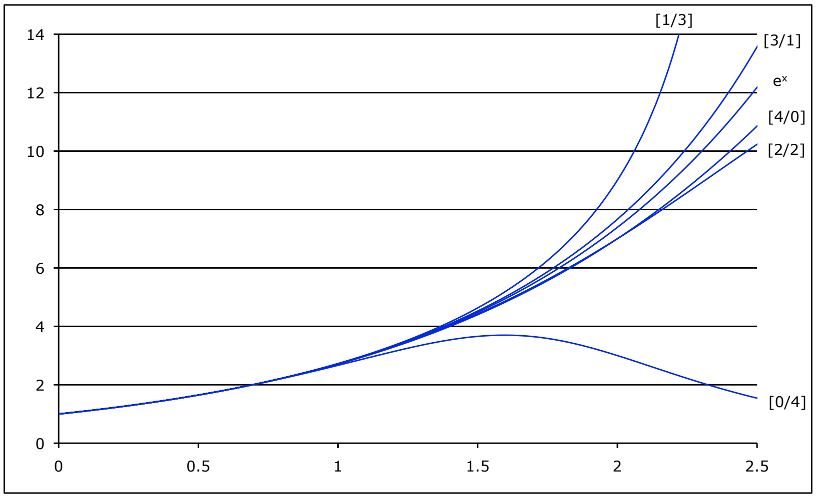

Figure 3.37 – The exponential function, e^x, is plotted along with the series truncated at N=5 ([4/0]) and four other Padé approximants ([0/4], [1/3], [2/2], and [3/1]).

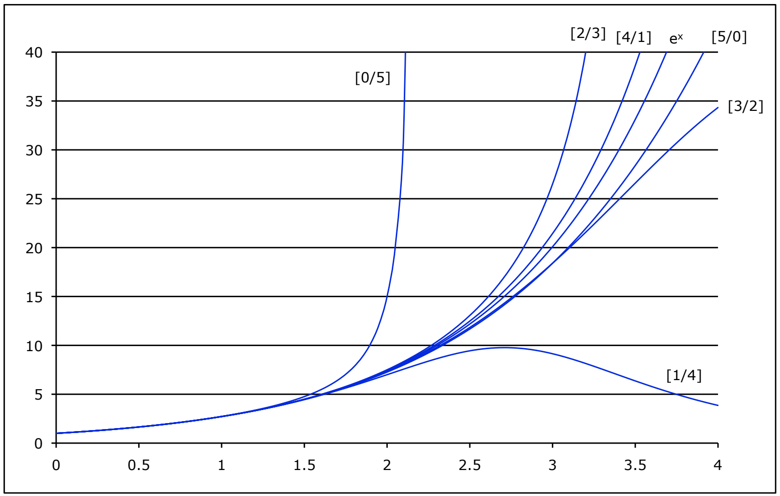

Figure 3.38 - The exponential function, e^x, is plotted along with the series truncated at N=6 ([5/0]) and five other Padé approximants ([0/5], [1/4], [2/3], [3/2], and [4/1]).

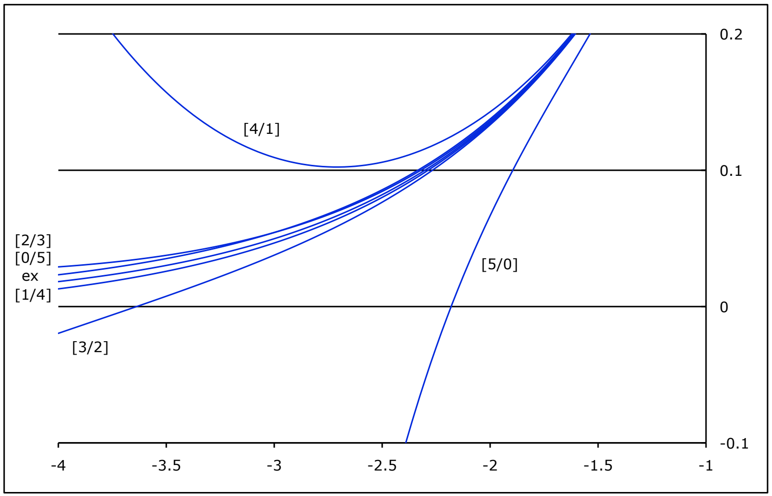

Figure 3.39 – The exponential function, e^x, is plotted along with the series truncated at N=6 ([5/0]) and five other Padé approximants ([0/5], [1/4], [2/3], [3/2], and [4/1]).

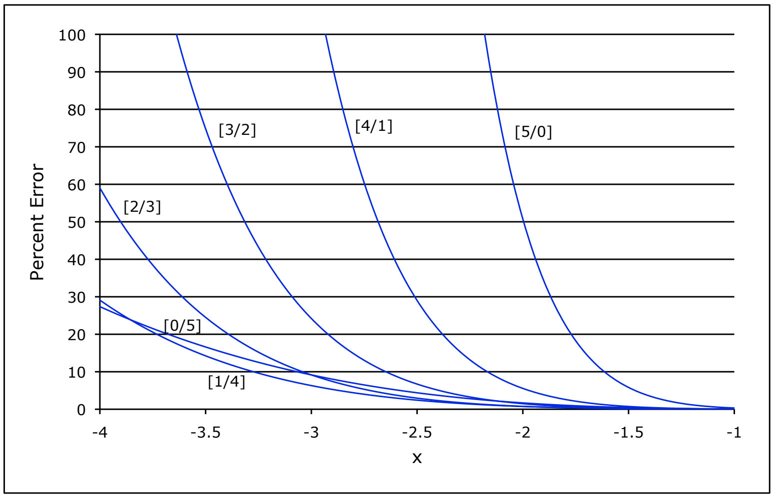

Figure 3.40 – Percent error between the exponential function and the power series truncated at N=6 ([5/0]) and five other Padé approximants ([0/5], [1/4], [2/3], [3/2], and [4/1]).

Padé approximants have been used often to extrapolate virial-coefficient data. They can be used to increase the accuracy of the virial equation of state, to predict higher ordered virial coefficients, or to investigate the convergence of the virial equation. The range of interest (for most applications) would be (somewhere within the interval) from infinity dilute ($\rho^* = 0$) to the close packing density ($\rho^* = 3\sqrt{2}/\pi$).

For the exponential power series all the coefficients are positive, this is not in general true for the virial coefficients of molecular models (all known coefficients for the hard sphere potential are positive, but the possibility exists that higher order coefficients are negative[8]). The result is positive terms canceling negative terms in the virial equation of state. Including higher order coefficients to the truncated equation is not guaranteed to increase the accuracy. For this reason the comparison of the negative region in figures 3.39 and 3.40 is particularly applicable. In the negative region the terms alternate sign and large values cancel each other; ignoring a value can lead to serious error. The Padé approximation doesn't suffer from this restriction. However this problem manifests itself as the denominator approaches zero.

For example, in figure 3.21 from section 3.2 no coexistence data could be generated for a square well potential with $\lambda = 2$ at $T^* = 5$ for the virial equation truncated at E(T). Using the Padé approximant [3/1] this is now possible as shown in figure 3.41.

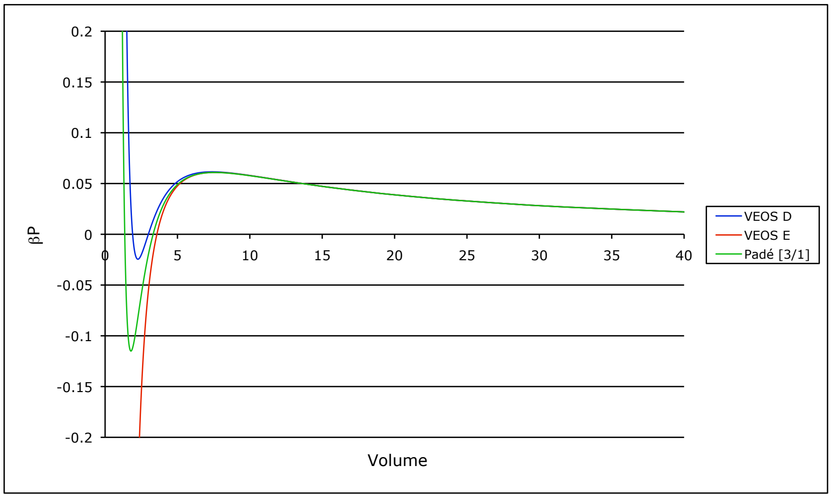

Figure 3.41 – Pressure v Volume for the square potential with λ = 2 at T* = 5 using the equations of state indicated.

An interesting method[9] for choosing which approximant to use has been developed. For the virial equation of order N, all approximants for order N-1 are calculated. The predicted value of the virial coefficient of order N, using (3.3.5), is then compared to the known value for each of the approximants. The value for N+1 is then calculated using the approximant that best matched N. Finally all approximants are calculated at order N, and the one which bests matches the predicted value for N+1 is chosen.

Rather than performing this calculation directly for each virial equation, it has been found to work best when the approximants chosen as most accurate in [9] are used. They are:

N	Best Approximant
2	[0/1]
3	[0/2]
4	[0/3] or [2/1]
5	[2/2]
6	[3/2]
7	[3/3] or [4/2]
8	[2/5]
9	[6/2]

Table 3.1 – The best Padé approximants, by order, for the hard sphere potential from [9], these have been found to be the best approximants for the square-well model as well.

Padé approximants present a simple method for increasing the accuracy of the virial expansion. This increase is even more effective as higher order virial coefficients are added.

3.5 MIXTURES

In an n-component mixture the virial expansion is given as:

$$\frac{\beta P}{\rho_m} = 1 + B_m(T)\rho_m + C_m(T)\rho_m^2 + D_m(T)\rho_m^3 + ... \tag{3.5.1}$$

In 3.5.1 ρ_m is the density of the mixture, given by the sum of densities for each component (ρ_i):

$$\rho_m = \sum_i^n \rho_i \tag{3.5.2}$$

The virial coefficients of the mixtures are given by:

$$\begin{gathered} B_m = \sum_i^n \sum_j^n x_i x_j B_{ij} \\ C_m = \sum_i^n \sum_j^n \sum_k^n x_i x_j x_k C_{ijk} \\ D_m = \sum_i^n \sum_j^n \sum_k^n \sum_l^n x_i x_j x_k x_l D_{ijkl} \\ . \\ . \\ . \end{gathered} \tag{3.5.3}$$

In 3.5.3 x_i is the mole fraction of component i and B_{ij} is the value of the second virial coefficient calculated for molecules of type i and j. Over counting is allowed so the first two coefficients of a two component mixture is given by:

$$\begin{gathered} B_m = x_i^2 B_{ii} + 2x_i x_j B_{ij} + x_j^2 B_{jj} \\ C_m = x_i^3 C_{iii} + 3x_i^2 x_j C_{iij} + 3x_i x_j^2 C_{ijj} + x_j^3 C_{jjj} \end{gathered} \tag{3.5.4}$$

As noted by Monago[10] the virial equation is the only method capable of predicting volumetric and caloric properties of mixtures in the gas phase at experimental uncertainties, and as such has value in applications that demand accurate values. One example being high-throughput gas density transducers used in custody transfers in the natural gas industry[11]. The truncated virial equation of state fails to accurately predict properties at densities above about a third the critical density (depending on the number of coefficients used), and as a result fails to accurately predict phase equilibrium as temperature approaches the critical point. However, densities are lower than this region during custody transfers.

Virial coefficients are used in the natural gas industry to calculate compressibility factors (Z) at given temperatures, pressures and compositions. A well-known and very successful method developed by the Group Européen de Recherches Gazières (GERG) in 1988[12] relies on high-accuracy measurements of Z to determine virial parameters.

In the GERG method the equation of state for a mixture is taken as 3.5.1 truncated after $C_m(T)$. The virial coefficients are approximated by:

$$\begin{aligned} B_{ij} &= b_{ij}^{(0)} + b_{ij}^{(1)}T + b_{ij}^{(2)}T^2 \\ C_{ijk} &= c_{ijk}^{(0)} + c_{ijk}^{(1)}T + c_{ijk}^{(2)}T^2 \end{aligned} \tag{3.5.5}$$

First high-accuracy values of Z for pure substances are used to determine B_{ii} and C_{iii}. Then binary mixture data is used in conjunction with the B_{ii} and C_{iii} values to determine B_{ij} C_{iij} and C_{ijj}. These values are then used with ternary mixture Z's to determine C_{ijk}. Finally this data (across many temperatures) is used to determine $b^{(0)}$, $b^{(1)}$, $b^{(2)}$, $c^{(0)}$, $c^{(1)}$ and $c^{(2)}$ for pure substances as well as binary and ternary mixtures. The advantage being that because the virial equation is truncated at C(T) only ternary interactions are needed to calculate compressibility factors for mixtures with more than three components.

The authors of [11] have improved on this method by replacing the approximation in 3.5.5 with:

$$\begin{aligned} B_{ij} &= b_{ij,0} + \frac{b_{ij,1}}{T} + \frac{b_{ij,2}}{T^2} \\ C_{ijk} &= c_{ijk,0} + \frac{c_{ijk,1}}{T} + \frac{c_{ijk,2}}{T^2} \end{aligned} \tag{3.5.6}$$

In both cases the authors note that the virial expansion is rigorously based in statistical mechanics as a justification to choose it as a model. However, the approximations 3.5.5 and 3.5.6 are not. The two approximations rely heavily on fitting many coefficients to high-accuracy values of Z. For a two-component mixture, for example, there are 21 independent variables. It is therefore not surprising that for binary and ternary mixtures this method is highly accurate.

The square-well potential can be used to model the interaction of gases as discussed in section 3.3, virial coefficients can then be calculated as previously described. B(T) data was again taken from [13] to parameterize the square-well model for the pair potentials of methane and diatomic nitrogen. B_{12} values are also used to approximate the methane-nitrogen interaction as shown in figures 3.42 – 3.44. The results are listed in table 3.2 and graphically in figure 3.45.

	σ (Å)	λ	ε/k (K)
$CH_4 - CH_4$	3.387	1.63	132.5
$N_2 - N_2$	3.320	1.63	85
$CH_4 - N_2$	3.215	1.5	140.8

Table 3.2 – The square-well parameters for the interactions indicated.

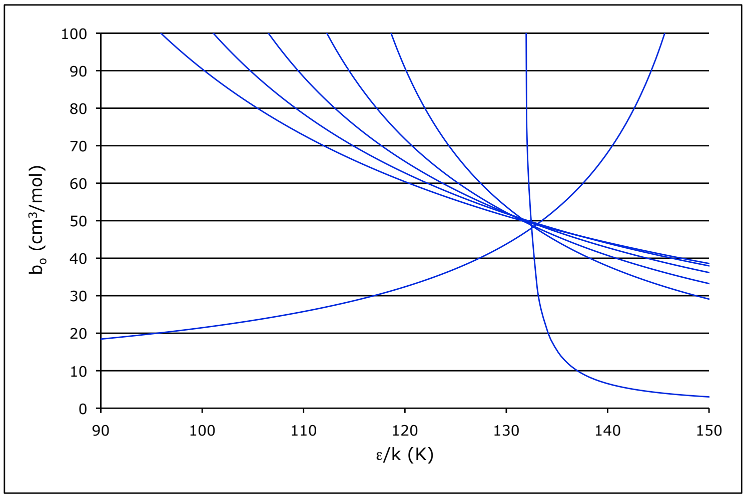

Figure 3.42 – Predicted values of b_o from ε/k and experimental methane data for a well width of 1.63.

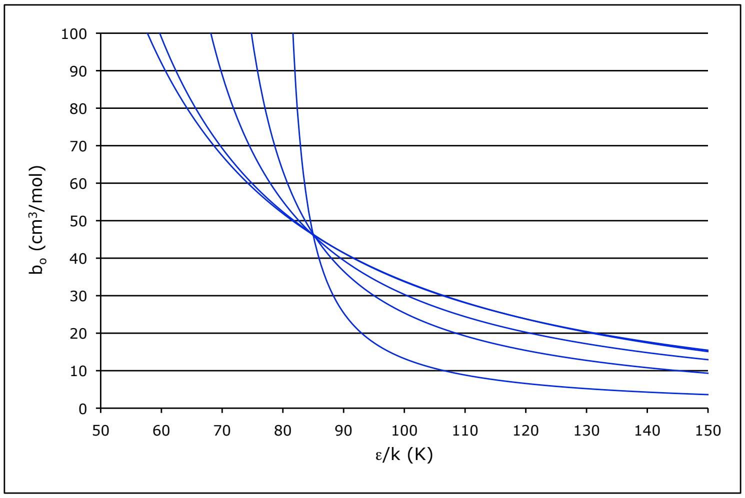

Figure 3.43 – Predicted values of b_o from ε/k and experimental nitrogen data for a well width of 1.63.

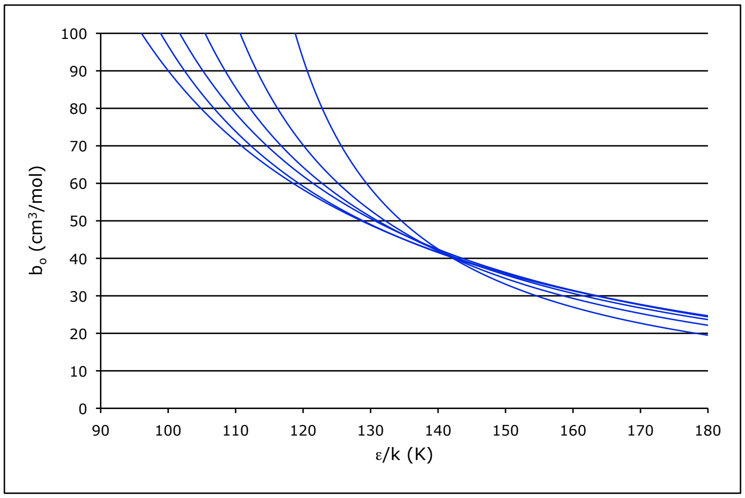

Figure 3.44 – Predicted values of b_o from ε/k and experimental methane-nitrogen mixture data for a well width of 1.5.

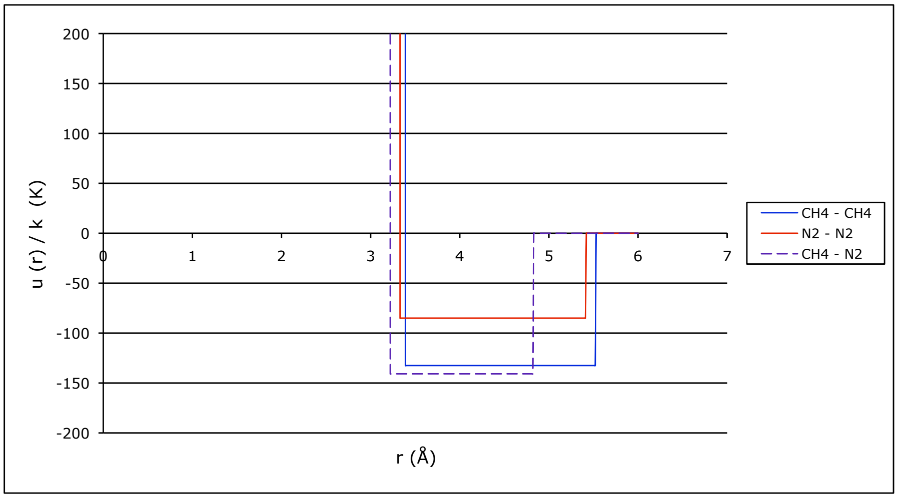

Figure 3.45 – Pair potential for methane, nitrogen, and a mixture modeled by the square-well potential.

For pure substances the virial coefficients are calculated using the exact expressions for B(T) up to D_2(T) as described in chapter 1. Higher order coefficients are calculated through ratio integration as described in chapter 2. Compressibility factors predicted by the truncated virial expansion at D(T) are compared to experimental results in[12] in table 3.3. All predicted values are within .1% of experimental compressibility factors.

T (K)	P (MPa)	Z D(T)	Z exp	Abs % Dev
273.16	2.0006	0.9529	0.9532	0.03
273.17	3.0006	0.9290	0.9297	0.07
273.18	4.0005	0.9051	0.9065	0.15
273.15	4.9998	0.8812	0.8836	0.27
273.16	6.0005	0.8576	0.8612	0.42
273.15	7.0004	0.8344	0.8398	0.64
273.16	8.0005	0.8121	0.8197	0.92
283.17	2.0002	0.9587	0.9587	0.001
283.17	3.0002	0.9380	0.9385	0.06
283.17	4.0002	0.9173	0.9184	0.12
283.16	5.0003	0.8968	0.8989	0.23
283.16	6.0002	0.8767	0.8799	0.37
283.16	7.0002	0.8570	0.8619	0.57
293.15	2.0000	0.9637	0.9640	0.03
293.15	3.0000	0.9456	0.9461	0.05
293.16	4.0000	0.9277	0.9287	0.10
293.15	5.9999	0.8928	0.8957	0.33
293.15	6.9999	0.8760	0.8803	0.49

Table 3.3 – Compressibility factors (Z) for pure methane from experiment (Z exp) and predicted by virial coefficients for the square-well model truncated at D(T).

For mixtures B(T) can be computed with equation 3.5.4 using the square-well parameters from table 3.2. C(T) is more difficult, because it involves integrals with different pair potentials. In equation 3.5.4 C_{iii} and C_{jjj} can be calculated as usual using the exact equation for C(T) for square-wells (1.9.37 and 1.9.38). For C_{iij} and C_{ijj} Kihara[14, 15] has generalized the exact solution for C(T) for a mixture of square-wells.

For D(T) there are no exact solutions to a mixture of square-well potentials for any of the three integrals despite analytical solutions to D_1 and D_2 for pure square-wells. A solution can be reached by approximating the CH_4 – N_2 interaction with a square-well potential that has the same well width (1.63). Kihara[14, 15] has also provided a method for approximating binary square-well interactions given the unary ones. The hard-core diameter is the arithmetic mean and the depth is the geometric mean:

$$\sigma_{AB} = \frac{\sigma_{AA} + \sigma_{BB}}{2} \tag{3.5.7}$$

$$\varepsilon_{AB} = \sqrt{\varepsilon_{AA}\varepsilon_{BB}} \tag{3.5.8}$$

Using values from table 3.2 the CH_4 – N_2 interaction can be approximated by:

	σ (Å)	λ	ε/k (K)
CH_4 – N_2	3.215	1.63	106.1

For a binary mixture each integral in D(T), D_1 D_2 and D_3, are given by:

$$D = x_A^4 D_{AAAA} + 4x_A^3 x_B D_{AAAB} + 6x_A^2 x_B^2 D_{AABB} + 4x_A x_B^3 D_{ABBB} + x_B^4 D_{BBBB} \tag{3.5.9}$$

D_{AAAA} and D_{BBBB} Can be calculated in the normal way. The other integrals can be solved by first setting σ_{AA} and σ_{BB} to σ_{AB}. Since now $\lambda_{AA} = \lambda_{BB} = \lambda_{AB}$ and $\sigma_{AA} = \sigma_{BB} = \sigma_{AB}$ the volume of the integrals are known; only the value of h ($h = e^{-\beta\varepsilon} - 1$) within each volume is unknown. The integrals are solved then by breaking them down into volumes by powers of h. The values used for h^n are the average value of h^n weighted by examining every possible labeling and selection of h bonds.

For D1$_{AAAB}$ the integral is given by only 1 unique labeling (where ‘A’ and ‘B’ represent molecules of that type, and bonds are represented by A-A = a, B-B=b, and A-B=c).

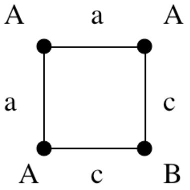

Since each h-bond is equally likely to be chosen the value of h^n values used to compute D1$_{AAAB}$ are:

$$h = (a+c)/2 \tag{3.5.10}$$

$$h^2 = (a^2+c^2+4ac)/6 \tag{3.5.11}$$

$$h^3 = (a^2c+ac^2)/2 \tag{3.5.12}$$

$$h^4 = a^2c^2 \tag{3.5.13}$$

D1$_{ABBB}$ has the same symmetry as D1$_{AAAB}$ so the values of h^n can be retrieved from 3.5.10 – 3.5.13 by substituting ‘b’ for ‘a’.

D1$_{AABB}$ can be represented by two uniquely labeled graphs:

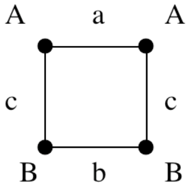

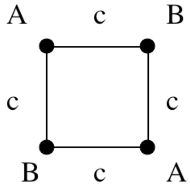

However, these should not be weighted equal, because they do not occur with equal probability. This can be seen by labeling all unique possibilities for particles 1 to 4:

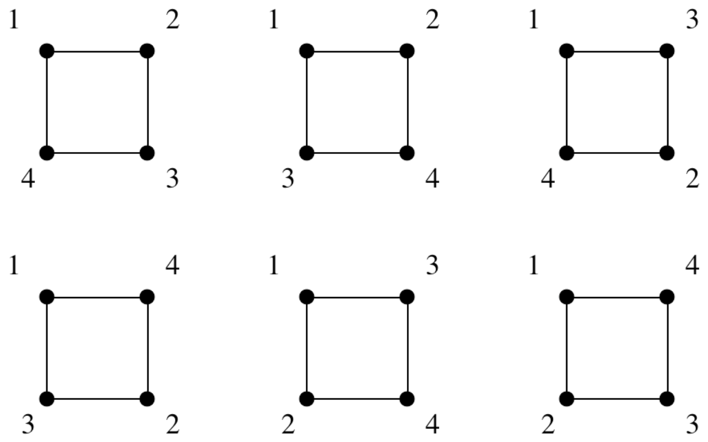

If 1 and 2 are replaced by ‘A’, and 3 and 4 are replaced by ‘B’, it becomes obvious that the weights should be:

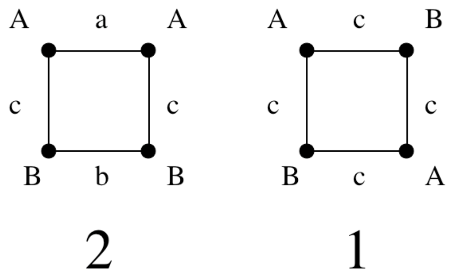

making the h^n values for $D1_{AABB}$:

$$h = (a + b + 4c)/6 \tag{3.5.14}$$

$$h^2 = (ab + 2ac + 2bc + 4c^2)/9 \tag{3.5.15}$$

$$h^3 = (ac^2 + bc^2 + 2abc + 2c^3)/6 \tag{3.5.16}$$

$$h^4 = (2abc^2 + c^4)/3 \tag{3.5.17}$$

Following the same procedure for D2:

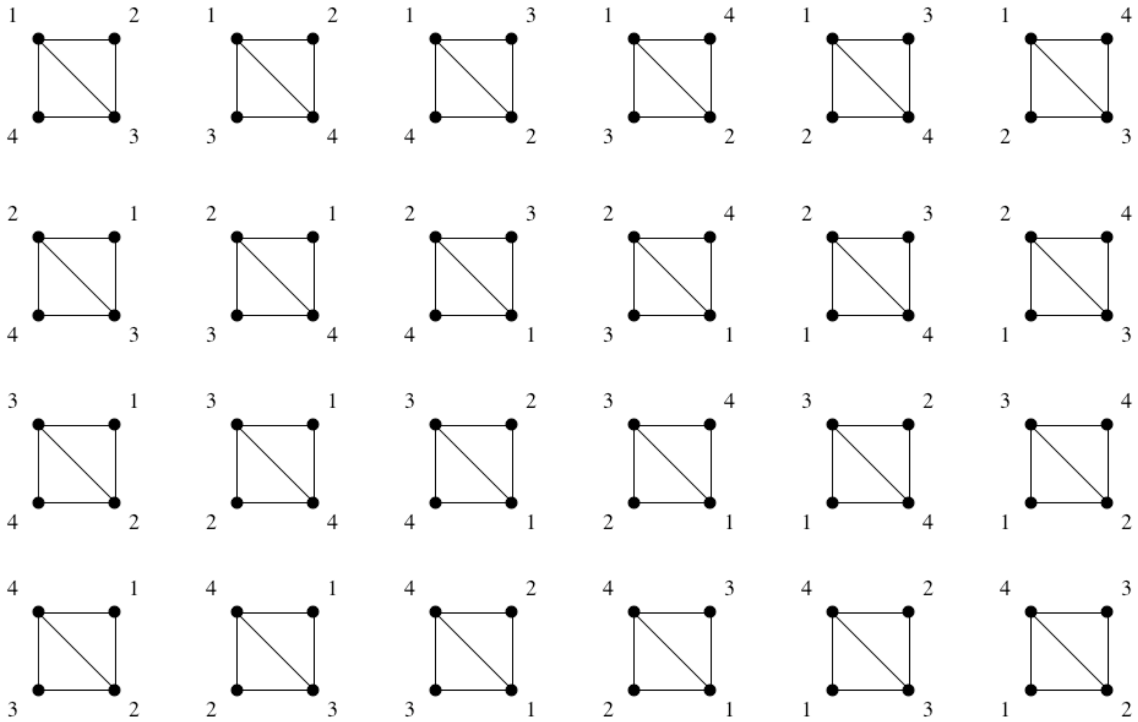

For D2$_{AAAB}$ we replace any three numbers (ex. 1,2,3) with 'A' and the other (ex. 4) with 'B'. The weights are equal between:

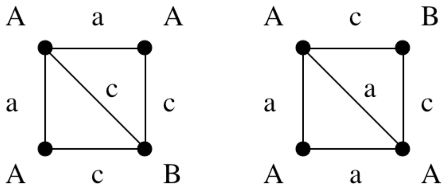

making the h^n values:

$$h = (a + c)/2 \tag{3.5.18}$$

$$h^2 = (a^2 + c^2 + 3ac)/5 \tag{3.5.19}$$

$$h^3 = (a^3 + 9a^2c + 9ac^2 + c^3)/20 \tag{3.5.20}$$

$$h^4 = (a^3c + 3a^2c^2 + ac^3)/5 \tag{3.5.21}$$

$$h^5 = (a^3c^2 + a^2c^3)/2 \tag{3.5.22}$$

Again D2$_{ABBB}$ has the same symmetry and can be recovered by replacing 'a' with 'b' in 3.5.18 – 3.5.22.

For D2$_{AABB}$ the weights are obtained by replacing two numbers in the numeric diagram with 'A' and the other two with 'B':

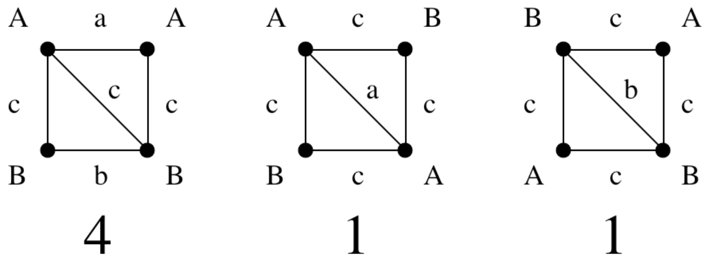

For D2$_{AABB}$ the h^n values are (grouped by the diagram they come from for pedagogical purposes):

$$h = [4(a+b+3c) + (4c+a) + (4c+b)]/30 \tag{3.5.23}$$

$$h^2 = [4(ab+3ac+3bc+3c^2) + (4ac+6c^2) + (4bc+6c^2)]/60 \tag{3.5.24}$$

$$h^3 = [4(3abc+3ac^2+3bc^2+c^3) + (6ac^2+4c^3) + (6bc^2+4c^3)]/60 \tag{3.5.25}$$

$$h^4 = [4(3abc^2+ac^3+bc^3) + (4ac^3+c^4) + (4bc^3+c^4)]/30 \tag{3.5.26}$$

$$h^5 = [4abc^3+ac^4+bc^4]/6 \tag{3.5.27}$$

The particles in D3 are fully connected, and therefore all are identical making D3$_{AAAB}$, D3$_{AABB}$ and D3$_{ABBB}$ simply:

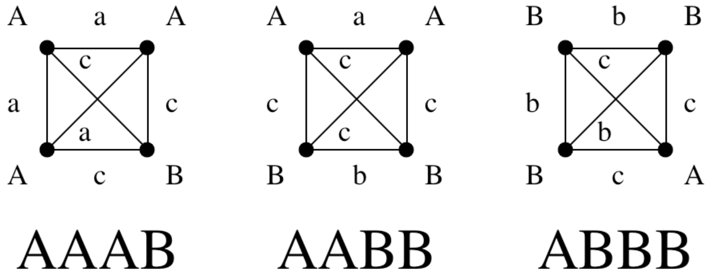

So the h^n values for D3$_{AAAB}$ are (where, again, D3$_{ABBB}$ is obtained by substituting ‘b’ for ‘a’):

$$h = (a+c)/2 \tag{3.5.28}$$

$$h^2 = (a^2+3ac+c^2)/5 \tag{3.5.29}$$

$$h^3 = (a^3+9a^2c+9ac^2+c^3)/20 \tag{3.5.30}$$

$$h^4 = (a^3c+3a^2c^2+ac^3)/5 \tag{3.5.31}$$

$$h^5 = (a^3c^2+a^2c^3)/2 \tag{3.5.32}$$

$$h^6 = a^3c^3 \tag{3.5.33}$$

And the values for $D3_{AABB}$:

$$h = (a + b + 4c)/6 \tag{3.5.34}$$

$$h^2 = (ab + 4ac + 4bc + 6c^2)/15 \tag{3.5.35}$$

$$h^3 = (2abc + 3ac^2 + 3bc^2 + 2c^3)/10 \tag{3.5.36}$$

$$h^4 = (6abc^2 + 4ac^3 + 4bc^3 + c^4)/15 \tag{3.5.37}$$

$$h^5 = (4abc^3 + ac^4 + bc^4)/6 \tag{3.5.38}$$

$$h^6 = abc^4 \tag{3.5.39}$$

The values of h^n can now be combined with the volume of the integrals in the same manner as discussed with ratio integration in chapter 2. The integrals are scaled by a factor of $(2\pi\sigma^3/3)^3$, with σ_{AB} is used. Equation 3.5.9 is used to determine D(T) for the mixture.

The compressibility factor for mixtures were calculated using 4 different virial expansions (where the subscript indicates the well width used for the CH_4 – N_2 interaction):

$$Z_1 = 1 + B_{1.5}\rho + C_{1.5}\rho^2 \tag{3.5.40}$$

$$Z_2 = 1 + B_{1.63}\rho + C_{1.63}\rho^2 \tag{3.5.41}$$

$$Z_3 = 1 + B_{1.5}\rho + C_{1.5}\rho^2 + D_{1.63}\rho^3 \tag{3.5.42}$$

$$Z_4 = 1 + B_{1.63}\rho + C_{1.63}\rho^2 + D_{1.63}\rho^3 \tag{3.5.43}$$

Table 3.4 compares the 4 compressibility factors calculated with the truncated virial expansion with the one from experimental data for a mixture of 48.4% CH_4 and 51.6% N_2 from [12]. The absolute percent deviations between experimental values are listed in table 3.5. Not surprisingly, the addition of D(T) increases the accuracy at higher pressures/densities and has little effect at low pressures/densities. The most accurate approximation is Z_3 which uses the more accurate cross-species interaction potential for B(T) and C(T); and switches to a potential with like width for D(T). All are accurate to less than .5% for all but the highest pressures/densities.

P/MPa	0.27122	0.49451	0.90055	1.63635	2.9632	5.34369	9.64011
Z_{EXP}	0.99752	0.99551	0.99191	0.9856	0.975	0.9586	0.9395
Z_1	0.99754	0.99553	0.9919	0.9854	0.9741	0.9553	0.9268
Z_2	0.99742	0.99532	0.99153	0.9848	0.9732	0.9541	0.9268
Z_3	0.99754	0.99553	0.9919	0.9854	0.9742	0.9557	0.9295
Z_4	0.99742	0.99532	0.99154	0.9848	0.9733	0.9545	0.9295

Table 3.4 – Experimental compressibility factors from [12] compared to the 4th virial expansion (3.5.40) – (3.5.43).

P/MPa	0.27122	0.49451	0.90055	1.63635	2.9632	5.34369	9.64011
Z_1	0.0019	0.0017	0.0013	0.017	0.088	0.347	1.36
Z_2	0.0097	0.0191	0.0379	0.08	0.186	0.467	1.35
Z_3	0.0019	0.0017	0.0011	0.016	0.081	0.303	1.07
Z_4	0.0097	0.0191	0.0378	0.079	0.179	0.423	1.06

Table 3.5 – Absolute percent deviation between experimental compressibility factors from [19] and those calculated from the 4 virial expansion (3.5.40) – (3.5.43).

For both the pure component and binary mixture compressibility factors calculated in [12] provide much better accuracy, but this is not surprising since this is the data the coefficients in [12] were derived from. When expanding the approximations to mixtures with more than two components, parameters for the methods described in [12] and [11] (using equations 3.5.5 and 3.5.6, respectively) rely on unary, binary and ternary mixture data for every possible combination of components. The method of approximation by a square-well pair potential, however, needs only B(T) data for the pure components and binary mixtures. The number of parameters needed for an n-component mixture using the methods from either [12] or [11] are given by:

$$3\binom{n+2}{3} + 3\binom{n+1}{2} = \frac{n^3}{2} + 3n^2 + 3n \tag{3.5.44}$$

The number of parameters using the square-well method is significantly smaller, given by:

$$3\binom{n+1}{2} = \frac{3}{2}(n^2 + n) \tag{3.5.45}$$

This method could be improved by using more recent (and likely more accurate) data for B(T) values than [13]. Higher order virial coefficients could be added in with the same method as D(T) with increasing difficulty (although E(T) can be added fairly trivially). This would also allow for the use of Padé approximants. The approximation was aided by CH_4 and N_2 both being approximated with a well width of 1.63, so it remains to be seen whether species with different well widths perform worse. It also remains to be seen how well this approximation will handle mixtures with more components and on a larger temperature range.

References

[1] Maxwell, J. C., 1965 (c1890), *The Scientific Papers of James Clerk Maxwell*, Dover, 424.

[2] Hirschfelder, J. O., Curtiss, C. F., Bird, R. B., 1966, *Molecular Theory of Gases and Liquids*, (John Wiley & Sons, New York).

[3] Gilgen, R., Kleinrahm, R., Wagner, W., 1994, *J. Chem. Thermodyn.*, **26**, 383.

[4] Bokis, C. P., Donohue, M. D., Hall, C. K., 1994, *Ind. Eng. Chem. Res.*, **33**, 146.

[5] Michels, A., DeGraaff, W., Ten Seldham, C. A., 1960, *Physica*, **26**, 393.

[6] Dymond, J. H., Smith, E. B., 1980, *The Virial Coefficients of Pure Gases and Mixtures*, (Clarendon Press, Oxford).

[7] Tegler, C., Span, R., Wagner, W., 1999, *J. Phys. Chem. Ref. Data.*, **28**, 779.

[8] Clisby, N., McCoy, B. M., 2006, *J. Stat. Phys.*, **122**, 15.

[9] Guerrero, A. O., Bassi, A. B. M. S., 2008, *J. Chem. Phys.*, **129**, 044509.

[10] Monago, K. O., 2010, *Can. J. Chem. Eng.*, **88**, 55.

[11] Estela-Uribe, J. F., Jeramillo, J., Salazar, M. A., Trusler, J. P. M., 2003, *Fluid Phase Equilib.*, **204**, 169.

[12] Jaeschke, M., Audibert, S., van Caneghem, P., Humphreys, A. E., Janssen-van Rosmalen, R., Pellei, Q., Michels, J. P. J., Schouten, J. A., ten Seldam, C. A., 1989, *High accuracy compressibility factor calculation for natural gases and similar mixtures by use of a truncated virial equation*, (GERG Technical Monograph TM 2).

[13] Dymond, J. H., Smith, E. B., 1980, *The Virial Coefficients of Pure Gases and Mixtures*, (Clarendon Press, Oxford).

[14] Kihara, T., 1953, *Rev. Mod. Phys.*, **25**, 831.

[15] Kihara, T., 1955, *Rev. Mod. Phys.*, **27**, 412.

[16] Kroto, H. W., Heath, J. R., O’Brien, S. C., Curl, R. F., Smalley, R. E., 1985, *Nature*, **318**, 162.

Chapter 4
Modeling Other Potentials

4.1 MAYER SAMPLING

As introduced in section 2.1 Mayer Sampling is a technique to solve cluster integrals using importance sampling and free-energy perturbation techniques[1]. Mayer Sampling has been used to calculate virial coefficients for a variety of potentials[1-7] as well as other cluster integrals[8-9].

A typical Monte Carlo simulation samples states of an ensemble, using a collection of molecules on the order 10^3 to 10^4. In Mayer sampling, however, only the molecules involved in the cluster integral are included in the simulation. The molecules are allowed to move over all space, but are sampled according to a probability distribution (π), and compared to a reference system (denoted with a 'o' subscript) whose cluster integral is known.

$$\Gamma(T) = \Gamma_0(T)\frac{\langle\gamma/\pi\rangle}{\langle\gamma_0/\pi\rangle} \tag{4.1.1}$$

Instead of directly calculating the integral, the expectation value (weighted by π) of the integrand (γ) is found for the system of interest and the reference system. The solution to the integral is the product of the known value of the cluster integral for the reference system, $\Gamma_o(T)$, and the ratio of $<\gamma/\pi>$ and $<\gamma_o/\pi>$ (where the angled brackets denote an ensemble average or expectation value).

For virial coefficients, the calculation begins with the number of particle in the cluster integral being evaluated (n). Each particle is assigned three Cartesian coordinates (x, y, z) to define its position. The distances between all particles are calculated and used to calculate all possible f-bonds. The f-bonds are then used to calculate the integrand value at this configuration.

All cluster integrals contributing to a virial coefficient are calculated in one simulation. The integrand (γ) to be calculated is the weighted sum of the integrands of the contributing cluster integrals. For example D(T) is the sum of three integrals (D1, D2, and D3) with coefficients -3/8, -3/4, and –1/8 respectively. So:

$$\begin{aligned}\gamma = &-\frac{3}{8}f_{1,2}f_{2,3}f_{3,4}f_{1,4} \\ &\qquad -\frac{3}{4}f_{1,2}f_{2,3}f_{3,4}f_{1,4}f_{1,3} - \frac{1}{8}f_{1,2}f_{2,3}f_{3,4}f_{1,4}f_{1,3}f_{2,4}\end{aligned} \tag{4.1.2}$$

The particles are considered unlabeled, so all possible labeling permutations are considered. Since the weight given to each integral is the number of ways it can be labeled, by summing all possible permutations the inclusion of the correct coefficient is ensured.

Therefore, the contributions are calculated by:

$$\begin{aligned}D1 = &\ f_{1,2}f_{2,3}f_{3,4}f_{1,4} \\ &+ f_{1,2}f_{2,4}f_{3,4}f_{1,3} \\ &+ f_{1,3}f_{2,3}f_{2,4}f_{1,4} \\ D2 = &\ f_{1,2}f_{2,3}f_{3,4}f_{1,4}f_{1,3} \\ &+ f_{1,2}f_{2,4}f_{3,4}f_{1,3}f_{1,4} \\ &+ f_{1,3}f_{2,3}f_{2,4}f_{1,4}f_{1,2} \\ &+ f_{1,2}f_{2,3}f_{3,4}f_{1,4}f_{2,4} \\ &+ f_{1,2}f_{2,4}f_{3,4}f_{1,3}f_{2,3} \\ &+ f_{1,3}f_{2,3}f_{2,4}f_{1,4}f_{3,4} \\ D3 = &\ f_{1,2}f_{2,3}f_{3,4}f_{1,4}f_{1,3}f_{2,4}\end{aligned} \tag{4.1.3}$$

because the factor –1/8 is common to both γ and γ_o it cancels out and can be ignored.

This method is significantly faster than manually changing the labels and recalculating D1, D2, and D3 for each, and then weighting them accordingly. In that case each calculation of D3 after the first would produce the same result. The benefit increases significantly for higher ordered virial coefficients.

After calculating γ for the initial configuration, γ_o is calculated in the same manner for the ring cluster (D1 here) for the reference system (usually hard spheres). Then a pseudo random number generator is used to choose a random number of particles (1-n) to move (with equal likelihood of any number being chosen). Each trial consist of the chosen particles being moved by a specific length, the step size. With each point on the sphere with radius equal to the step size around the particle being equally likely to be moved to. The value of γ is then calculated at the trial separations. The trial is then either accepted or rejected according to the probability distribution.

The probability distribution (π) is taken to simply be the absolute value of the integrand sum for the system of interest, $\pi = |\gamma|$. Each trial is automatically accepted if the new probability is larger than the old. If it is smaller, than the ratio of π_{new} to π_{old} is compared to a randomly chosen number uniformly distributed between 0 and 1, and accepted if the ratio is larger. The criteria for acceptance is:

$$U(0,1) < \frac{\pi_{new}}{\pi_{old}} \tag{4.1.4}$$

Making the probability of the move being accepted:

$$min(\frac{\pi_{new}}{\pi_{old}}, 1) \tag{4.1.5}$$

After each trial the values of γ/π and γ_o/π are added to a sum from all previous trials in order to calculate their ensemble average. Since $\pi = |\gamma|$, γ/π only contributes ±1 to its sum, so only the sign of γ need to be checked for the top average. The number of trials need not be counted since this too will cancel in the final ratio, instead just the sums for γ/π and γ_o/π are stored ($\Sigma\gamma/\pi$ and $\Sigma\gamma_o/\pi$).

After the simulation has run the pre-selected number of trials, M, the value of the ratio in (4.1.1) can be calculated. Using the known value for the ring cluster integral with a hard sphere potential, $\Gamma_o(T)$, $\Gamma(T)$ is then calculated from (4.1.1).

Before the averaging begins there is a short equilibration period where the step size is changed to achieve 50% acceptance of all trial moves. Increasing the step size lowers the acceptance rate, while decreasing the step size increases the acceptance.

By storing the values for $\Sigma\gamma/\pi$ and $\Sigma\gamma_o/\pi$, future simulations for the same potential and temperature can be treated as extending the simulation rather than average multiple simulations. Rather than calculate the virial coefficient from multiple runs as the mean of their solutions, the sums for γ/π and γ_o/π can be added together and treated as data from a longer simulation. This has the added benefit of weighting the simulations by their sample size.

For example, two simulations were run for the Girifalco potential[10] to calculate C(T) at T=1930.944K with different sampling sizes (M).

Run	M	$\Sigma\gamma/\pi$	$\Sigma\gamma_o/\pi$	C(T)
1	2×10^8	-6089372	-9422756.178	1.7717
2	1×10^9	-30389780	-47192200	1.7654

C(T) is calculated from (4.1.1) with values:

$$C(T) = \frac{5}{8}\left(\frac{2\pi}{3}\right)^2 \frac{\Sigma\gamma/\pi}{\Sigma\gamma_o/\pi} \tag{4.1.6}$$

To express the combined result as C(T) we could simply take the mean and calculate C(T) = 1.7686. A more accurate value would be the mean weighted by the sampling size, C(T) = 1.7665. However, the most accurate result is obtained by:

$$C(T) = \frac{5}{8}\left(\frac{2\pi}{3}\right)^2 \frac{\Sigma\gamma/\pi_{run1} + \Sigma\gamma/\pi_{run2}}{\Sigma\gamma_o/\pi_{run1} + \Sigma\gamma_o/\pi_{run2}} \tag{4.1.7}$$

giving, again, C(T) = 1.7665. The benefit of (4.1.7) is most pronounced when the virial is closed to zero. For the Girifalco potential at T = 1737.85K, two E(T) simulations were run:

Run	M	$\Sigma\gamma/\pi$	$\Sigma\gamma_o/\pi$	E(T)
1	$5x10^8$	-429972	-46331060	0.27203
2	$5x10^8$	-143712	-45462900	0.09266

Averaging E(T) = 0.18234, but when the virial is recalculated by adding the sums from each run together using the E(T) equivalent of (4.1.7), E(T) = 0.18319.

Each simulation must have a different number seeded to the random number generator to prevent identical configurations from being sampled multiple times.

4.2 MAYER SAMPLING USES

Calculating virial coefficients is not an end in itself. They can be used to test models, predict isothermal compressibilities and other bulk properties, construct phase diagrams (as discussed in chapter 3), and investigate the closure of the virial series.

Statistical mechanical models of real systems often begin with an analytical approximation to the pair potential of the real system and attempt to derive the bulk properties through analytical or numerical methods. Some experimental data from the real system must be used to fit the parameters of the model to the real system. A successful model will be able to predict other experimentally determined properties. Mayer sampling provides a method to determine an equation of state from any pair potential model.

The second virial coefficient has long been experimentally measurable and has provided data for models to be both fitted with and tested with. Third[11,12] (and less directly fourth[13]) virial coefficients have also been determined experimentally and successfully compared to their theoretical determined coefficients.

Mayer sampling is particularly useful for complicated potentials, where analytical solutions are not possible. The most accurate analytical solutions to thermodynamic properties or virial coefficients are often applicable to simplified pair potentials. Mayer sampling can calculate virial coefficients for any model whose pair potential can be calculated, including anisotropic potentials. In his review on virial coefficients[14], Masters has suggested Mayer sampling may be useful in studying ab initio potentials or potentials that do not assume an additive pair potential but instead take into account three body interactions. Mayer sampling has also been used to calculate virial data for an embedded charge protein model as a route to predicting the osmotic pressure[15]. This allows more complex models to be developed and tested.

Recently two works by Schultz and Kofke have further increased the usefulness of Mayer sampling. In the first[16] the authors have provided a method for interpolating between virial coefficients at different temperatures. Their method reduces the error of up to 300% for simple linear interpolation at low temperatures to only a few percent (at most) and from 20% to an unperceivable level at high temperatures. Since each Mayer sampling simulation is specific for a given temperature, this ensures that unique simulations need not be run for each temperature of interest, and so greatly expands the use of Mayer sampling.

In their second work[17] the authors map the regions of the phase diagram by the minimum number of virial coefficients needed to describe the system. Or, alternatively put, where each truncation is successful. This allows engineers to choose the appropriate order for the truncated virial equation of state, but it also describes regions where the calculation of higher order virial coefficients is not necessary.

4.3 C_{60} POTENTIALS - GIRIFALCO

In 1985 Kroto et al.[18] discovered the remarkably stable C_{60} ball-shaped molecule buckminsterfullerene. Since, both experimental and theoretical scientists have been interested in this unique molecule. It is of particular interest to statistical mechanical scientists because of its large size and near spherical symmetry.

Indeed the near spherical symmetry of the molecule led Girifalco[19, 20] to approximate the intermolecular potential with an isotropic one (hereby referred to as the Girifalco potential). In it the carbon atoms are “smeared-out” evenly on the spherical surface of the molecules to produce isotropy. The intermolecular carbon-carbon potential is assumed to have be a 6-12 potential with attractive (A) and repulsive (B) variables:

$$u_{c-c}(r) = -\frac{A}{r^6} + \frac{B}{r^{12}} \tag{4.3.1}$$

The C_{60}-C_{60} potential is a function of the distance between their centers obtained by integrating (4.3.1) over the surfaces of the two spheres and scaling by the square (because there are two molecules) of the density of carbon atoms:

$$u_{c_{60}-c_{60}}(r) = \sigma^2 \int_{1,2} u_{c-c}\ d\Sigma_1 d\Sigma_2 \tag{4.3.2}$$

where Σ_1 and Σ_2 are the surfaces of the two molecules and σ is the carbon atom density equal to $60/4\pi d^2$ for C_{60} with a radius of d. The resulting Girifalco potential is:

$$u(r) = -\alpha_1 \left[\frac{1}{s(s-1)^3} + \frac{1}{s(s+1)^3} - \frac{2}{s^4}\right] + \alpha_2 \left[\frac{1}{s(s-1)^9} + \frac{1}{s(s+1)^9} - \frac{2}{s^{10}}\right] \tag{4.3.3}$$

In (4.3.3) $s = r/d$, $\alpha_1 = N^2A/12d^6$, $\alpha_2 = N^2B/90d^{12}$, where N is the number of carbons in the generalized fullerene (here 60). The values for the constants are calculated by fitting lattice sums to solid-state data. For C_{60} they are $A = 32 \times 10^{-60}$ erg cm^6, $B = 55.77 \times 10^{-105}$ erg cm^{12} and d = .71 nm.

The C60-C60 Girifalco potential is compared to the C-C unscaled and scaled in figures 4.1 and 4.2, respectively.

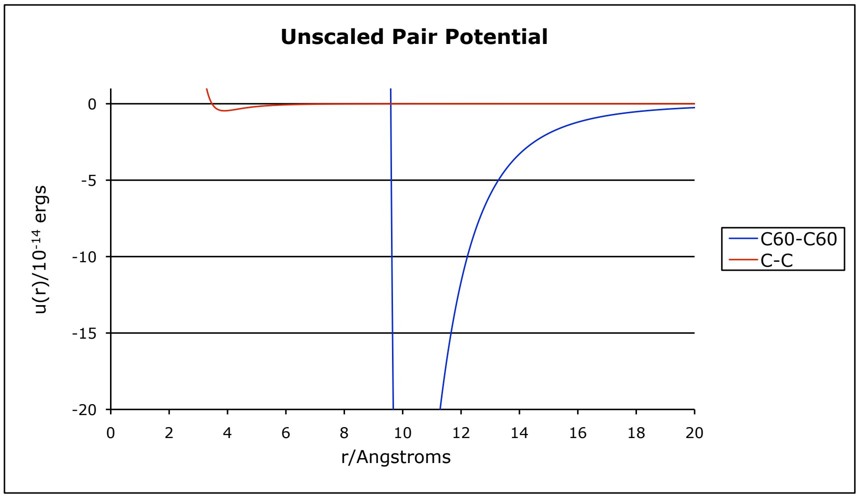

Figure 4.1 – Unscaled comparison of the Girifalco potential for C_{60} – C_{60} interactions with the approximation of C-C interaction.

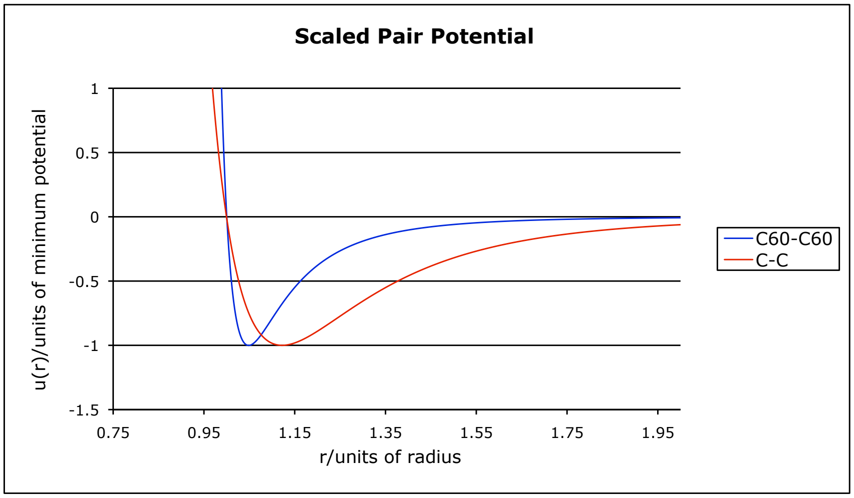

Figure 4.2 – Comparison of the Girifalco potential for C_{60} – C_{60} interactions with the approximation of C-C interaction scaled by the radii and minimum potential.

The Girifalco potential has been used extensively in the study of fullerenes. The complicated form of the potential prevents it from being used with some integral equation theory methods, but it is an ideal candidate for Mayer Sampling.

The second virial coefficient was calculated by Girifalco[20], however, the values listed are incorrect. They have been recalculated here using both Mayer Sampling and numerical integration in the mathematics program Maple. The results are listed in table 4.1.

T (K)	Girifalco[20]	Maple	Mayer Sampling
490	57,530	168023	166475
500	51,990	149526	150362
510	47,210	133716	133315
520	43,030	120128	120652
530	39,380	108386	108425
540	36,160	98190	98157
550	33,320	89294	88901
560	30,800	81496	82165
570	28,560	74633	75162
580	26,550	68567	68341
590	24,750	63186	63311
600	23,130	58394	58254
620	20,350	50273	50337
640	18050	43706	43730
660	16,140	38331	38295
680	14530	33886	33827
700	13,160	30171	30275
725	11,730	26333	26429
750	10530	23192	23188
775	9,529	20591	20562
800	8,674	18415	18389
850	7,309	15006	14980
900	6,276	12490	12481
950	5,473	10577	10578
1000	4,835	9088	9078
1050	4319	7904	7903
1100	3,894	6944	6937
1150	3,539	6155	6152
1200	3,239	5496	5498
1300	2,760	4464	4463
1400	2,400	3698	3697

Table 4.1 – B(T) calculation results for the Girifalco potential using Maple and Mayer sampling compared to those from reference [20] where the values listed are –B(T) cm^3/mol.

The results from Maple and Mayer sampling in Table 4.1 show good agreement and reproduce the graph of B(T) for the Girifalco potential presented by Osman and Khedr[21], although the authors don't mention the discrepancy with the original Girifalco result. Simulations were also done for the third, fourth and fifth virial coefficients (figures 4.3 - 4.6).

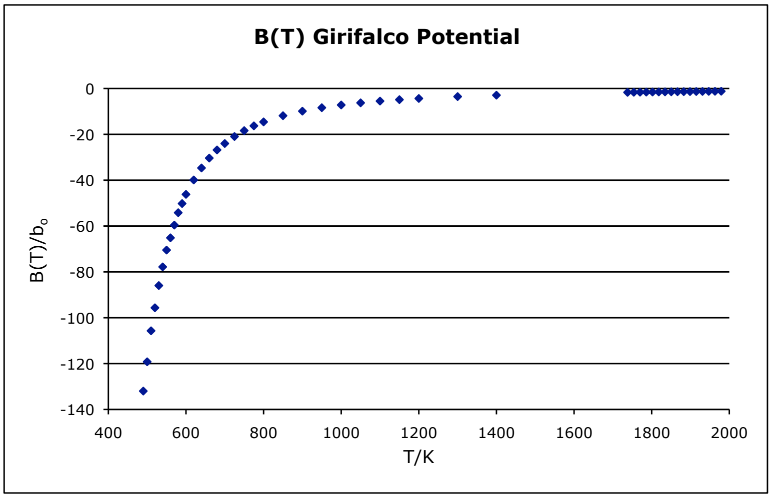

Figure 4.3 – The second virial coefficient for the Girifalco potential in units reduced by the hard sphere second virial coefficient, $b_0 = 2\pi\sigma^3/3$, with σ = 1 nm.

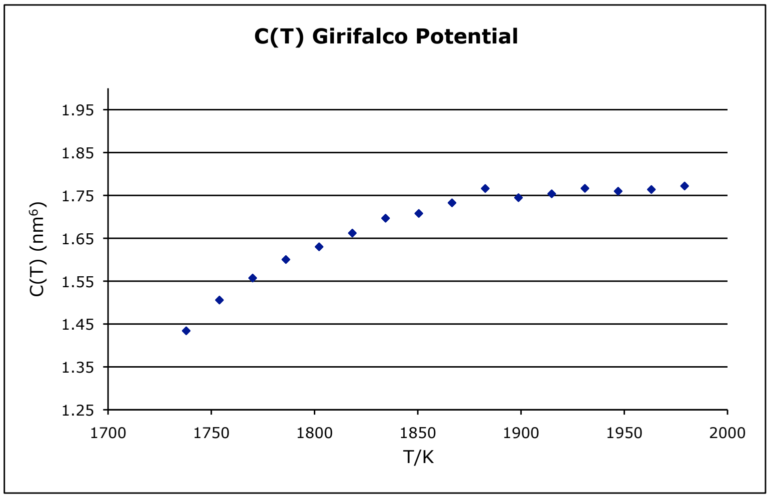

Figure 4.4 – The third virial coefficient for the Girifalco potential in nm^6 calculated by Mayer sampling.

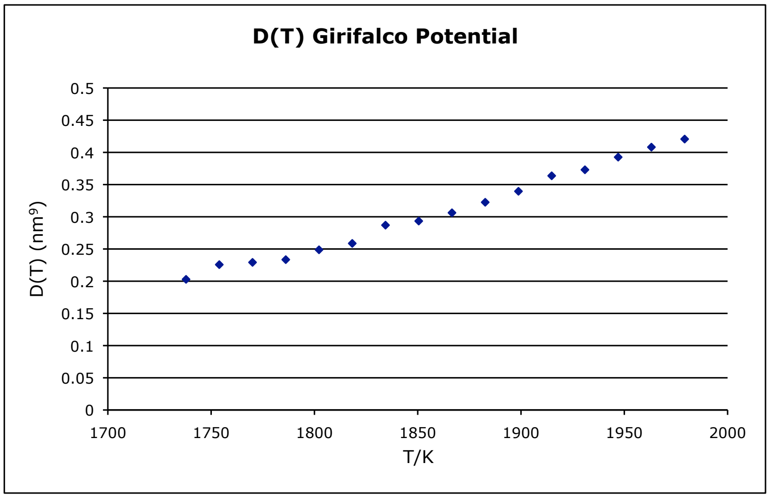

Figure 4.5 – The fourth virial coefficient for the Girifalco potential in nm^9 calculated by Mayer sampling.

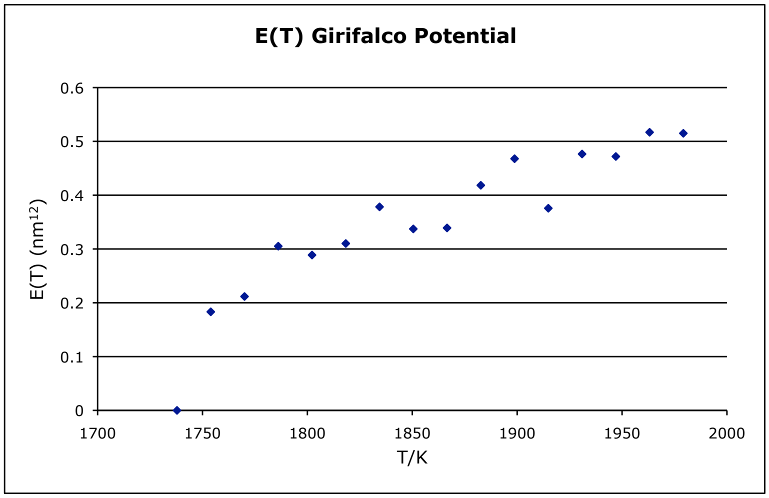

Figure 4.6 – The fifth virial coefficient for the Girifalco potential in nm^{12} calculated by Mayer sampling.

All calculations were done over multiple simulations with a sampling size from 10^8 to 10^9, and had data averaged as described in section 4.1. The coefficients were used to produce coexistence data from the Maxwell construction described in chapter 3. Figures 4.7 and 4.8 show the isotherms used for the Maxwell construction plotted as pressure vs. density and pressure vs. volume respectively. Figure 4.9 shows the liquid vapor coexistence predicted by the virial expansion truncated at D(T), E(T) and using the [2/2] Padé approximant from E(T) data.

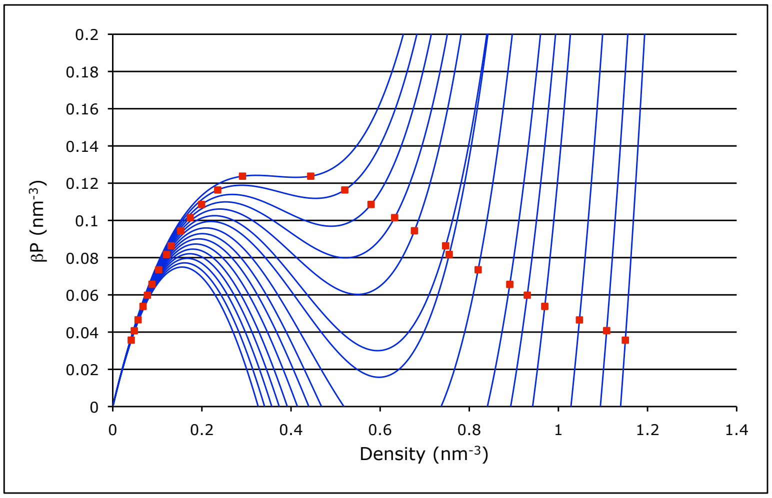

Figure 4.7 – Isotherms for the Girifalco potential predicted by Mayer sampling up to E(T) graphed as pressure vs. density. Red squares are the coexistence points calculated by Maxwell construction.

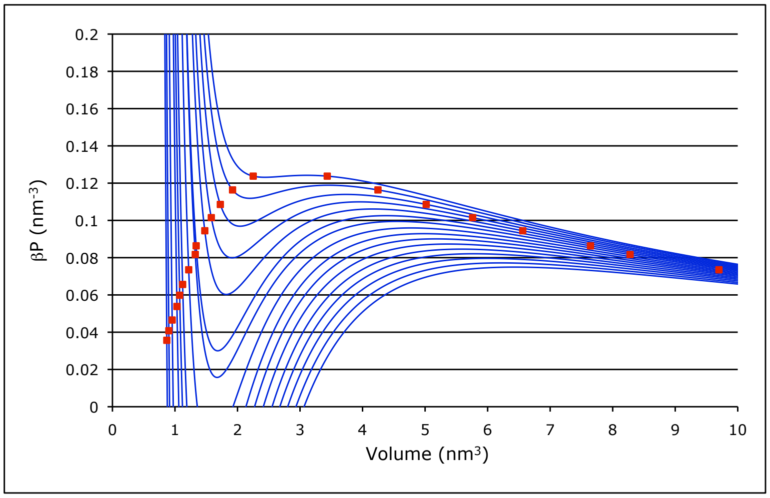

Figure 4.8 – Isotherms for the Girifalco potential predicted by Mayer sampling up to E(T) graphed as pressure vs. volume. Red squares are the coexistence points calculated by Maxwell construction.

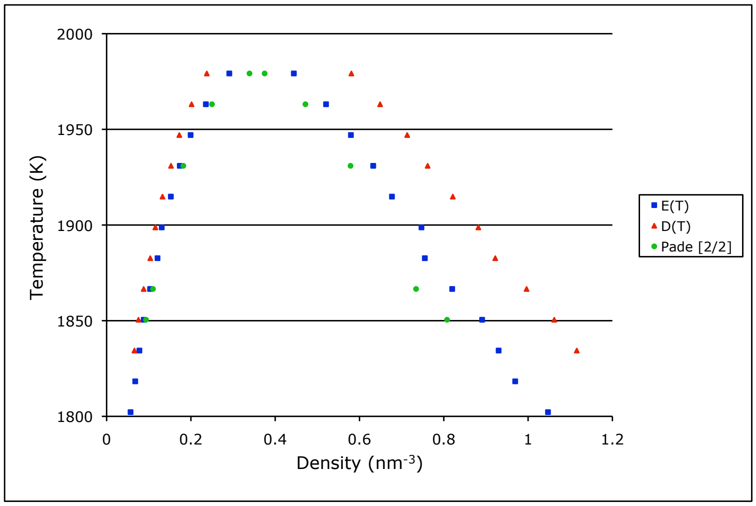

Figure 4.9 – Liquid-vapor coexistence points obtained through Maxwell construction for the Girifalco potential using the virial expansion truncated at D(T), E(T) and a [2/2] Padé approximant.

The virial expansion over estimates the critical point when compared to literature values[22-29] from 1798 – 1976. The critical point is lowered closer by adding E(T) and lowered further by using a Padé approximant as can be seen in the isotherm at T = 1930 K in figures 4.10 and 4.11. The isotherm is closest to the critical point for the Padé [2/2] fluid because the loops are tighter, followed by the virial expansion truncated at E(T) and then at D(T).

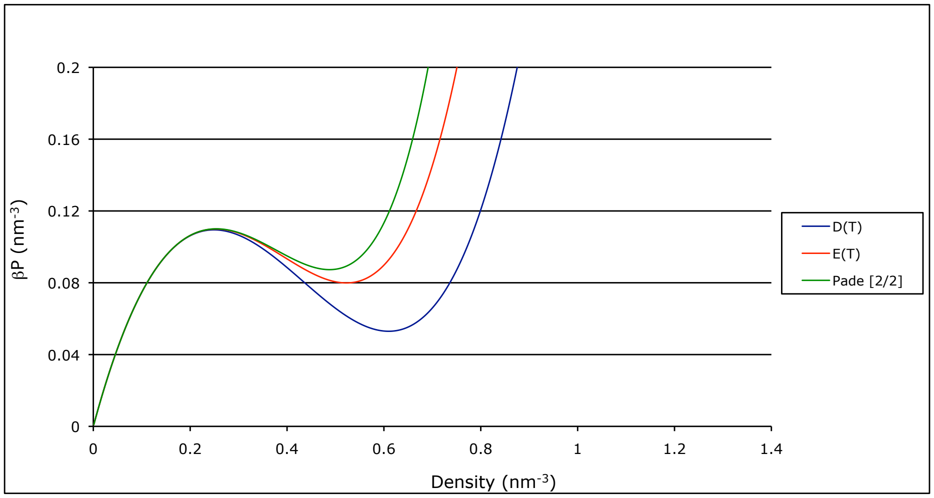

Figure 4.10 – Pressure vs. density isotherm at 1930 K for three approximations.

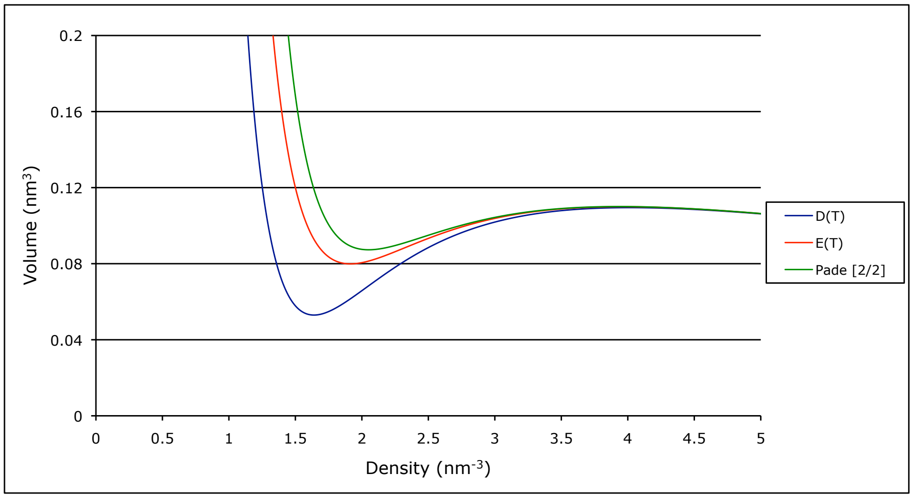

Figure 4.11 – Volume vs. density isotherm at 1930 K for three approximations.

The values calculated for the second virial coefficient were also used to calculate square well parameters to model the Girifalco potential by the method described in section 3.3 (see Figure 4.12). In section 3.3 all B(T) data available for argon was used to choose a well width. Because we are modeling another potential, B(T) at any temperature can be calculated through Mayer sampling and incorporated. However, the square-well potential is incapable of modeling a system for all temperatures (zero to infinity) because of the infinitely repulsive hard core. At extremely high temperatures ($\varepsilon/k \ll T$) the kinetic energy of the system should allow particles to overlap some of the repulsive parts of the potential, essentially contracting the repulsive core. A choice must be made as to which temperatures B(T) values should be matched to. Unless a specific temperature range is of interest, it was found that the best choice is approximately .75 T_c – 4 T_c, where T_c is the critical temperature. The optimal parameters for the Girifalco potentials were found to be λ = 1.333, ε/k = 2059 K and σ = 0.9309 nm. Figures 4.13 and 4.14 compare the Girifalco potential with this square-well model for u(r) and f(r) at 1950 K, respectively.

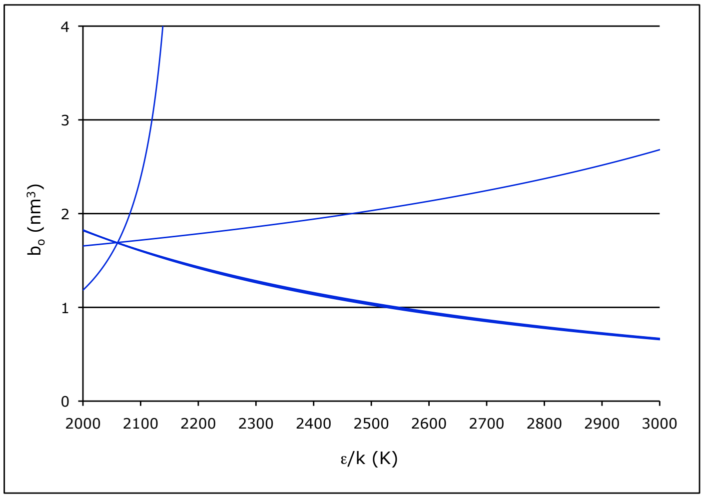

Figure 4.12 – Values for b_0 of the square well model that match B(T) values of the Girifalco potential given ε/k at λ = 1.333 at T = 1738, 1850, 1867, 1899, 2000, 4000, and 8000 K.

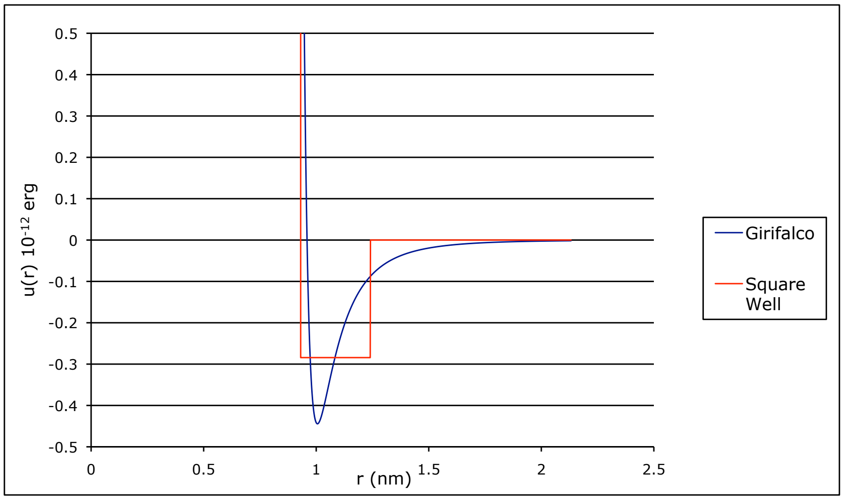

Figure 4.13 – Pair potential for the Girifalco potential and as modeled by the square-well potential.

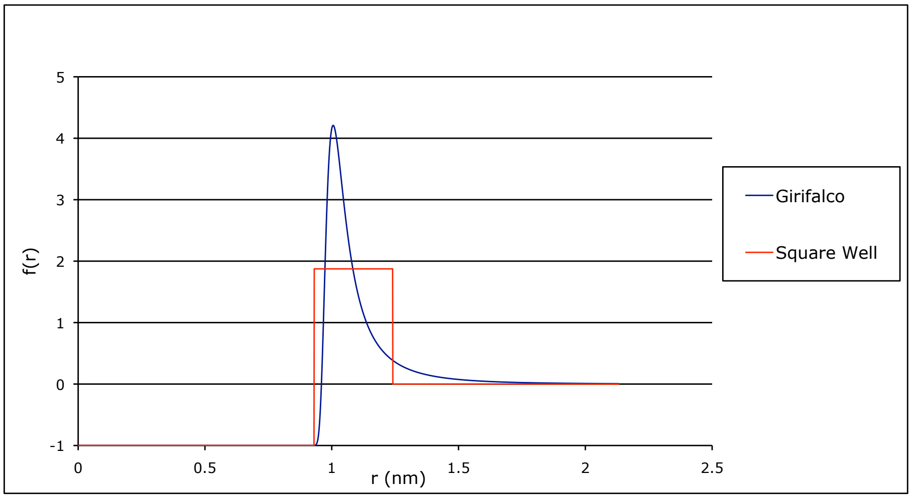

Figure 4.14 – Mayer f-bond for Girifalco potential and the square well model at T = 1950 K.

Coexistence data was also calculated for the square-well model using a Maxwell construction. Because the solution for the square-well potential is independent of temperature, a full coexistence curve can be calculated as opposed to coexistence data only being calculated only at isotherms that simulations were run at, as is the case in figure 4.9. Coexistence data from several virial expansions are displayed in figure 4.15. The critical point here is predicted below the ones found in literature.

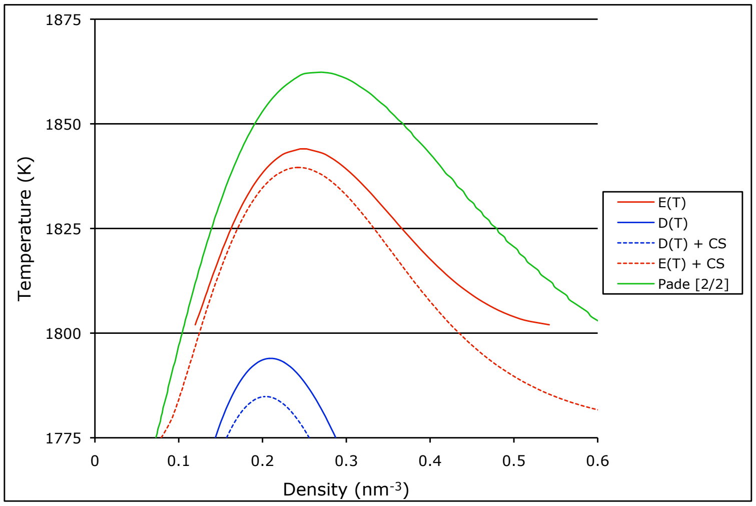

Figure 4.15 – Coexistence curves for several virial expansions, including Padé approximation, for the square-well model of the Girifalco potential.

Again it is seen that including E(T) brings the predicted critical point closer to literature values and it is brought closer still with a Padé approximation. This can be seen from the isotherms in figure 4.16, not that at T = 1850 K all fluids are supercritical except the Padé [2/2] approximant. In figure 4.15 D(T) + CS and E(T) + CS indicate equations of state completed by using higher order terms from the Carnahan Starling equation as described in section 3.2, although this seems to move the critical point lower away from literature values.

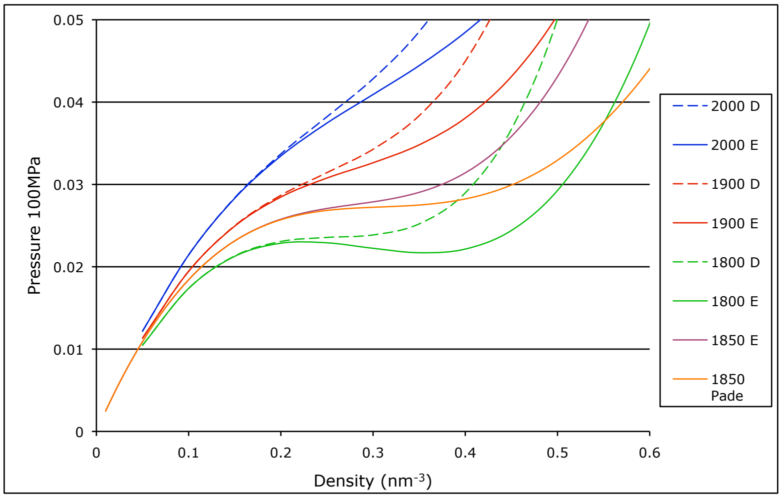

Figure 4.16 – Isotherms for different virial expansions of the square-well modeling the Girifalco potential.

As stated in section 3.3, the accuracy of the coexistence curves are severely limited because they rely on both low- and high-density data and high-density is susceptible to error when using a truncated virial expansion. Comparing the low density pressures calculated from truncated virial expansions to the coexistence pressures from [21] (where we use their values for density, but predict the pressure) both truncated virial expansions at E(T) for the Girifalco potential and the square-well model show good agreement figure 4.17. Higher temperatures correspond to higher densities, and so there is some disagreement at $T - T_c$.

The virial coefficients for the Girifalco potential have been calculated up to E(T) for several temperatures in the range of the of the critical temperature. The truncated virial expansion at E(T) shows good agreement at lower densities with literature data. Using the method discussed in section 3.3, the Girifalco potential was modeled with a square-well potential. The truncated virial expansion at E(T) for the square-well model also shows good agreement at low temperatures with available literature data and has the added advantage of being applicable to all temperatures after just one simulation per virial coefficient. Both virial expansions were improved from the use of Padé approximants. The accuracy of the virial coefficients used could be increased with more sampling, and the accuracy of the virial expansion and especially the Padé approximants could be increased with the addition of higher order coefficients.

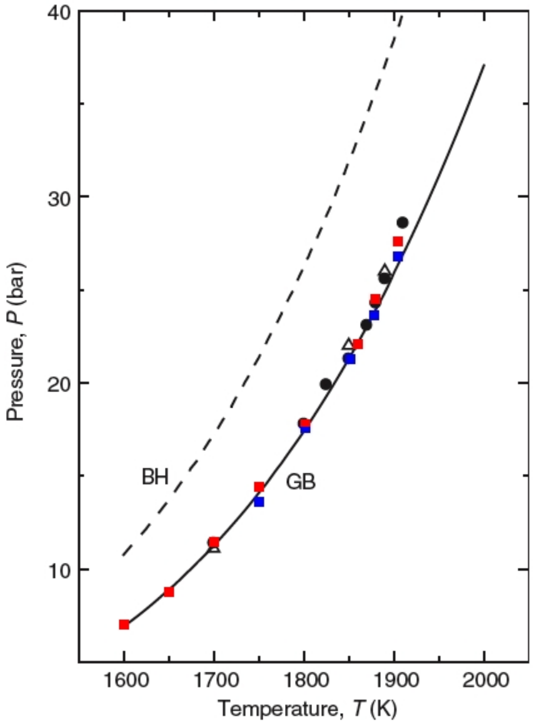

Figure 4.17 – Coexistence pressure vs. temperature from Barker-Henderson perturbation theory (BH), Gibbs-Bogoliubov variational method (GB), Monte Carlo simulation (N = 600 black circles, N = 1500 white triangles), virial expansion truncated at E(T) for the Girifalco potential (blue squares), and virial expansion truncated at E(T) for the square-well potential (red squares).

4.4 C$_{60}$ POTENTIALS – SMITH-THAKKAR

Another pair potential to model[30] the C60 fullerene has been proposed to replace the Girifalco model discussed in section 4.3. As stated in [30] a significant problem with the Girifalco potential is that it behaves unrealistically in the repulsive region when r < 7.1nm, even becoming negative. Because this represents the overlap of two fullerenes it should be greatly repulsive (positive). This may not interfere with molecular dynamic or Monte Carlo simulations because this interparticle distance is sterically hindered by an asymptotic increase as $r \to .71^+$. This is not the case for virial coefficients calculated from integration or Mayer sampling. In section 4.3 the Girifalco potential was assumed to be the piecewise function (where $u(r)_G$ is the original Girifalco potential):

$$u(r) = \begin{cases} \lim_{r \to .71^+} u(r)_G & r \le .71 \\ u(r)_G & r > .71 \end{cases} \tag{4.4.1}$$

To solve this problem the authors of [30] have used enthalpy of sublimation, lattice constant and compressibility of the face-centered cubic crystal for the C_{60} molecule to construct a pair potential of Smith-Thakkar type. The general Smith-Thakkar[31] potential is:

$$u(r) = \begin{cases} \frac{A}{(r^2-d^2)^6} - \frac{B}{(r^2-d^2)^3} & r > d \\ \infty & r \leq d \end{cases} \tag{4.4.2}$$

From the experimental data it was determined that A = 352.48, B = 6262.60, d = .7258, and u(r) is in J mol^{-1} and r is in nm. This will be referred to as the Smith-Thakkar potential from here. The Smith-Thakkar potential has a slightly lower minimum potential and shorter node compared to the Girifalco potential. The two potentials are compared in figure 4.18.

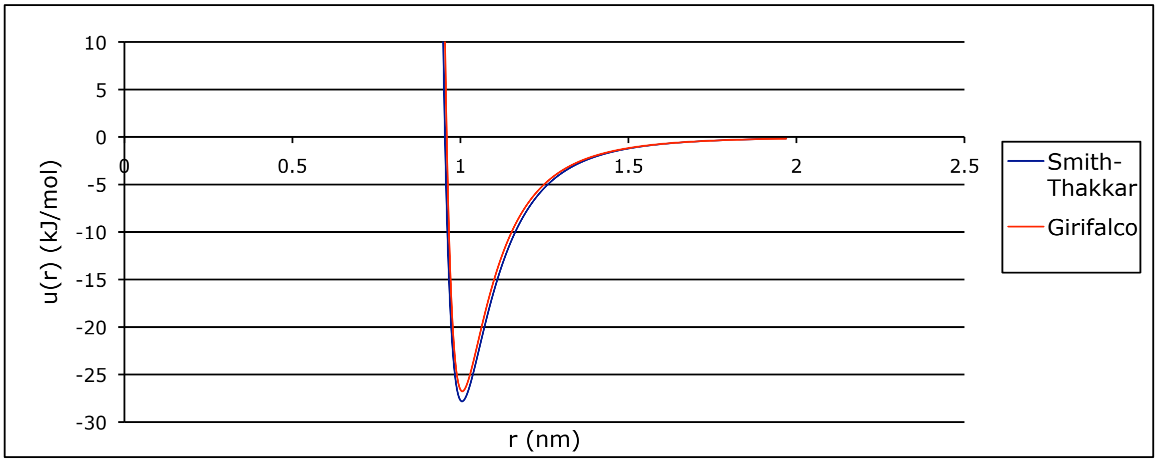

Figure 4.18 – Pair potential for Girifalco and Smith-Thakkar potentials.

Like Girifalco, authors of [30] also calculated the second virial coefficient in but again it disagrees with numerical integration done in Maple and Mayer sampling. The results are presented in table 4.2 in the original units of [30] (-B(T)/cm^3 mol^{-1}).

Liu, Wang[30]		Maple		Mayer Sampling	
T	B(T)	T	B(T)	T	B(T)
490	226,931	490	227406	490	226794.6345
500	200,772	500	201249	500	201975.9454
510	178,535	510	179012	510	180456.5847
520	159,520	520	159998	520	159265.3983
540	129,044	540	129523	540	129361
560	106,067	560	106547	560	106375
580	88,427	580	88907	580	89270.3
600	74,659	600	75140	600	75227.6
650	51,258	650	51740	650	51644.2
700	37,171	700	37653	700	37922.5
750	28,129	750	28611	750	28662.1
800	22,017	800	22499	800	22518.5
850	17,706	850	18188	850	18163.3
900	14,554	900	15037	900	15019.3
950	12,182	950	12664	950	12631.8
1000	10,349	1000	10831	1000	10817.4
1050	8902	1050	9384	1050	9376.41
1100	7737	1100	8219	1100	8230.51
1150	6785	1150	7267	1150	7273.97
1200	5994	1200	6477	1200	6480.7
1250	5330	1250	5812	1250	5812.84
1300	4766	1300	5248	1300	5256.2
1400	3861	1400	4343	1400	4339.97
1500	3172	1500	3654	1500	3650.57
2000	1300	2000	1782	2000	1781.461753
2500	480	2500	962	2500	960.9043986
3000	26.7	3000	508	3000	507.988179
3038	0.5	3038	482	3038	482.08822
3039	-0.2	3039	481	3039	481.248799
4000	-454	4000	25.1	4000	25.195478
		4077	0.2	4077	-0.043033
		4078	-0.08	4078	-0.235416
		4500	-118	4500	-117.726775

Table 4.2 – B(T) calculation results for the Smith-Thakkar potential using Maple and Mayer sampling compared to those from reference [30] where the values listed are –B(T) cm^3/mol.

Mayer sampling was also performed for C(T), D(T) and E(T) for temperatures from 1750 K to 2000 K. All calculations were done over multiple simulations with a sampling size from 10^8 to 10^9, and had data averaged as described in section 4.1. The results are shown in figures 4.19 – 4.22.

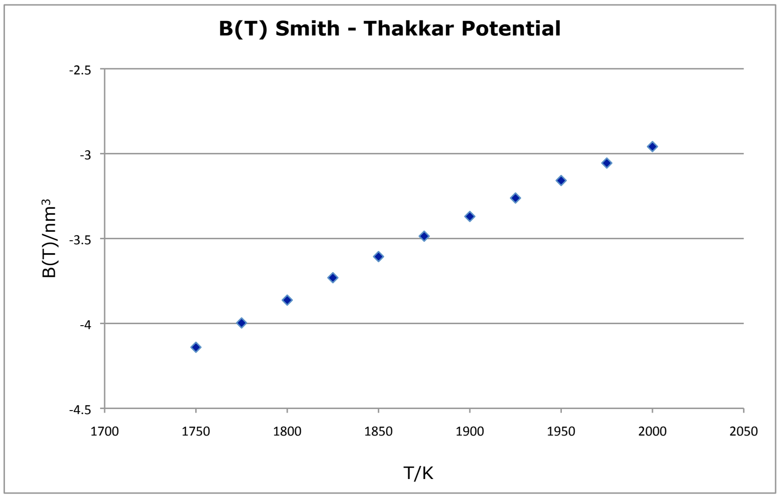

Figure 4.19 – Second virial coefficient for the Smith – Thakkar potential calculated by Mayer Sampling.

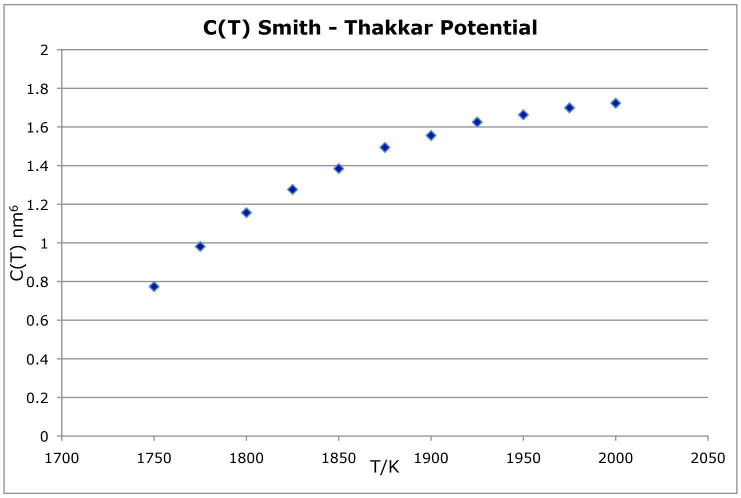

Figure 4.20 - Third virial coefficient for the Smith – Thakkar potential calculated by Mayer Sampling.

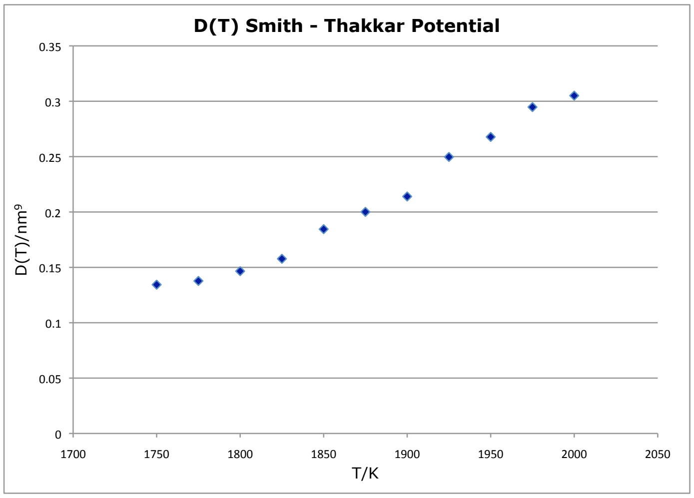

Figure 4.21 - Fourth virial coefficient for the Smith – Thakkar potential calculated by Mayer Sampling.

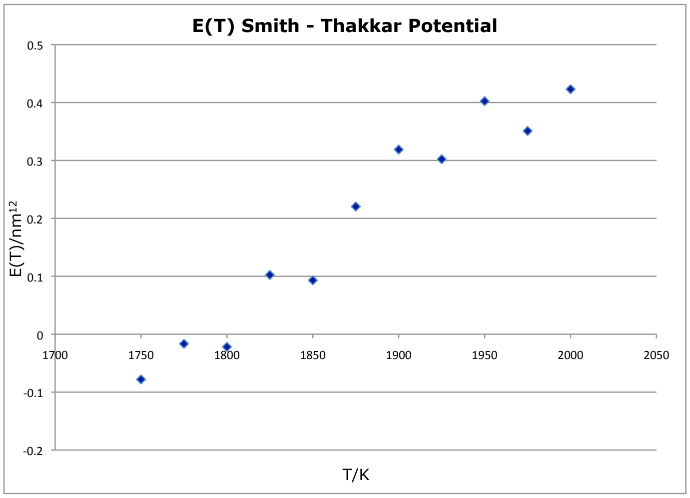

Figure 4.22 - Fifth virial coefficient for the Smith – Thakkar potential calculated by Mayer Sampling.

As with the Girifalco potential, the coefficients were used to produce coexistence data from the Maxwell construction described in chapter 3. Figures 4.23 and 4.24 show the isotherms used for the Maxwell construction plotted as pressure vs. density and pressure vs. volume respectively with E(T) predicted coexistence points. Figure 4.25 shows the liquid vapor coexistence predicted by the virial expansion truncated at D(T), E(T) and using the [2/2] Padé approximant from E(T) data.

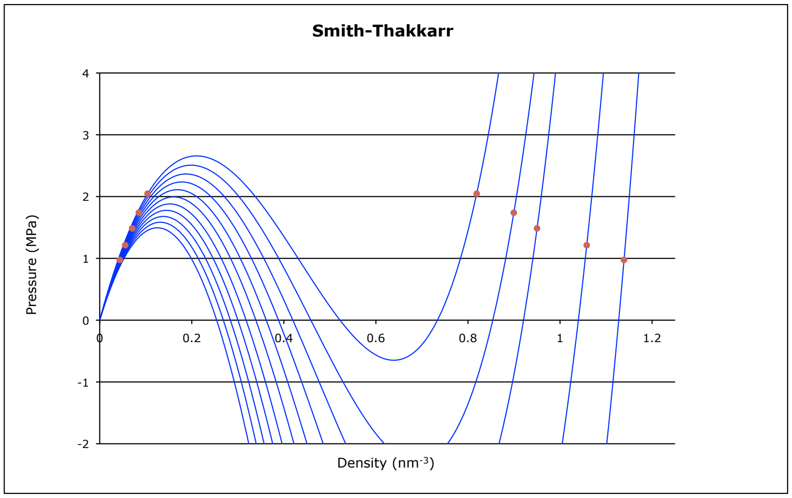

Figure 4.23 – Isotherms for the Smith - Thakkar potential predicted by Mayer sampling up to E(T) graphed as pressure vs. density. Red squares are the coexistence points calculated by Maxwell construction.

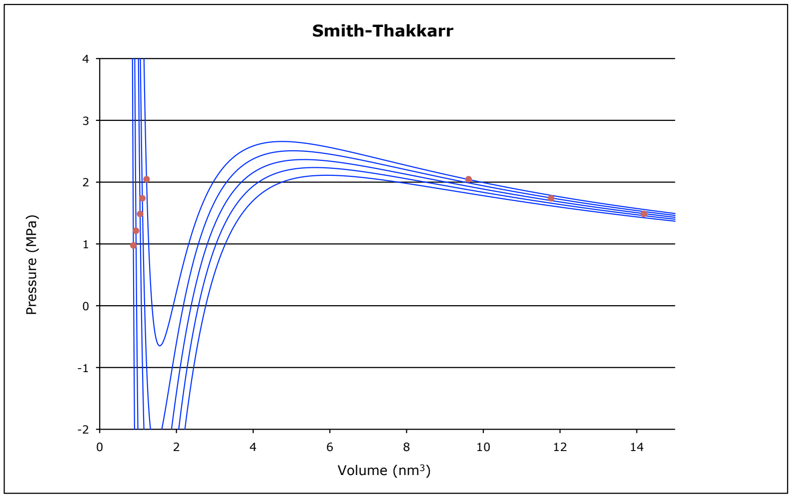

Figure 4.24 – Isotherms for the Smith - Thakkar potential predicted by Mayer sampling up to E(T) graphed as pressure vs. volume. Red squares are the coexistence points calculated by Maxwell construction.

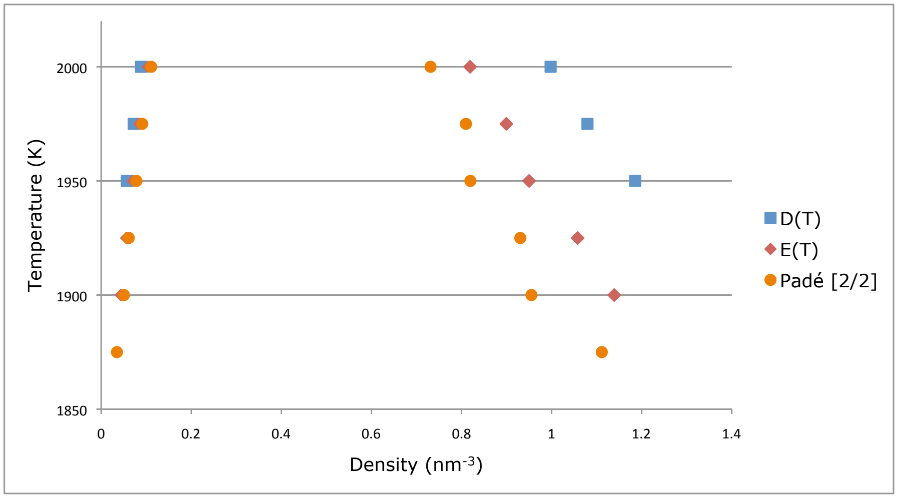

Figure 4.25 – Liquid-vapor coexistence data predicted from several equations of state derived from Mayer sampling.

The critical temperatures predicted from the virial expansions of the Smith - Thakkar potential are higher than those predicted from the Girifalco potential. Again the critical temperatures predicted from low to high are in the order Padé [2/2], E(T), and D(T). Unfortunately unlike the Girifalco potential there has been no simulations done to compare results with. This also leaves us with no way to determine if the Girifalco and Smith – Thakkar coexistence curves should be consistent, although a depressed $u(r)_{min}$ for the Smith – Thakkar potential could raise the critical temperature (by lowering the ratio T : ε/k). Ideally there would be both computer simulation of the Smith – Thakkar potential and experimental coexistence curves for C_{60} to determine which potential better approximates the liquid-vapor line.

As with the Girifalco potential, the Smith – Thakkar potential was approximated with the square-model using the method of matching B(T) data from Mayer sampling with the exact square-well B(T) values as described in section 3.3. Again, because we can predict the Smith – Thakkar B(T) at any temperature and the square-well model behaves unnaturally across a large temperature range we choose B(T) data from 1500 K – 4500 K. The resulting parameters are $\lambda = 1.333$, $\varepsilon/k = 2237$ K, $\sigma = 0.9205$ nm (note this is the same well width chosen for the Girifalco potential). The plot used to choose these parameters is figure 4.26. The u(r) and f(r) at T = 1950 predicted by this potential are compared to the Smith – Thakkar, Girifalco, and Girifalco square-well potentials in figures 4.27 and 4.28, respectively.

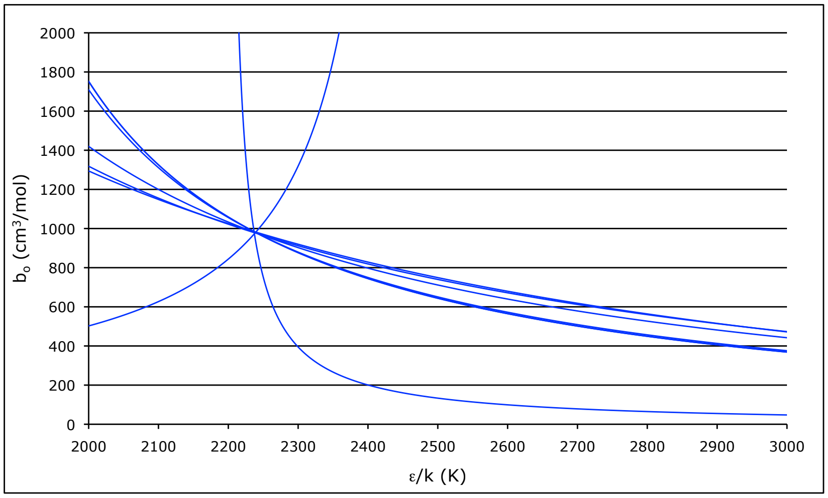

Figure 4.26 – Values for b_0 for a square-well potential with a well-width of 1.333 that match B(T) data for the Smith – Thakkar potential plotted against the well depth.

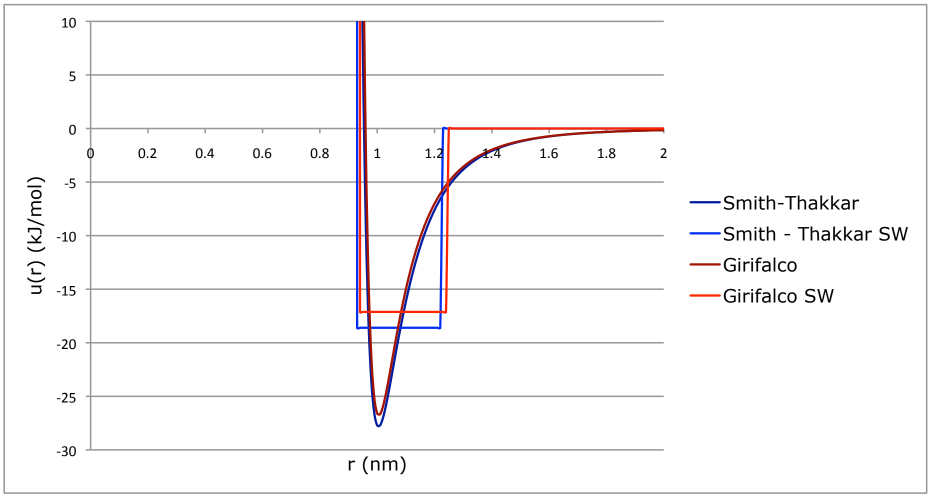

Figure 4.27 – Pair potential models for the C_{60} fullerene.

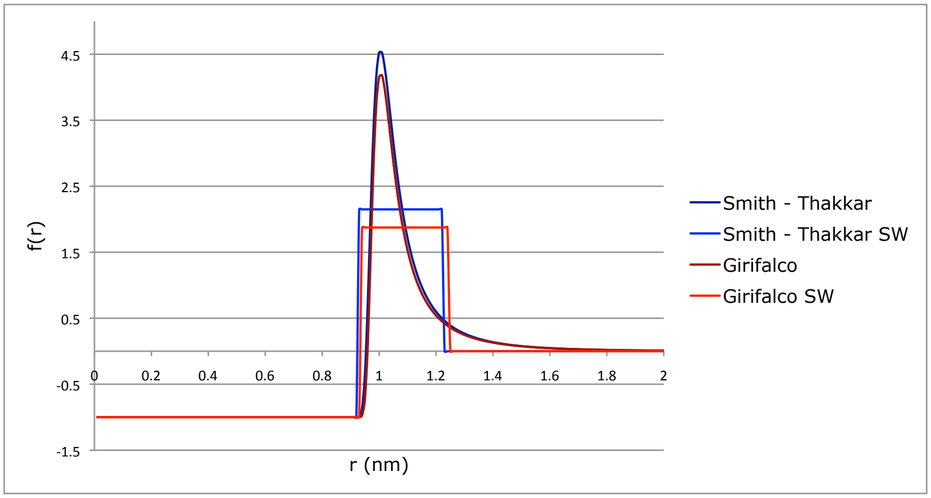

Figure 4.28 – Mayer F-bonds for the C_{60} fullerene models at T = 1950 K.

The same ratio integration results for the Girifalco square-well model can be reused here because they have the same well widths. Coexistence curves were calculated for the square-well model derived from the Smith - Thakkar potential using a Maxwell construction with results in figure 4.29. Again this was done at all temperatures with no addition simulations. Because the well widths are the same for the Girifalco and Smith-Thakkar potentials the predicted phase diagrams are the same on a reduced units scale ($T^* = kT/\varepsilon$, $\rho = \rho\sigma^3$). The square-well coexistence curves are again below the ones predicted by performing a Maxwell construction on the Mayer sampling results.

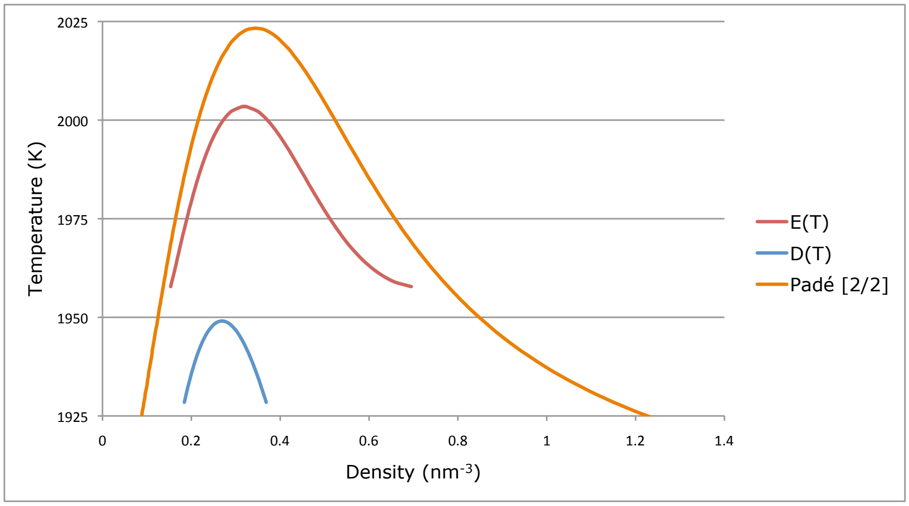

Figure 4.29 – Liquid-vapor coexistence curves predicted by the square-well potential modeling the Smith-Thakkar potential of the C_{60} fullerene calculated from the Maxwell construction method.

References

[1] Singh, J. K., Kofke, D. A., 2004, *Phys. Rev. Lett.*, **92**, 220601-1.

[2] Benjamin, K. M., Singh, J. K., Schultz, A. J., Kofke, D. A., 2007, *J. Phys. Chem. B*, **111**, 11463.

[3] Rosch, T. W., Errington, J. R., 2007, *J. Phys. Chem. B*, **111**, 12591.

[4] Benjamin, K. M., Schultz, A. J., Kofke, D. A., 2007, *J. Phys. Chem. C*, **111**, 16021.

[5] Naresh, D. J., Singh, J. K., 2009, *Fluid Phase Equilib.*, **279**, 47.

[6] Naresh, D. J., Singh, J. K., 2009, *Fluid Phase Equilib.*, **285**, 36.

[7] Monago, K. O., 2010, *Can. J. Chem. Eng.*, 2010, **88**, 55.

[8] Kwak, S. K., Kofke, D. A., 2005, *J. Chem. Phys.*, **122**, 104508.

[9] Chen, W. W., Kwak, S. K., 2009, *Mol. Phys.*, **107**, 2213.

[10] Girifalco, L. A., 1991, *J. Phys. Chem.*, **95**, 5370.

[11] Nowak, P., Kleinrahm, R., Wagner, W., 1997, *J. Chem. Thermodyn.*, **29**, 1137.

[12] Funke, M., Kleinrahm, R., Wagner, W., 2002, *J. Chem. Thermodyn.,* **34**, 2001.

[13] Monago, K. O., 2010, *Can. J. Chem. Eng.*, **88**, 55.

[14] Masters, A. J., 2008, *J. Phys. Condens. Matter*, **20**, 283102.

[15] Rosch, T. W., Errington, J. R., 2007, *J. Phys. Chem. B*, **111**, 12591.

[16] Schultz, A. J., Kofke, D. A., 2009, *Mol. Phys.*, **107**, 1431.

[17] Schultz, A. J., Kofke, D. A., 2009, *Mol. Phys.*, **107**, 2309.

[18] Kroto, H. W., Heath, J. R., O'Brien, S. C., Curl, R. F., Smalley, R. E., 1985, *Nature*, **318**, 162.

[19] Girifalco, L. A., 1991, *J. Phys. Chem.*, **95**, 5370.

[20] Girifalco, L. A., 1992, *J. Phys. Chem.*, **96**, 858.

[21] Osman, S. M., Bahaa Khedr, M., 2009, *Phys. Chem. Liq.*, **47**, 564.

[22] Hagen, M. H. J., Meijer, E. J., Mooij, G. C. A. M., Frenkel, D., Lekkerkerker, H. N. W., 1993, *Nature*, **365**, 425.

[23] Cheng, A., Klein, M. L., Caccamo, C., 1993, *Phys. Rev. Lett.*, **71**, 1200.

[24] Caccamo, C., Costa, D., Fucile, A., 1997, *J. Phys. Condens. Matter*, **106**, 255.

[25] Broughton, J. Q., Lill, J. V., Johnson, J. K., 1997, *Phys. Rev. B*, **55**, 2808.

[26] Caccamo, C., 1995, *Phys. Rev. B*, **51**, 3387.

[27] Hasegawa, M., Ohno, K., 1996, *Phys. Rev. E*, **54**, 3928.

[28] Hasegawa, M., Ohno, K., 1999, *J. Chem. Phys.*, **111**, 5955.

[29] Costa, D., Pellicane, G., Caccamo, C., Schöll-Paschinger, E., Kahl, G., 2003, *Phys. Rev. E*, **68**, 021104.

[30] Lui, F. L., Wang, J., 2006, *J. Mol. Struct.*, **778**, 105.

[31] Smith, V. H., Thakkar, A. J., 1972, *Chem. Phys. Lett.*, **17**, 274.

Chapter 5
Future Research

5.1 STICKY SPHERES

Large macromolecules such as colloids or proteins have similar attractive forces as smaller molecules but with much larger repulsive diameters. When modeling these forces with the square-well potential, the well-width is dramatically reduced since the length of attraction ($\lambda\sigma - \sigma$) remains the same while the hard-core diameter is increased (5.1.1 – 5.1.3).

$$\sigma_1 << \sigma_2 \tag{5.1.1}$$

$$\lambda_1\sigma_1 - \sigma_1 = \lambda_2\sigma_2 - \sigma_2 \tag{5.1.2}$$

$$\therefore \lambda_1 - 1 >> \lambda_2 - 1 \tag{5.1.3}$$

A common method for approximating macromolecules with the square-well potential is to use a very deep, very narrow well[1]. The limit of this potential is the Baxter sticky sphere[2]. Introduced by Baxter in 1968 and extensively studied since, the Baxter stick sphere model has a hard-core with an infinitely deep and infinitely narrow square-well. A remaining question has been if and how the thermodynamics of the Baxter sticky-sphere system is approached as the square-well potential is narrowed and deepened; an interesting feature of which is the disappearance of the liquid – vapor coexistence curve[3].

To explore this, ratio integration was performed on decreasing well-widths. Coexistence curves were constructed using Maxwell's equal area law using the virial expansion truncated at E(T) and augmented with the Carnahan Starling equation of state. As in section 3.2, the depth at each well-width is set by matching B(T) to a reference system at its critical point, with reference values λ = 1.85, ε/k = 69.4, and T_c = 151K. Results are plotted in figures 5.1 and 5.2.

As the well-width decreases, the coexistence curves flatten out and the critical point is pushed to a lower T* (although T remains in the same region because of the well's deepening). The next step would be to solve the solid state with a perturbation method and determine the solid-fluid coexistence curve. If the liquid-vapor coexistence curve is low enough, the solid-vapor curve will be above it; effectively eliminating the liquid phase. This has been discussed for the C_{60} model in Nature[4]. These results also need to be compared to the thermodynamics of the Baxter sticky sphere model.

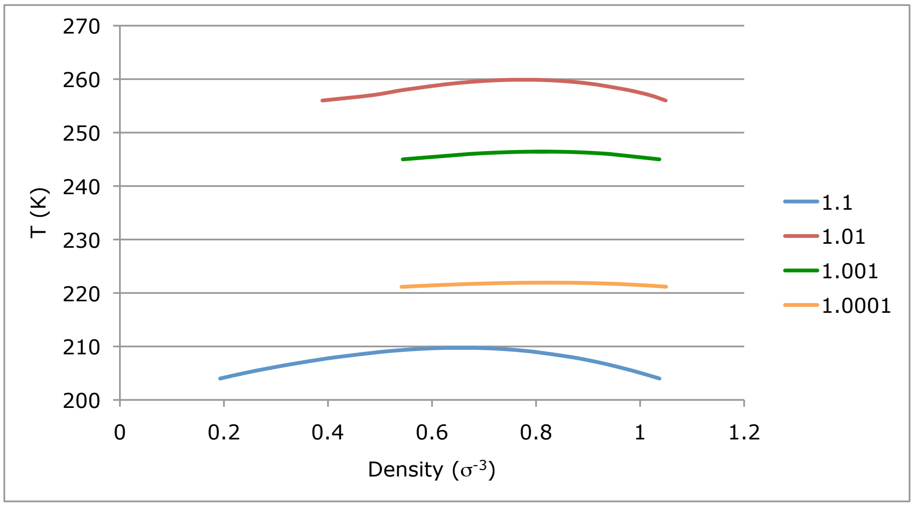

Figure 5.1 – Coexistence curves for the square-well model.

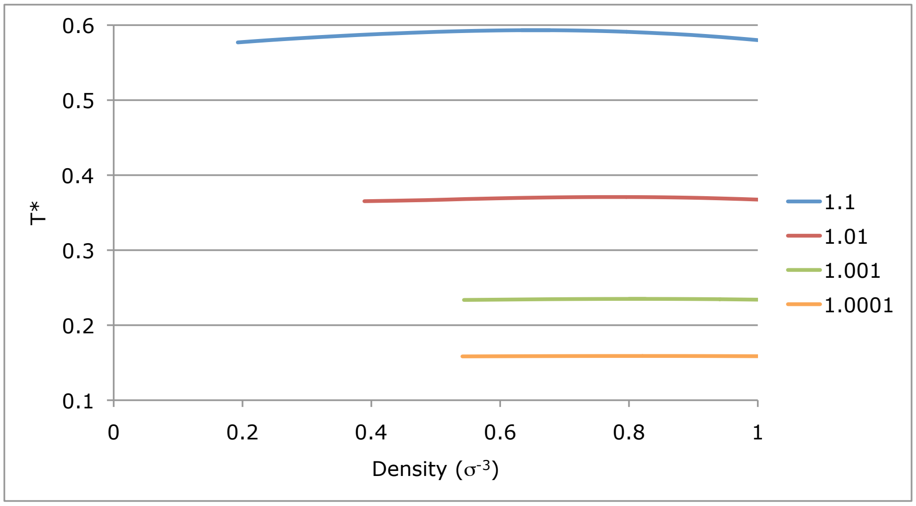

Figure 5.2 – Coexistence curves for the square-well model.

5.2 FUTURE SQUARE-WELL RESEARCH

Ratio integration has been performed for $D_3(T)$ and E(T) in this work. More simulations would increase the values obtained. Higher order virial coefficients could be calculated and increase the accuracy of the truncated virial expansion, especially when using Padé approximants. Generating higher order virial coefficients is necessary to determine if the series converges.

A technique for using the square-well potential to model real systems and other potentials was developed in section 3.3. This needs to be tested and compared to more systems to determine its accuracy. Its usefulness lies with its economy of parameters and simulations; however more optimization is needed for it to find practical usefulness.

In section 3.5 the square-well was used to model binary mixtures. No further generalization is needed to study mixtures with more components, but the accuracy of the square-well model for such systems needs to be tested.

The square-well model along with Mayer sampling can be used to test the accuracy of other potential models and generate new thermodynamic data in the same way as was done in chapter 4 for the Girifalco and Smith-Thakkar potentials. One model of particular interest is the Derjaguin/Landau-Verwey/Overbeek (DLVO) model of colloidal systems, for which Mayer sampling has already been used on to generate B(T) data[5].

Virial coefficients in dimensions greater than d = 3 have been calculated for the hard sphere potential. Using these results and ratio integration it is possible to calculate virial data for the square-well potential in the same manner as discussed in chapter 2 for the three-dimension case.

Perhaps the greatest potential for further research is finding an application that can benefit from the simplicity, accuracy, speed, and flexibility of this modeling technique.

Chapter 5 References

[1] Tang, Y. P., 2007, *J. Chem. Phys.*, **127**, 164504.

[2] Baxter, R. J., 1968, *J. Chem. Phys.*, **49**, 2770.

[3] Noro, M. G., Frenkel, D., 2000, *J. Chem. Phys.*, **113**, 2941.

[4] Hagen, M. H. J., Meijer, E. J., Mooij, G. C. A. M., Frenkel, D., Lekkerkerker, H. N. W., 1993, *Nature*, **365**, 425.

[5] Rosch, T. W., Errington, J. R., 2007, *J. Phys. Chem. B*, **111**, 12591.

References

Boltzmann L 1899 *Proc. Sect. Sci. K. Acad. Wet., Amsterdam* **7** 484

Hauge E. H. 1965 PhD Thesis Trondheim, Norway

Boltzmann 4th Virial for Hard Spheres

Barker, J. A., and Monaghan, J. J., 1962, *J. Chem. Phys.*, **36**, 2558.

Hauge, E. H., 1963, *J. Chem. Phys.*, **39**, 389.

Katsura, S., 1958, *Phys. Rev.*, **115**, 1417.

Ree, F. H., Hoover, W. G., 1964, *J. Chem. Phys.*, **40**, 939.

Vlasov, A. Y., You, X. M., Masters, A. J., 2002, *Mol. Phys.*, **100**, 3313.

Sevick, E. M., Monson, P. A., 1991, *J. Chem. Phys.*, **94**, 3070.

Hussein, N. A. R., Ahmed, S. M., 1991, *J. Phys. A: Math. Gen.*, **24**, 289.

Naresh, D. J., Singh, J. K., 2009, *Fluid Phase Equilib.*, **279**, 47.

Singh, J. K., Kofke, D. A., 2004, *Phys. Rev. Lett.*, **92**, 220601-1.

Kratky, K. W., 1976, *Physica A*, **85**, 607.

Maxwell, J. C., 1965 (c1890), *The Scientific Papers of James Clerk Maxwell*, Dover, 424.

Hirschfelder, J. O., Curtiss, C. F., Bird, R. B., 1966, *Molecular Theory of Gases and Liquids*, (John Wiley & Sons, New York).

Gilgen, R., Kleinrahm, R., Wagner, W., 1994, *J. Chem. Thermodyn.*, **26**, 383.

Bokis, C. P., Donohue, M. D., Hall, C. K., 1994, *Ind. Eng. Chem. Res.*, **33**, 146.

Michels, A., DeGraaff, W., Ten Seldham, C. A., 1960, *Physica*, **26**, 393.

Dymond, J. H., Smith, E. B., 1980, *The Virial Coefficients of Pure Gases and Mixtures*, (Clarendon Press, Oxford).

Tegler, C., Span, R., Wagner, W., 1999, *J. Phys. Chem. Ref. Data.*, **28**, 779.

Clisby, N., McCoy, B. M., 2006, *J. Stat. Phys.*, **122**, 15.

Guerrero, A. O., Bassi, A. B. M. S., 2008, *J. Chem. Phys.*, **129**, 044509.

Monago, K. O., 2010, *Can. J. Chem. Eng.*, **88**, 55.

Estela-Uribe, J. F., Jeramillo, J., Salazar, M. A., Trusler, J. P. M., 2003, *Fluid Phase Equilib.*, **204**, 169.

Jaeschke, M., Audibert, S., van Caneghem, P., Humphreys, A. E., Janssen-van Rosmalen, R., Pellei, Q., Michels, J. P. J., Schouten, J. A., ten Seldam, C. A., 1989, *High accuracy compressibility factor calculation for natural gases and similar mixtures by use of a truncated virial equation*, (GERG Technical Monograph TM 2).

Dymond, J. H., Smith, E. B., 1980, *The Virial Coefficients of Pure Gases and Mixtures*, (Clarendon Press, Oxford).

Kihara, T., 1953, *Rev. Mod. Phys.*, **25**, 831.

Kihara, T., 1955, *Rev. Mod. Phys.*, **27**, 412.

Kroto, H. W., Heath, J. R., O'Brien, S. C., Curl, R. F., Smalley, R. E., 1985, *Nature*, **318**, 162.

Singh, J. K., Kofke, D. A., 2004, *Phys. Rev. Lett.*, **92**, 220601-1.

Benjamin, K. M., Singh, J. K., Schultz, A. J., Kofke, D. A., 2007, *J. Phys. Chem. B*, **111**, 11463.

Rosch, T. W., Errington, J. R., 2007, *J. Phys. Chem. B*, **111**, 12591.

Benjamin, K. M., Schultz, A. J., Kofke, D. A., 2007, *J. Phys. Chem. C*, **111**, 16021.

Naresh, D. J., Singh, J. K., 2009, *Fluid Phase Equilib.*, **279**, 47.

Naresh, D. J., Singh, J. K., 2009, *Fluid Phase Equilib.*, **285**, 36.

Monago, K. O., 2010, *Can. J. Chem. Eng.*, 2010, **88**, 55.

Kwak, S. K., Kofke, D. A., 2005, *J. Chem. Phys.*, **122**, 104508.

Chen, W. W., Kwak, S. K., 2009, *Mol. Phys.*, **107**, 2213.

Girifalco, L. A., 1991, *J. Phys. Chem.*, **95**, 5370.

Nowak, P., Kleinrahm, R., Wagner, W., 1997, *J. Chem. Thermodyn.*, **29**, 1137.

Funke, M., Kleinrahm, R., Wagner, W., 2002, *J. Chem. Thermodyn.,* **34**, 2001.

Monago, K. O., 2010, *Can. J. Chem. Eng.*, **88**, 55.

Masters, A. J., 2008, *J. Phys. Condens. Matter*, **20**, 283102.

Rosch, T. W., Errington, J. R., 2007, *J. Phys. Chem. B*, **111**, 12591.

Schultz, A. J., Kofke, D. A., 2009, *Mol. Phys.*, **107**, 1431.

Schultz, A. J., Kofke, D. A., 2009, *Mol. Phys.*, **107**, 2309.

Kroto, H. W., Heath, J. R., O'Brien, S. C., Curl, R. F., Smalley, R. E., 1985, *Nature*, **318**, 162.

Girifalco, L. A., 1991, *J. Phys. Chem.*, **95**, 5370.

Girifalco, L. A., 1992, *J. Phys. Chem.*, **96**, 858.

Osman, S. M., Bahaa Khedr, M., 2009, *Phys. Chem. Liq.*, **47**, 564.

Hagen, M. H. J., Meijer, E. J., Mooij, G. C. A. M., Frenkel, D., Lekkerkerker, H. N. W., 1993, *Nature*, **365**, 425.

Cheng, A., Klein, M. L., Caccamo, C., 1993, *Phys. Rev. Lett.*, **71**, 1200.

Caccamo, C., Costa, D., Fucile, A., 1997, *J. Phys. Condens. Matter*, **106**, 255.

Broughton, J. Q., Lill, J. V., Johnson, J. K., 1997, *Phys. Rev. B*, **55**, 2808.

Caccamo, C., 1995, *Phys. Rev. B*, **51**, 3387.

Hasegawa, M., Ohno, K., 1996, *Phys. Rev. E*, **54**, 3928.

Hasegawa, M., Ohno, K., 1999, *J. Chem. Phys.*, **111**, 5955.

Costa, D., Pellicane, G., Caccamo, C., Schöll-Paschinger, E., Kahl, G., 2003, *Phys. Rev. E*, **68**, 021104.

Lui, F. L., Wang, J., 2006, *J. Mol. Struct.*, **778**, 105.

Smith, V. H., Thakkar, A. J., 1972, *Chem. Phys. Lett.*, **17**, 274.

Tang, Y. P., 2007, *J. Chem. Phys.*, **127**, 164504.

Baxter, R. J., 1968, *J. Chem. Phys.*, **49**, 2770.

Noro, M. G., Frenkel, D., 2000, *J. Chem. Phys.*, **113**, 2941.

Hagen, M. H. J., Meijer, E. J., Mooij, G. C. A. M., Frenkel, D., Lekkerkerker, H. N. W., 1993, *Nature*, **365**, 425.

Rosch, T. W., Errington, J. R., 2007, *J. Phys. Chem. B*, **111**, 12591.